Imperial College London

Thesis

Scalable Soft Matter Patterning From The Macro To The Nanoscale

Author:

Manuela Nania

Supervisors:

Dr João T. Cabral

Prof Omar K. Matar

A thesis submitted in fulfilment of the requirements

for the degree of Doctor of Philosophy

in the

Polymers and Microfluidics Group

Department of Chemical Engineering

July 2017

Abstract

Surface patterning is important for a range of engineering applications, including controlled wetting and spreading of liquids, adhesion and assembly of smart coatings. There is therefore a need of simple, cost-effective and scalable techniques for pattern formation over a wide range of scales. Conventional methods fail to comply with these requirements, as costs and complexity increase in the attempt to impress nm to μm scale features. By contrast, wrinkling of bi-(multi-)layers is inherently inexpensive, scalable and robust, and has the potential for soft matter patterning from the nano- to the macro-scale. This work investigates the controlled multi-layer generation of polydimethylsiloxane (PDMS) glassy skins via surface oxidation using plasma exposure and/or ultraviolet ozonolysis (UVO). Uniaxial mechanical compression is then employed to induce pattern formation via a well-known wrinkling instability. Topographies with wavelengths down to 45 nm are achieved, for the first time, as well as features with characteristic lengthscales of $\sim$ 10s μm. Moreover, simple design routes for double frequency nested pattern formation, imposed by compression of tri-layer laminate films, are established.

The work concludes by exploiting wrinkling as a method for the mechanical characterisation of thin drying films. A time-resolved wrinkling interrogation during film drying is established as a simple and reliable approach to determining evolving mechanical properties of films, overcoming the difficulties associated with handling very thin free-standing films and the limited sensitivity of conventional methods, with potential applications extending to coatings, personal care items, and foods.

Declaration

The work presented in this thesis is the result of my own original research. All collaborative work has been acknowledged and the literature used referenced.

Copyright Declaration

Dedication

"La fortuna non esiste: esiste il momento in cui il talento incontra l'occasione"

Seneca

A Mamma, che mi ha insegnato a volare.

E a Michele, che mi ha spinto.

Acknowledgements

The person I am now, my achievements, this PhD thesis, are the result of what I have been taught by the people around me. And I want to take this occasion to express all my gratitude.

I thank my supervisor Dr João Cabral, for his support. He has transmitted me his knowledge about soft matter and from him I learnt the importance of communication in science. I thank my supervisor Prof Omar K. Matar, for all the discussions, about science and about life. He is an inspiration, an example every professor should look to.

I am grateful to everyone I met in the Polymers and Microfluidics group. I thank Alessandra, for the early morning coffees. She taught me the importance of details: all the figures in this thesis are dedicated to her. I thank Ruhina, from whom I learnt to always stand up, when life lets you down, and fight, like she does every day. I thank Fabrizia, for having introduced me to the wonderful world of scattering and, most importantly, for having been the older sister I never had. Thanks to Christiana for her contagious laugh, which can brighten even the darkest day. I thank Andreas, Giulia and Matt for all their support.

A special thanks goes to my students, especially Will, Matt, Olivia, Caitlin, Helen, Sorcha, Sang Ju, Zhi Yuan, Del-Wyn and Chia. I thank them for all the times they made me feel like I was making a difference. They taught me how to teach, and I have never loved something so much.

I thank Ascanio, for giving me the opportunity to work for *The Young Consultant* and being with me through the crazy times of the job hunting. From him I got how important resilience is, and to try and try until you reach your objective.

I want to say thank you to all the *Chem Eng PhDs*. Thank you, for all the laughs, all the lunches, all the coffees (and we know they were many!) and all the Jagerbombs (maybe too many!). Thank you for the moments of light heartedness and for being part of the best memories I have here.

I thank Susi and all the Department of Chemical Engineering for having given me the opportunity of pursuing this PhD and having contributed to a great student experience.

***

Ringrazio i miei genitori, per tutte le volte che mi hanno detto di no. Li ringrazio per l'educazione e i valori che ci hanno trasmesso, e che mi hanno fatto diventare la persona che sono. Un ringraziamento speciale va a mia mamma, che mi ha insegnato tutto quello che so. La ringrazio, per avermi aiutata a venire qui, ed avermi salutato con un sorriso, nonostante il cuore le stesse scoppiando dentro. Mi ha insegnato cosa significa amare qualcuno più di se stessi. Questa tesi è dedicata a lei.

Ringrazio Valeria, per tutte le volte che, a modo suo, mi ha fatto sentire la sua stima e il suo amore. E per tutte le volte in cui è stata la sorella maggiore, insegnandomi ad usare la razionalità, quando le emozioni mi soffocavano. Ringrazio Nonna Carmen, che mi è sempre stata vicina, da prima che i miei occhi vedessero il mondo. Ha continuato e continua a seguirmi, in ogni parte del mondo, sempre un passo indietro, pur essendo 100 passi avanti a me. Un ringraziamento speciale va a Zia Silvana, Zio Mimmi, Fabio e Nonna Wanda, perchè ogni volta che mi giro, li vedo sempre lì a fare il tifo per me.

Ringrazio Michele, per quella telefonata nel 2011 in cui mi disse di fare domanda all'Imperial. Mi ha spinta fuori una comfort zone che non avrei mai lasciato altrimenti. E lo ringrazio, per essere stato un punto di riferimento durante questi

anni a Londra. Grazie ad Alessandra, la mia bona, per avermi fatto compagnia con una *pukka* anche nelle serate più calde, e per essere diventata una vera amica.

Grazie a Cristina, per essere stata con me più quando ero a Londra di quando fossi a Napoli. Grazie a Italo, per avermi aiutata a ritrovare me stessa ogni volta che mi sono persa.

E poi un ringraziamento speciale va a Marco. Per la pazienza con cui ha gestito i miei momenti di ansia senza senso. Per tutte le volte che ha riletto con me questa tesi. Per la concentrazione con la quale mi ha ascoltata prima di ogni prova importante. Per avermi aiutata a sconfiggere ogni timore del futuro, e avermi dato la voglia di crescere e scoprire il mondo, insieme a lui.

Contents

Symbols

A	pattern amplitude	m
A_r	aperture of the lenses	m
b	scattering length	m
$c_{0,glycerol}$	glycerol mass fraction in solution	-
d	depth from the surface	m
d_{lamp}	distance from UV lamp	m
d_{el}	distance between electrodes	m
D	plasma dose	J
$D_{equivalent}$	UVO dose	J m^{-2}
E	elastic modulus	Pa
$\bar{E}$	plane strain modulus	Pa
f	frequency	Hz
F	applied force	N
F_c	critical force for wrinkling	N
h	thickness	m
I	intensity	W m^{-2}
I_m	inertial moment	m^4
k	Winkler modulus	Pa
k_1	Rayleigh constant	-
KI_0	kinetic parameter	J^{-1}
L	length	m
M	mass	kg
M_w	molecular weight	kg mol^{-1}

N_a	Avogadro number	-
p	power	W
P	pressure	mbar
Q	momentum transfer	m $^{-1}$
r	curvature radius	m
R	reflectivity	-
SLD	scattering length density	m^{-2}
t	time	s
T	temperature	°C
$V_{breakdown}$	breakdown voltage	V
w	width	m
y_{O_2}	oxygen gas content	-
α_L	linear thermal expansion coefficient	°C $^{-1}$
ϵ	applied strain	-
ϵ_c	critical strain for wrinkling	-
ϵ_L	critical strain for stress localisation phenomena	-
ϕ	conversion	-
γ_{se}	number of secondary electrons	-
λ	pattern wavelength	m
λ_r	wavelength of the radiation source	m
μ	attenuation parameter	m $^{-1}$
ν	Poisson ratio	-
ρ	density	kg m^{-3}
θ	incident angle	°
θ_c	critical incident angle	°

Chapter 1

Introduction

Current and emerging industries, ranging from microelectronics[1–3] to photonics [4, 5] and advanced coatings [6], extensively employ micro and nano-scale structures. An increase in the demand drives an incessant need of improved methods for nano-patterning and micro-components fabrication. The improvement has to involve three main aspects: cost, easiness of implementation and range of pattern dimensions attainable. Ideally one seeks for a method that is cheap and simple thus easily scalable, and that allows for large area patterning of soft surfaces from the macro to the nanoscale. However conventional techniques do not fully comply with these requirements .

Lithography remains one of the most well-known and established patterning processes, as it allows the creation of patterns whose dimensions can vary from the nano- to the micrometer scale [7, 8]. Amongst lithographic techniques, *photolithography* has been widely utilised [9], especially for the manufacturing of microelectronic and, more recently, microfluidic devices [10, 11]. This technique allows for pattern formation on a monomer (or polymer) which is sensitive to UV-light. The monomer (or polymer) is usually referred to as *photoresist* [12], defined as 'negative' if it solidifies upon light exposure, and 'positive' when light modifies its chemical structure making it more soluble in a developer solution, and thus easily removable [13, 14]. In *conventional photolithography*, referred as *contact* or *proximity printing*, pattern creation results from the application of a photomask,

placed between the monomer and the collimated light source. This allows the polymerisation of selected areas, resulting in a specific geometry. Recent studies have shown the possibility of controlling the process and of creating a variety of two- and three-dimensional structures [15, 16]. The described setup is trivial to implement, the photomasks can be easily designed and fabricated, and the photo-curable monomer (or polymer) can be sourced readily at relatively low costs. Moreover, large areas can be patterned and the throughput is notably high.

Conventional photolithography, however, has an intrinsic limitation in relation to the range of achievable pattern dimensions. In order to compute the resolution of the technique, Res, one has to consider optical diffraction limitations, which are given by the Rayleigh equation [17]:

$$Res = \frac{k_1 \lambda_r}{A_l} \tag{1.1}$$

where k_1 is a constant typical of the monomer chosen, λ_r is the wavelength of the UV light, and A_l denotes the aperture of the lamp lens. This equation suggests that, in order to improve the resolution, one could decrease the wavelength of the light source, or increase the aperture of the lenses. In contrast to the predictions of equation (1.1), empirical observations have shown that the best resolution that can be achieved is $Res \approx \lambda_r$ [17], which can go up to 193 nm when using a ArF excimer laser as the illuminating source.

Patterned surfaces with lower feature sizes (down to 37 nm) have been fabricated using *projection printing photolithography*, where an optical lenses system is utilised to directly project the pattern from an excimer laser onto the photoresist. Further attempts to decrease the pattern dimensions have been developed through *immersion* [18] or *extreme-UV lithography* [19] as well as *resolution enhancing techniques* [20]. Even though these techniques have succeeded in extending the range of pattern dimensions, they still require expensive and complex equipment with an associated increase in capital and operating costs, which can often become over-riding factors.

Method	Costs	Large Area	Throughput	nm-scale patterns
Photolithography (conventional)	+	+	+	-
Photolithography (projection printing)	-	-	+	+
E- beam lithography	-	-	-	+
Ideal technique	+	+	+	+

TABLE 1.1: Comparison between the reviewed techniques for soft matter patterning in terms of costs, throughput, and feasibility for large area and nm-scale patterning.

Alternatives to photolithography include *Electron Beam Lithography* (EBL), which has been widely utilised in the semiconductor industry for the manufacturing of nanoscale components such as masks [21]. As the form of radiation is now an electron beam, the resolution of the technique (capable of impressing patterns with dimensions down to 5 nm [21]) is no longer influenced by optical diffraction, but by factors such as the beam diameter, and the forward and backward-scattering of electrons in the resist and from the substrate, respectively [22]. EBL is mainly utilised in two forms: *Electron Projection Lithography* (EPL), and *Direct Writing*. The EPL takes advantage of an electron beam, which passes through a membrane made of an electron-absorbing material, before being focused on a substrate covered by the resist [23]. The first limitation of the technique is the need for masks with very small thicknesses, due to the relatively low penetration depth of electrons. One also has to consider the fact that the electron beam has a field size that should not exceed ~ 1 mm^2 in order for the effects of field aberrations to be minimised. The patterning of larger areas, therefore, requires the need of precisely merging a number of small sub-patterns, resulting in a low throughput.

A low throughput is also a characteristic feature of *Direct Writing*, where the resist is impacted directly by the beam. The latter moves thanks to a deflection system and creates the pattern pixel-by-pixel, with the aid of a blanker to alternatively switch the beam on and off.

1.1 Wrinkling for soft matter patterning

The brief review presented above (summarised in Table 1.1) covered only a portion of all the techniques available for soft matter patterning (e.g. block copolymer assembly [24–26] or printing techniques [27–29]). Nonetheless, it highlighted the need for a scalable technique for soft matter patterning from the macro to the nanoscale. The naturally-occuring phenomenon of *wrinkling* may offer a potential solution [30].

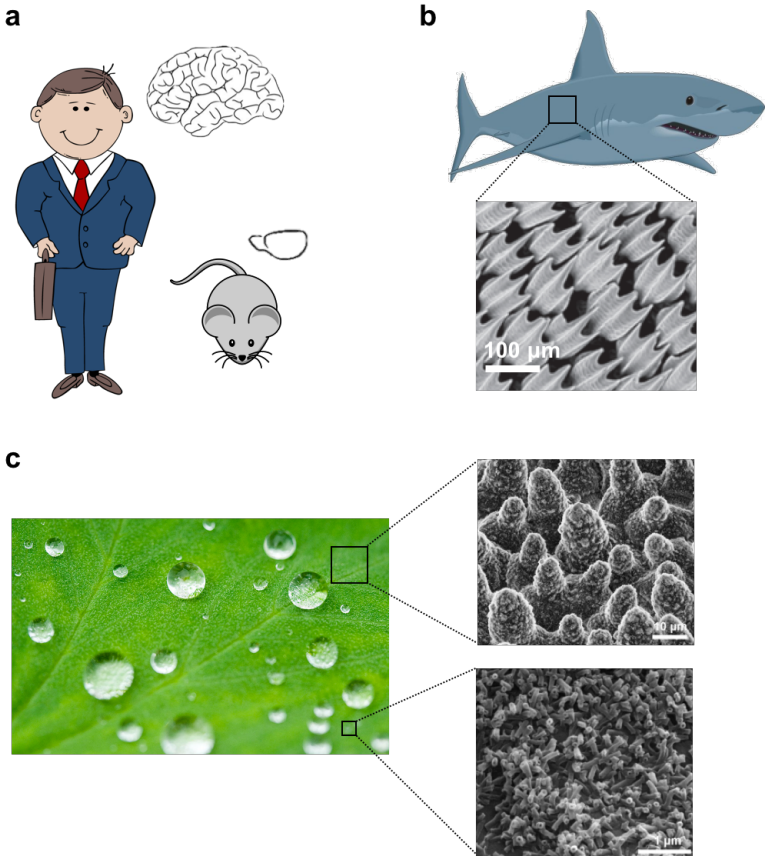

FIGURE 1.1: Examples of wrinkles in nature. a) Comparison between the human (wrinkled) and the mouse (flat) brain. Sketches reprinted from [31]. b) Patterns on the skin of sharks. Optical microscopy image reprinted from [32]. c) Superhydrophobic properties of the lotus leaf, driven by hierarchical features. Microscopy images reprinted from [33].

Thanks to this intriguing phenomenon, the effective area of a human brain is three times larger than the external, surface area, contributing to large-information storage, and facilitating the execution of complex functions [31, 34]. Wrinkling

patterns on the skin of sharks, with characteristic dimensions in the 100 of microns range [35], prevent the attachment of microbes and other marine organisms [35, 36], and act to reduce drag due to their effect on the velocity boundary layer [32]. The characteristic micro and nano features on the skin of geckos have been found to result in unique anti-wetting and self-cleaning properties, as well as impeding the adhesion of contaminant agents [37]. Wrinkling mechanisms leading to a hierarchy of patterns are also responsible for the superhydrophobic properties of the lotus leaf, referred to in the literature as the *lotus effect* [38, 39]. These patterns are characterised by features in the micron range (so-called *papillae*), on top of which nanoscale protrusions are formed [39]. The presence of secondary structures causes a reduction in the water contact angle hysteresis, and more stable superhydrophobic states [33]. These examples, shown in Figure 1.1, show how different functionalities correspond to different geometrical features.

***

Inspired by these and other phenomena, scientists have looked for ways to replicate these ordered patterns in the lab [40–42]. It is intuitive that the application of a compressive or tensile force to a single layer of an elastic material (with mechanical properties expressed through the elastic modulus E_s), can cause (if the force exceeds a critical value) a temporary bending deformation, which then disappears when the strain is released. The deformation is characterised by a length scale commensurate to the lateral dimension of the beam. Consider now a situation whereby another, thinner, and stiffer film (with an elastic modulus $E_f > E_s$) is placed atop this layer, and assume that they adhere to one another perfectly. When a uniaxial, compressive strain is applied to the bilayer, the mismatch between the mechanical properties of the film and the more compliant substrate causes instabilities, which can manifest themselves through the formation of periodic structures on the surface characterised by a well-defined wavelength, λ, and amplitude, A [43–45]. Figure 1.2 schematically describes this phenomenon. A quantitative description of the wrinkling phenomenon described above involves a force balance [46–48], which accounts for the competition between film bending

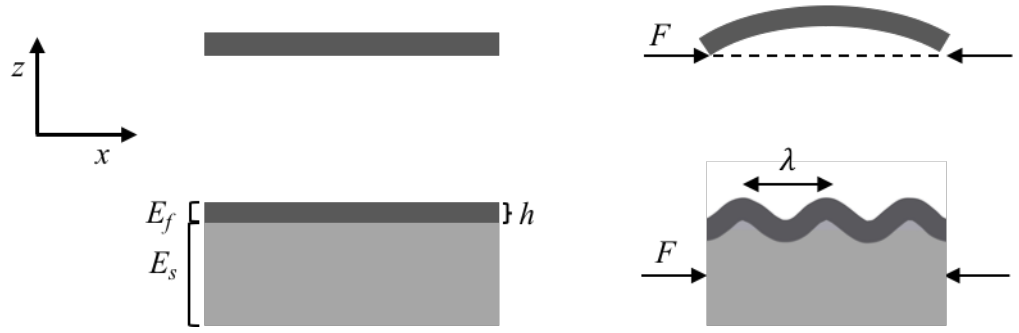

FIGURE 1.2: Schematic of film responses to compression. On the top, an unsupported layer is subject to a compressive force F. When the force is greater than a critical value, bending occurs, with a characteristic length scale commensurate to the length of the layer. On the bottom, the film is placed onto an elastomeric substrate, forming a bilayer. When compressing above a critical treshold, the film wrinkles with a characteristic wavelength λ, that can be extracted from a force or energy balance.

and substrate deformation:

$$\bar{E}_f I_m \frac{d^4 z}{dx^4} + kz + F\frac{d^2 z}{dx^2} = 0 \tag{1.2}$$

Specifically, the first term accounts for the force arising when the film buckles whilst the second term in the equation describes the corresponding deformation of the elastomeric substrate; as a result of the competition between these two mechanisms, the system chooses a characteristic buckling wavelength. The last term accounts for how the applied force affects the film. In the equation, $\bar{E}_f$ is the *plane strain modulus* of the film, given by $\bar{E}_f = E_f/(1-\nu_f^2)$, with ν_f being the Poisson's ratio; I_m denotes the inertial moment of a film with thickness h and width w given by $I_m = wh^3/12$; z and x represent respectively the directions orthogonal and parallel to the the film surface (and the compressive force applied F); and k is the Winkler modulus of the substrate, assumed to be a semi-infinite plane, given by $k = \bar{E}_s w\pi/\lambda$ [49], with $\bar{E}_s$ being the substrate's plane strain modulus, related to the its Young's modulus and Poisson's ratio through $\bar{E}_s = E_s/(1-\nu_s^2)$. If $z(x) = A\sin(2\pi x/\lambda)$, then it follows that

$$F = \frac{h^3\pi^2 w\bar{E}_f}{3\lambda^2} + \frac{\lambda w\bar{E}_s}{4\pi} \tag{1.3}$$

which describes how the force applied to the bilayer with mismatching mechanical properties, affects the wavelength of the sinusoidal patterns generated by the instability.

The critical force, F_c, for the onset of instability corresponds to the minimal force required to trigger wrinkling with characteristic wavelength λ. Therefore an expression for λ can be found by

$$\frac{\partial F}{\partial \lambda} = \frac{\bar{E}_s w}{4\pi} - \frac{2\pi^2 \bar{E}_f w h^3}{3\lambda^3} = 0 \tag{1.4}$$

which allows finding the wavelength of the wrinkles that arise when the force is equal to the minimal value F_c. Equation 1.4 leads to

$$\lambda = 2\pi h \left(\frac{\bar{E}_f}{3\bar{E}_s} \right)^{1/3} \tag{1.5}$$

The expression for the wavelength can be substituted into (1.3) in order to obtain an expression for the critical value of the force F_c:

$$F_c = \frac{\left(\bar{E}_f\right)^{1/3} \left(3\bar{E}_s\right)^{2/3} hw}{4} \tag{1.6}$$

The strain applied, ϵ, is related to the force through

$$\epsilon = \frac{\sigma_c}{\bar{E}_f} = \frac{F_c}{hw\bar{E}_f} \tag{1.7}$$

In contrast to F, the measurement of ϵ is trivial, and directly derivable from the bilayer deformation in the applied strain direction, compared to the relaxed state. By substituting the expression of the critical force, the critical value of the strain, ϵ_c, is then be given by [47, 50]

$$\epsilon_c = \frac{1}{4} \left(\frac{3\bar{E}_s}{E_f} \right)^{2/3} \tag{1.8}$$

The critical strain thus depends on the mismatch between the elastic moduli of

the film and the substrate, decreasing when their ratio increases. In the context of facial wrinkles, for instance, as the epidermis stiffens with age [51], the critical force decreases accordingly, triggering skin wrinkling.

Based on the considerations so far we can conclude that, given a thick substrate-thin film bilayer, pattern formation occurs if ϵ exceeds ϵ_c. Above threshold, observations suggest that the wavelength λ does not strongly depend on ϵ. In order to compute the amplitude A, one can start by writing the following expression [45]

$$\epsilon - \epsilon_c = \frac{\int_0^\lambda \left(1 + \left(\frac{dz}{dx}\right)^2\right)^{\frac{1}{2}} dx - 1}{\lambda} \tag{1.9}$$

whence the overstrain $(\epsilon - \epsilon_c)$ equals the contour length of the wrinkle pattern, limited to only one period of a pattern (assuming periodic patterns). The function to integrate can be simplified via the assumption that dz/dx is relatively small, which holds when the amplitude is at least one order of magnitude lower than the wavelength, leading to

$$\epsilon - \epsilon_c = \frac{\int_0^\lambda \left(1 + \left(\frac{dz}{4dx}\right)^2\right) dx - 1}{\lambda} \tag{1.10}$$

from which

$$\epsilon - \epsilon_c = \frac{\pi^2 A^2}{\lambda^2} \tag{1.11}$$

for $z(x) = A\sin(2\pi x/\lambda)$. Substitution of equation (1.5) into this equation yields [46, 47, 50]

$$A = h\left(\frac{\epsilon}{\epsilon_c} - 1\right)^{1/2} \tag{1.12}$$

This equation shows that an increase in the strain applied results in an increase in pattern amplitude. Later in the thesis, it will be shown that the wavelength is also affected by an increase in the strain, and equations (1.5)-(1.12) are modified accordingly.

It is interesting to note that sinusoidal wrinkling can evolve into more complex modes such as creasing [42, 53–56], folding [57–60], period doubling [59, 61], ridging

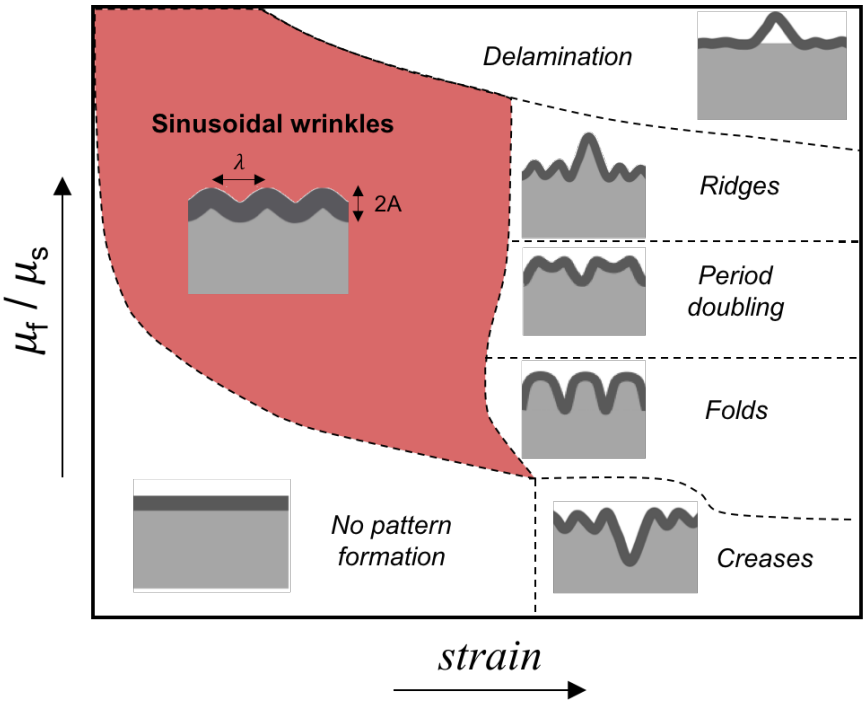

FIGURE 1.3: Evolution of the bilayer responses as a function of the applied strain, for different ratios of the shear moduli μ_f/μ_s. The region where sinusoidal wrinkling, with features sizes λ and A, occurs, has been highlighted as it is the focus of this project. The phase diagram is reproduced from the findings of [52].

[60, 62, 63], or to failures modes such as delamination [62, 64–66], or the formation of cracks [67–69]. The transition to these modes is marked by a critical value of the strain ϵ_L [54, 60], which depends on the ratio between the shear modulus of the film and the substrate (μ_f/μ_s). A detailed description on the onset of these instabilities can be found in the work of Wang and Zhao [52]. The authors studied bilayers with different μ_f/μ_s and mapped the evolution of pattern morphologies as a function of strain. A phase diagram is reproduced qualitatively in Figure 1.3 based on their findings. The diagram is meant to highlight that sinusoidal wrinkling, of interest in this project, only represents a portion of the range of patterns achievable via wrinkling.

In the next sections, Equations (1.5), (1.8) and (1.12) will be referred as the *bilayer model*. This model suggests that wrinkling may provide the basis for a scalable method for soft matter patterning over a wide range of scales, from nm to mm. This can be done by tuning the thickness of the top layer and the applied strain. It is important to note, however, that there are limits to the pattern dimensions

accessible, which are primarily set by the techniques for bilayer formation and, to a lesser extent, strain application.

1.1.1 Towards optimal techniques for bi-layer formation and strain application

To form the bilayer, one can simply select a substrate and place a film of desired thickness on top, where the materials of the two layers are independently chosen in relation to the modulus mismatch required. To this extent, the simplest technique is referred as *thin film deposition*, generally achieved via floating [70, 71] (where the film is deposited in its solid state), subsequent evaporation and condensation [72–75] or ion sputtering [76–80].

Conventionally in film floating, the material that makes up the film is firstly diluted with a solvent, to obtain a solution with concentration c; the solution is then spun coated onto a hard support (glass or silicon), and film formation occurs via solvent evaporation. The resulting film thickness is directly related to c, to the spinning time and speed and to the molecular weight of the polymer. The film formed on the support is then placed in contact with the substrate of choice and the sandwich is immersed in a liquid (usually deionised water). In this way, provided there is a strong interaction between the materials selected for the substrate and the film, the film detaches from the support and is transferred to the substrate, leading to bilayer formation. Several studies report on solid film deposition in the dry state [81–83]. In one of these works, Sharp and co-workers [81], fabricated polystyrene (PS)/polyethylene oxide (PEO) bilayers. PS films on a glass support were transferred via floating on a metal slab, where a circular hole had previously been drilled: by doing this the film was only clamped at the edges (along the contour of the hole), otherwise freely standing. Thus, the PS film was placed onto a PEO layer, supported on a Si wafer: as a result of surface forces the PS film detached from the metal support and a PS/PEO bilayer was formed. Wrinkling was then induced by heating the laminate structure, leading to melting of the PEO substrate with subsequent strain applied to the PS film, induced by the change

in interfacial area. Pattern formation was observed with different combinations of polymer layers using the same technique [82, 83]. These methods, while relatively easy to implement, have one main downside. Indeed, the multiple steps involved result in a relatively slow process, which is also not suitable for scaling up.

An alternative to film floating is *vapour film deposition*, involving a metallic material which is firstly sublimed in a vacuum chamber then condensed onto the substrate to form a film. This technique for bilayer formation has been utilised in one of the first studies on patterning via wrinkling [72]; in this work, gold was deposited on a polydimethylsiloxane (PDMS) substrate and wrinkling was induced via thermal strain, achieved upon cooling of the substrate, previously heated to allow for evaporative gold deposition. Langley *et al.* [75] also employed this method to deposit aluminium onto a PDMS substrate: wrinkling was then mechanically induced on the resulting bilayers, leading to periodic patterns. By varying the mechanical strain over the surface of the samples, the authors showed that the wavelength of the patterns changes, resulting in different wetting properties.

Metallic film fabrication can also be achieved by ion sputtering. Ions (generally Ar^+) can be accelerated via a potential gradient before impacting a metal of choice, thus transferring their momentum to the surface atoms. The atoms, once in the gas phase, can be transferred onto the substrate, where film formation occurs. Laminate structures obtained via this method have been widely utilised to study surface wrinkling. Watanabe *et al.* [76] mechanically-induced wrinkling on bilayers obtained by sputtering gold on a silicon substrate, also quantifying the effect of stiffening the substrate on the resulting pattern morphology. Serrano *et al.* [77] worked with SiO_2 instead (commonly utilised for active plastic components), sputtered on polymethylmethacrylate (PMMA) and induced wrinkling on the resulting bilayers by imposing a temperature gradient. Small film thicknesses (thus pattern dimensions) are achievable via these techniques, though this comes at a cost due to both the metal utilised, the complex equipment needed, and the non-trivial implementation of the process. It is thus evident that the formation of the bilayers using these techniques takes away the intrinsic simplicity of wrinkling,

making the pattern formation complex, cost-ineffective, and unattractive at large scales.

***

Serendipity is about making discoveries by accident and perfectly describes what opens a new path for bilayer fabrication. Casper *et al.* [78] were studying wrinkling of bilayers obtained via sputtering of indium oxide on a PDMS substrate, when they noticed that patterns were present even after the film was removed. They justified the observation by considering the substrate modification which occurs during sputtering. As a result of this modification a thin film is formed at the surface, creating thus a sandwich bilayer where wrinkling can be induced, without recurring to film deposition. The mechanism underlying this phenomenon is related to the nature of PDMS, an organic, transparent, elastomeric polymer made up of a silicone matrix. Its chemical structure is composed of number n of repeating monomer units $SiO(CH_3)_2$. The interesting property is that the $Si-CH_3$ groups can be cleaved into OH groups [84–87] when the polymer is subjected to an oxidative treatment, which also results in severing the $Si-O$ bonds (responsible for the PDMS flexibility). A *glassy*, silica layer can eventually form upon sufficient substrate conversion [86, 87]. In the first instance, this surface modification alters the wetting properties of PDMS, which becomes hydrophillic. More importantly, this denser film on top of the bulk PDMS, effectively yields a strongly bound 'sandwich bilayer' with a high skin/substrate modulus contrast as required for wrinkling. However, we first have to understand how the oxidation reaction is carried out in order to assess the viability of substrate vitrification, compared with the other film deposition techniques.

PDMS was found to oxidise upon air exposure at room conditions, albeit at an extremely slow rate. This reaction, occurring over long time scales, can potentially turn into a faster one when carried via a radical mechanism. In case of PDMS conversion, such radical species are formed when plasma oxidation is employed. The plasma is created within a chamber, by means of an oscillating electric field which ionises a gas at low pressure ($\sim 10^{-4}$ bar) conditions [88]. As a result, oxygen radicals are formed, which rapidly react with the surface first, eventually

penetrating into the bulk when sufficient plasma exposure takes place. A similar result is obtained by replacing plasma exposure with Ultra Violet Ozonolysis (UVO) [89], relying on the use of light with wavelength ranging from 185 to 254 nm. Within a chamber at ambient pressure conditions, the sample is placed in contact with the light source, generating highly penetrative radiations responsible for the formation of oxygen radical species. These can subsequently react with the molecular oxygen present to form ozone, which contributes to substrate conversion [85].

Both plasma and UVO processes allow for PDMS oxidation on large areas over relatively short time-scales (from seconds to hours). The two techniques can be easily implemented and do not require installation of complex equipment: PDMS vitrification thus satisfies the low-cost and scalability criteria in terms of bilayer formation. However, so far we still lack of an indication of pattern dimensions achievable when inducing wrinkling on these laminate structures. In this context, several literature studies on pattern formation via wrinkling of oxidised PDMS/PDMS bilayers are relevant.

Bowden *et al.* [90] were amongst the first to study the formation of wrinkles on bilayers obtained upon oxygen plasma oxidation of PDMS. They found that by increasing the plasma treatment time, the wavelength (and amplitude) of the patterns induced on the resulting bilayers increased accordingly, going from hundreds of nanometers to a few microns. The same dependence was also established by other more recent studies [91–93]. Considering equations (1.5) and (1.12), we can easily deduce that an increase in the pattern characteristic dimensions with the exposure to plasma might be related to an increase in the thickness of the oxide layer and/or its stiffness. Bayley *et al.* [93] elucidated on this matter by studying the evolution of the glassy layer thickness and *densification* by means of X-ray reflectivity. They observed an increase of h with exposure time, ranging from ≈ 2 to 40 nm, and that the PDMS to silica conversion increases during the first stages, until reaching a plateau upon saturation. When inducing mechanical wrinkling on the bilayers obtained, they found a minimum wavelength $\lambda_{min} \approx 140$ nm. They reported the need of increasing the mechanical strain applied when lowering the

treatment duration, in agreement with the initial film densification; indeed, by recalling Equation 1.8, we can infer that during the first stages of plasma exposure, the mismatch between the elastic modulus of the top film and the substrate is not significant, leading to a relatively high value of the critical strain. The minimum pattern dimensions are thus only achieved when applying a strain of $\approx$ 200 %; further decrease of the exposure time did not yield any wrinkling even at these high values of the mechanical stress, suggesting that i) the modulus contrast is too low or ii) the film is yet to be formed. The study of Bayley *et al.* [93] proved that one can effectively access highly ordered patterns with lateral dimensions down to 140 nm via wrinkling. Despite the limitations, e.g. the need of using significant strains which might lead to material failure, these results represent a valuable start towards large area nm-patterning via wrinkling.

To date bilayers obtained via PDMS plasma oxidation proved to be suitable to obtain morphologies with feature sizes between hundreds of nm to few microns. We now have to focus on whether (and how) laminate structures fabricated via substrate vitrification can give rise to morphologies with larger($\sim$ 100s microns) characteristic dimensions. To resolve this, we can examine UVO oxidation of polydimethylsiloxane. Wrinkling experiments performed on UVO oxidised PDMS/PDMS bilayers indeed showed the formation of ordered sinusoidal patterns whose characteristic dimensions vary from $\approx$ 10-100 μm [89, 94–98]. If we recall the dependence of λ and A on h and $\bar{E}_f$ it is clear that this oxidative treatment yields thicker and softer skins compared to plasma exposure. A study also pointed out that, under specific conditions, multiple frequency hierarchical morphologies can be mechanically induced on PDMS upon UVO exposure [94]. These features remind us of the lotus leaf, where generations of patterns with different length-scales contribute to its well-known superhydrophobic properties [39].

Based on the findings presented, PDMS oxidation via ultra violet ozonolysis or plasma exposure appears as an ideal technique for bilayer formation. However, patterns arise upon strain application and the characteristic dimensions (at first instance the amplitude A) are affected by the extent of bilayer tension or compression: what is, thus, the optimal strategy to apply strain?

In some of the studies presented so far, we mentioned wrinkling occurring via *thermal* strain application [72, 90]. When the film/substrate bilayer is heated to a certain temperature ($T_{initial}$), each of the two layers will expand: upon subsequent cooling to T_{final}, the two layers experience a strain $\epsilon_{thermal}$ which can be estimated as

$$\epsilon_{thermal} = \alpha_L(T_{initial} - T_{final}) \tag{1.13}$$

where α_L is the linear thermal expansion coefficient. A mismatch in the thermal expansion coefficients of the film and the substrate results in a net strain applied to the bilayer, that can cause wrinkling to occur. The use of a temperature gradient to impose strain shows two main downsides. First of all, the bilayer can expand in multiple directions, thus not allowing for compression along selected axes (e.g. uniaxial compression); furthermore, the expansion resulting from the temperature gradient is not significant. Small values of ϵ can therefore be achieved, which are not suitable for bilayers with low moduli contrast (thus high ϵ_c), as well as impeding tuning the wrinkles' amplitude over a relevant range.

Alternatively, several studies reported the possibility to use swelling as a way to induce bilayer wrinkling [99–104]. This exploits the increase of dimensions an elastoplastic polymer or an hydrogel is subject to when a solvent diffuses within it. Again, provided there is a mismatch in the rate of solvent uptake between the two layers, patterns can form as a result of surface instabilities. Breid and Crosby [100] actually employed this method on UVO oxidised PDMS, by placing the bilayers in a vapour atmosphere allowing for solvent diffusion to take place and swelling to occur. Control on the strain applied could be achieved via changing the composition of the solution, and accordingly its vapour pressure. A quantification of the strain resulting from swelling is given by [105]. Beam bending experiments were carried out and the following correlation for $\epsilon_{swelling}$ was derived

$$\frac{h_s}{r} = \frac{\frac{2E_f h_f \epsilon_{swelling}\left(h_s+h_f\right)}{E_s h_s^2}}{1+\left(\frac{E_f h_f^2}{E_s h_s^2}\right)^2 + 2\frac{E_f h_f}{E_s h_s}\left(2+3\frac{h_f}{h_s}+2\frac{h_f^2}{h_s^2}\right)} \tag{1.14}$$

r indicates the curvature radius. The bilayer deformation resulting from swelling is represented schematically in Figure 1.4. Swelling induced patterns on bilayers

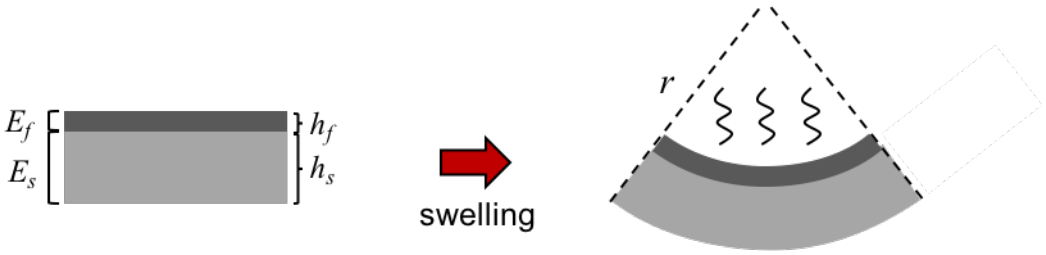

FIGURE 1.4: Schematic of bilayer deformation occurring upon solvent swelling.

formed upon substrate vitrification were also studied by Chung *et al.* [104]. The authors focused on laminate structures obtained via UVO oxidation of polystyrene, where strain was induced by swelling in toluene vapour. Depending on the extent of the UVO oxidation (thus thickness and mechanical properties of the topmost layer) a variety of periodic wrinkling patterns were observed, ranging between flower-like to concentric rings features. These morphologies were found to initiate corresponding to defects on the surface [104]. Swelling thus offers control on the strain applied as well as its rigorous quantification; however it is intrinsically denoted by the disadvantages already highlighted for the thermal strain. It is indeed not possible to control the dimensions along which expansion takes place, and the amount of strain applied is limited by the osmotic pressure. Furthermore the need of a solvent as well as the time required for diffusion to occur, are not desirable for a scalable and cost-effective patterning method.

The challenges associated with the use of temperature or swelling for strain application, leave us with another option which corresponds to mechanical strain. The latter requires a strain stage, where the bilayer can be clamped and stretched or compressed to the desired extent. Clamping a sample imposes a different condition at the boundaries compared to the case in which the material is free to move: however, the boundary effects are negligible compared to the numerous advantages

of this method. Firstly one can achieve control on the expansion, and, depending on the stage, uniaxial, biaxial or multiaxial strain can be imposed leading to an entire range of complex, controllable, morphologies. For example, ordered miura-ori patterns have been observed when mechanical strain was applied to the bilayer in two orthogonal directions. The two components of the strain have indeed two effects: a deformation which takes place out from the plane of the sample, similar to the one observed in the case of uniaxial strain, coupled with a '*on plane*' deformation responsible for the zig-zag pattern [92, 106]. Apart from the control over the axial deformation, significant values of the strain can be applied mechanically, opening up to a wider range of pattern dimensions achievable. The strain can then be simply quantified by measuring the increase in sample dimensions along the selected axes.

1.1.2 The Project

Based on all the considerations we have made so far, we decided to focus on pattern formation via **mechanical wrinkling** of bi- (multi-) layers obtained by **substrate vitrification**. While a range of materials can be used as substrates (e.g. polystyrene, which can be oxidised leading to the formation of an hard film on the surface [107, 108]), we choose to work with PDMS due to its relatively low elastic modulus ($\approx$ 1.6 MPa [109]), near incompressibility (Poisson ratio $\approx$ 0.5 [109]), large elongation at break (200 %) [110], surface adhesion and transparency. These substrate features are of interest for the pattern formation while, depending on the application, one can simply use the wrinkled PDMS as a mold and replicate the surface morphology onto the materials of interest.

We first focus on PDMS oxidation via plasma exposure and its impact on surface wrinkling. Building up from previous work [93], we perform a series of controlled experiments, where we systematically vary process parameters and evaluate their impact on the surface morphology. By doing this, we enlarge the limits of this method, and obtain ordered sinusoidal wrinkles with wavelengths ranging from 5 μm down to 100 nm, by employing relatively low values of the mechanical strain,

leading to a simple and reproducible process. We demonstrate that the optimal conditions for nanoscale patterning are achieved when oxygen is replaced by air as the ionising gas, representing an added value from manufacturing and safety standpoints. Patterns with these feature sizes could be of interest in the field of optics [111, 112] and photonics [58, 113]. For example these wrinkled substrates could serve as a template for the fabrication of diffraction gratings [111, 112], commonly utilised optical components whose periodic structure is responsible for the diffraction phenomenon occurring when shining light across them. As the structural periodicity impacts the diffraction characteristics, by wrinkling of air plasma oxidised PDMS a wide range of applications can be covered. Morphologies with these dimensions can also be utilised to improve the efficiency of organic solar cells, currently spreading out as a low-cost alternative to those using crystalline and polycrystalline silicon as starting material. Studies have demonstrated that when the cell surface is patterned with wrinkles with $\lambda \sim 1$ μm the efficiency increases significantly, with ≈ 47 % more energy produced compared to flat devices [58].

In an attempt to access even lower pattern dimensions, we then study the effects of the plasma treatment on the PDMS to silica conversion and glassy film formation. Through this deeper understanding we aim to justify the existence of a critical exposure time to be exceeded, corresponding to a minimum wavelength $\lambda_{min} \approx 100$ nm. As the simple tuning of the process variables can only go so far, we go back to the bilayer equations and evaluate the wavelength reduction achieved when increasing the substrate stiffness. We devise conventional strategies to increase the elastic modulus of PDMS by changing the curing conditions. Eventually we find that by using a '*two step*' process comprising UVO exposure followed by air plasma exposure we can effectively impress single frequency, sinusoidal patterns with dimensions in the deep UV range ($\lambda_{min} \approx 45$ nm), at low strain conditions. Surfaces with these morphologies have potential applications in optics and photonics, nano-fluidics, as well as template formation and contact printing.

After the success in obtaining sub-100 nm wrinkles, we explore the upper limit of pattern formation via mechanical wrinkling of oxidised PDMS. To this aim,

we focus on oxidation with ultraviolet ozonolysis and evaluate its impact on the pattern formation, by selectively varying the process variables. As expected, we are able to obtain sinusoidal features with lateral dimensions of tens to hundeds of microns. These can find application in the biological field, as cells can be confined in these patterns whilst analysing their behaviour as well as interactions with the environment [94] . One can also exploit the impact of the culture medium surface topography on the cell culture [114].

When studying UVO oxidation we also find that, under specific conditions, a second generation of nm-scale wrinkles arises on top of the μm-scale ones, leading to hierarchical patterns. We build upon these observations and estabilish the conditions for double-frequency, sinusoidal pattern formation; moreover we gain the ability to re-create these morphologies via different methods and tune independently the dimensions of the two generations of patterns. These findings have a significant applicability as surfaces with hierarchical patterns have showed a wide range of interesting properties, including self-cleaning [115], optical activity [116], wettability and superhydrophobicity [117–123]. Indeed the presence of a second generation of patterns causes air to be trapped within the features resulting in a transition from the Wenzel [124] to the Cassie-Baxter [125] state corresponding to a higher contact angle.

After having established the capabilities of wrinkling as a scalable and cost-effective method to impress patterns from the macro- to the nano-scale, we decide to look at the same process, but from a different perspective. So far the final aim was to obtain patterns via wrinkling and we have thus tried to optimise the bi- (multi-) layer formation depending on the final application. However, these patterns can be exploited to gain insight about the film mechanical properties. Specifically, if we recall the bilayer equations, it is intuitive that, by inducing sinusoidal wrinkling on bilayers and measuring the corresponding morphologies we can infer properties like the film's thickness and elastic modulus. This method, known as SIEBIMM [70, 126] has indeed been widely applied for the mechanical characterisation of thin and ultrathin polymeric, composite, and metallic supported

thin films [41, 70, 126–128], as it overcomes the difficulties associated with handling these films and the limited sensitivity typical of conventional methods [127]. We focus on applying the same process but in a time resolved manner, aiming to evaluate how the mechanical properties of thin films evolve upon drying under controlled conditions (e.g. temperature and relative humidity). In this way we develop a method that can be exploited for applications ranging from paints to personal care products.

***

This thesis is organised as follows. Chapter 2 details the experimental methodologies utilised. Chapter 3 explores pattern formation via PDMS vitrification induced by plasma oxidation. Chapter 4 presents strategies to enlarge the limits of PDMS oxidation and accessing sub-100 nm wrinkles. Chapter 5 focuses on wrinkling of bilayers obtained by means of ultra-violet ozonolysis oxidation of PDMS whilst Chapter 6 explores the origins of double frequency sinusoidal patterns. Chapter 7 presents the exploitation of wrinkling as a method to dynamically characterise the mechanical properties of thin, drying films. Chapter 8 summarises the findings obtained and explores future possible applications of this work.

Chapter 2

Experimental Methodologies

2.1 Wrinkling experiments

2.1.1 Substrate preparation

As discussed in Chapter 1, we chose polydimethylsiloxane(PDMS) as the substrate for wrinkling experiments. We utilised the kit Sylgard 184 (Dow Corning), comprising a liquid pre-polymer base and a crosslinker. The two components were mixed at a selected mass ratio (the precision of the weight measurements was within ± 0.001 g, performed with a Sartorius 1702 balance). The typical ratio chosen was 10 g of elastomer per gram of crosslinker (10:1): however, this ratio was varied in selected experiments to increase the PDMS elastic modulus, where lower ratios correspond to stiffer substrates [109, 129, 130]. After stirring for ≈ 5 minutes, the mixture was placed in a plastic desiccator and left under vacuum for 15 minutes to remove the residual bubbles and then deposited onto a glass surface, to have a thickness of ≈ 2 mm. Thermal curing was carried out for 3 hours at ambient temperature followed by 1 hour in a convection oven (Binder, FD 56), generally at 75 °C. In selected experiments, the curing temperature as well as the duration were varied to tune the stiffness of the substrate [109, 129, 130].

2.1.2 Surface oxidation

The PDMS surface was oxidised by means of plasma or ultraviolet ozonolysis exposure. Two different chambers were utilised for the purpose of plasma oxidation: a Harrick Plasma Cleaner (PDC-002, Figure 2.1) and a Diener Plasma Oven (FEMTO, Figure 2.2). The Harrick plasma cleaner is able to generate an oscillating electric field with a frequency of 8-12 MHz and is usually referred as *MHz* chamber. It has three power settings (30, 10 and 7 W) and is equipped with a pressure sensor as well as two gas inputs with flowrate controls which can be mixed at the desired proportions. The Diener chamber is referred as *kHz* as it has a nominal frequency of 40 kHz. It is equipped with a single gas input, flowrate control and power settings ranging from 10 to 99 W. Both chambers are linked to vacuum pumps. The samples to be oxidised via plasma, were placed in one of the chambers, which was then evacuated down to $\approx$ 0.2 mbar. The ionising gas (air, or oxygen and/or nitrogen) was then allowed to flow within the chamber for 5 minutes at the maximum settable flowrate. Therefore the flowrate was reduced in order to reach the desired value of the pressure within the chamber, and the system was left until the pressure stabilised. The power (set to the desired value) was then switched on so that the gas was ionised and the plasma formed: the sample was left under exposure for the desired amount of time. However, we

FIGURE 2.1: Harrick Plasma Cleaner (PDC-002), referred as MHz chamber.

FIGURE 2.2: Diener Plasma (FEMTO), referred as kHz chamber.

found that plasma ignition did not occur when the pressure in the chamber was higher than 1 mbar (for the MHz plasma). As predicted from the Pashen's Law [131] the breakdown voltage $V_{breakdown}$, required to induce a discharge between two electrodes (at a distance d_{el}) within a gas, is related to the pressure P through

$$V_{breakdown} = \frac{B \times d_{el} \times P}{\ln\left(C \times d \times P\right) - \ln\left(\ln\left(1 + 1/\gamma_{se}\right)\right)} \tag{2.1}$$

where γ_{se} indicates the number of secondary electrons that each incident positive ion produces, whilst B and C are empirical constants typical of the gas utilised. The relation above can be plotted for air, using the coefficients given by Bazelyan [132] (Figure 2.3). We can see that as the voltage provided by the plasma chamber is fixed (220 V for the MHz plasma chamber as given from the manufacturer), there will be values of the pressure for which this is lower than the breakdown value, impeding the ignition.

In an attempt to assess the impact of higher pressure values on the PDMS surface oxidation, we overcame this intrinsic limitation. The plasma was ignited at a pressure lower than 1 mbar: thereafter the gas flowrate was rapidly increased in order to achieve the desired value of the pressure. PDMS oxidation via ultraviolet ozonolysis was carried out within a PSD Pro series NOVASCAN (Figure 2.4), equipped with a UV lamp emitting light at both 185 and 254 nm. The two wavelengths contribute to the creation of an effective oxidising atmosphere. Indeed molecular oxygen exhibits strong light absorption at 185 nm: as a result

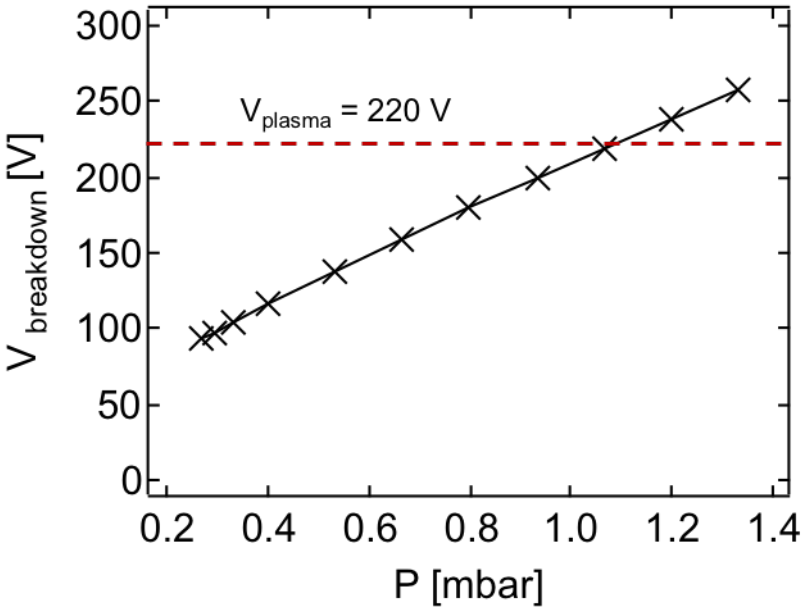

FIGURE 2.3: Breakdown voltage for air as a function of pressure according to equation 2.1. Coefficients were taken from [132]. The horizontal line indicates the constant voltage of the MHz plasma chamber.

FIGURE 2.4: UVO cleaner (PSD Pro series NOVASCAN).

it dissociates forming oxygen radicals, responsible for the production of ozone by reaction with molecular oxygen [133, 134]. Ozone then strongly absorbs light at 254 nm, dissociating back to O_2 and oxygen radicals. A dynamic oxidising environment is thus achieved within the UVO chamber. The mechanism is represented schematically below

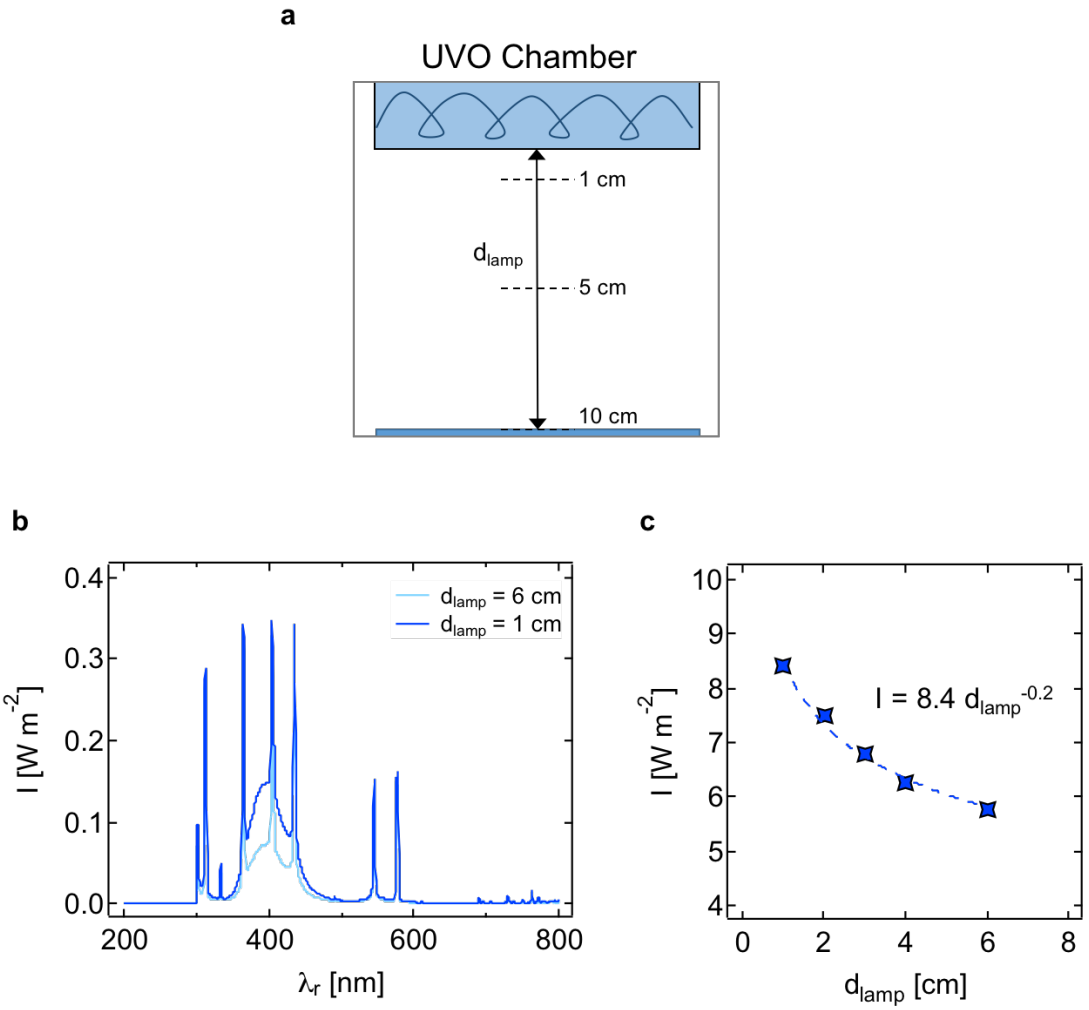

FIGURE 2.5: a) Schematic of the sample position relative to the UV lamp within the UVO chamber. The parameter d_{lamp} is utilised to express the distance between the sample and the UV lamp, and varies between 1 (minimum distance) and 10 cm (maximum distance). b) Light emission spectra in the range of 300-900 nm wavelength for two values of d_{lamp}. c) Measured integral intensity of the light emitted by the source in the UVO chamber as a function of d_{lamp}. The line represents a power fit to the data, according to the equation $I = I_1 d_{lamp}^a$ with fitting parameter a = -0.2 ± 0.01 and I_1 = 8.4 W m^{-2} the maximum intensity measured at d_{lamp} = 1 cm.

$$O_2 \longleftrightarrow 2\,O^{\cdot}$$

$$O_2 + O^{\cdot} \longleftrightarrow O_3$$

$$O_3 \longleftrightarrow O_2 + O^{\cdot}$$

The sample to treat was simply placed in the chamber, operated at ambient temperature and pressure, and oxidised for controlled times. Apart from the exposure time, the distance from the lamp was varied (defined according to the schematic in Figure 2.5a), as it impacts the light intensity thus affecting the number of radical species present. By using a BLACK-Comet UV-VIS Spectrometer coupled with SpectraWiz software (Stellar Net Inc.), we acquired the light spectrum in a range of 300-900 nm wavelength, at different values of d_{lamp}. Figure 2.5b shows two selected spectra, from which it is evident the intensity decrease at increasing d_{lamp}. Figure 2.5c shows the intensity, evaluated as the integral of the spectra, as a function of d_{lamp}. According to the inverse square law, one should expect that $I \propto d_{lamp}^{-2}$ [135]. This relationship, however, is derived with the assumption of a point source. In the case of the UVO chamber the lamps are rather high-aspect-ratio cylindrical tubes, resulting in a less sharp dependence [136]: indeed by fitting the data we find $I \propto d_{lamp}^{-0.2}$. The derived relationship represents a valuable tool in predicting the intensity from a simple geometrical measurement.

2.1.3 Strain application

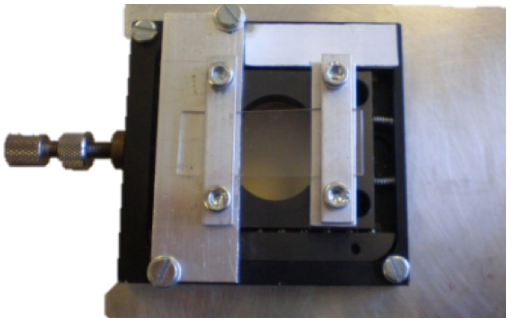

FIGURE 2.6: Uniaxial strain stage utilised. A PDMS coupon is clamped and stretched by means of the screw.

As discussed previously, wrinkling was induced on bilayers by means of mechanical strain. A uniaxial stage was employed (Figure 2.6), where the sample was clamped

and stretched through a screw. We indicate with x the strain direction whilst y is the direction orthogonal to x on the sample surface plane. The stretching could be performed prior or after the substrate oxidation. In the first scenario, the substrate was uniaxially stretched, then oxidised (leading to bi-(multi-)layer formation): surface patterns oriented along y arose upon compression in the x direction, occurring when releasing the strain. These are referred as 'ON samples', as they show wrinkles in their relaxed state. For ON samples, the applied strain $\epsilon_{prestrain}$ is computed by comparing the initial distance between the clamps L_1 to the value measured after stretching L_0 as

$$\epsilon_{prestrain}\% = \left(1 - \frac{L_1}{L_0}\right) \times 100 \tag{2.2}$$

where the lengths are measured with a precision of ± 0.01 mm.

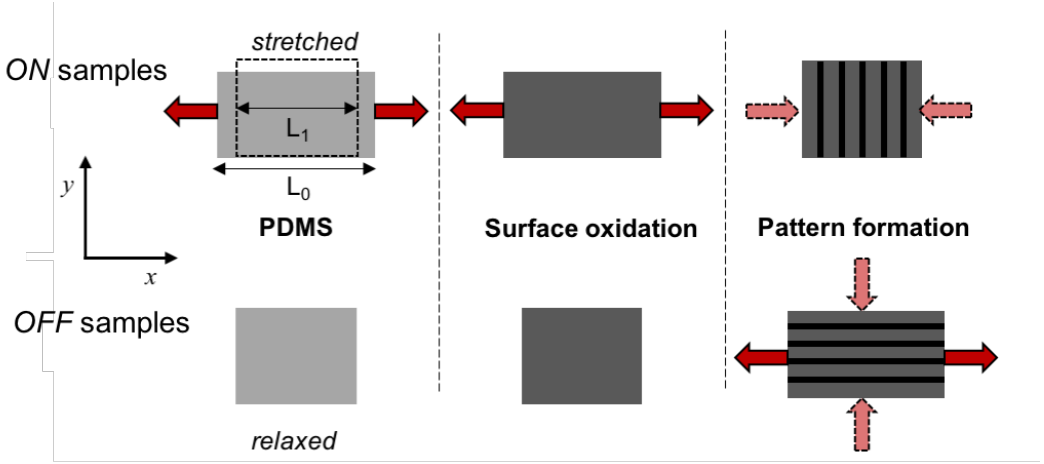

FIGURE 2.7: Schematic of the procedures employed to obtain ON or OFF wrinkled samples

As opposed to ON samples, OFF samples were subject to strain upon bi-(multi-)layer formation. After the oxidation treatment, the coupons (whose surface appeared as 'flat') were stretched by means of the strain stage. By stretching along x, compression occurs in the y-direction, leading to patterns oriented parallel to x. The compression can be related to the extent of stretching by recalling the definition of the Poisson's ratio which in this case yields $\nu = \epsilon_y/\epsilon_x$. If we take $\nu_{PDMS} \approx 0.5$ it is evident that the OFF samples have a limitation in terms of the applicable strain compared to ON samples. The wrinkling experiments performed

in this work are related to ON samples, unless otherwise stated. The procedures to obtain both ON and OFF samples are depicted in Figure 2.7.

2.1.4 Acquiring wrinkle morphology data

2.1.4.1 Optical microscopy

Optical microscopy in reflection mode (Olympus BX40) was employed to obtain 2-D images of the patterned surfaces, thanks to the optical transparency of the PDMS coupons. Depending on the pattern morphology, lenses with magnification 5×, 10×, 50× or 100× were utilised. Analyses on the acquired images were performed using ImageJ, allowing the extraction of the average value of the wrinkles' wavelength expressed in pixel. Each lens was calibrated in order to have a rigorous correspondence between the dimensions in pixels and the real dimensions: the calibration factor was obtained by imaging diffraction gratings with periodicities of known values.

2.1.4.2 Atomic Force Microscopy

Imaging through optical microscopy, albeit sufficient to simply obtain a first indication of the surface morphology, showed two main disadvantages. The resolution was limited by the magnification of the lenses available, thus only pattern wavelengths ≥ 1 μm could be accurately determined. Moreover, the 2-D image did not allow for amplitude quantification, requiring alternative techniques such as Atomic Force Microscopy (AFM) or stylus profilometry [137, 138].

We extensively employed AFM, by means of a Veeco/Bruker Innova scanning probe. For morphology measurements, AFM was employed in tapping mode. As shown in the schematic in Figure 2.4, the sample surface is scanned by a probe tip (Si) supported by a cantilever. Whilst scanning, the probe tip deflects a laser beam and the deflection is recorded by a detector sensitive to the position. The information recorded through the probe movement is translated into 3-D micrographs which allow for λ and A to be extracted through the NanoScope

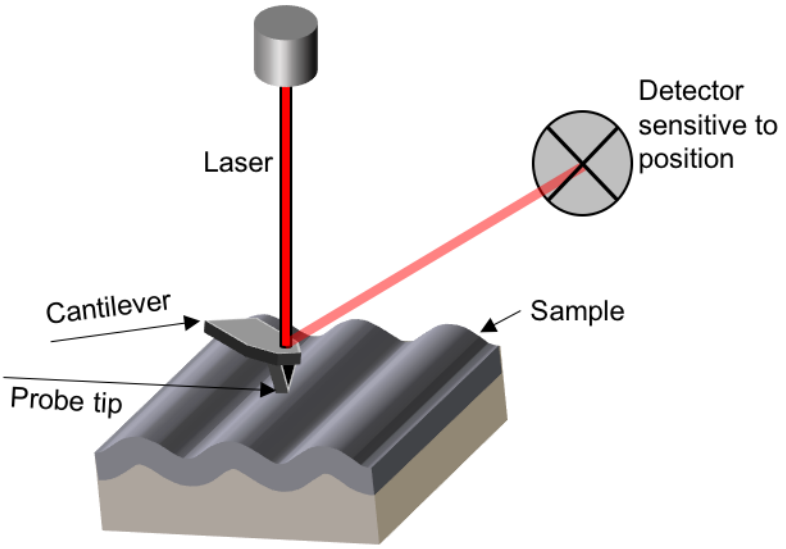

FIGURE 2.8: Schematic of the AFM microscope employed for the morphological characterisation of wrinkled samples.

analysis software accompanying the microscope. We employed Si tips (MPP-11100 W, Bruker) with a spring constant within 20-80 N/m and resonant frequency between 200-400 kHz.

Measurements were usually performed at the minimum scanning frequency of 0.1 Hz, and PID controller parameters tuning the distance tip/surface were adjusted and optimised for each sample in order to maximise the quality of the images obtained (generally, P was varied between [0.2-3], I [0.5-0.8] and D $\approx$ 0.0001). To verify the goodness of the selected parameters, surface height profiles were recorded both for forward and backward scanning.

AFM, therefore, overcomes the limitations highlighted for optical microscopy, leading to accurate and complete morphology characterisation down to the nano-scale. However, the equipment we utilised was designed to scan a maximum area of 100 μm^2, thus being not suitable to accurately characterise patterns with lateral dimensions bigger than $\approx$ 20 μm.

2.1.4.3 Surface Profilometry

Due to the 'area' limitations of the AFM, surface profilometry can be of use to measure both the wavelength and amplitude of patterns in the 10-few hundreds microns range. We employed a Bruker DektakXT DXT profilometer, equipped with a diamond stylus of 12.5 μm radius. The stylus moves vertically and laterally across the selected area of the sample, with a specified contact force of 1 mg (chosen in order to minimise any damage to the sample). A digital signal is generated from the stylus displacement, which is then stored and displayed in the form of a surface profile.

2.1.5 Estimation of the uncertainty

Morphology data acquired are affected by an error which results from multiple factors. First of all, it has to be noticed that the dimensions of the wrinkles may slightly vary across the area of a selected sample. The values reported in the result sections therefore represent the average of N measurements on a portion of the sample, chosen to be approximately one order of magnitude bigger than the characteristic wavelength. Moreover one has to consider that λ and A depend on a number n of process parameters p_i (e.g. strain, exposure time and pressure when using PDMS oxidation to create the bilayer), whose measurement is affected by an error $u(p_i)$. As a result, the error on A (or equally λ), $u(A)$, is estimated as

$$\left(\frac{u\left(A\right)}{A}\right)^2 = \sum_{i=1}^{N} \frac{1}{N}\left(\frac{A_i - A_{average}}{A_{average}}\right)^2 + \left(\frac{1}{A}\left(\sum_{i=1}^{n}\frac{\partial A}{\partial p_i}u\left(p_i\right)\right)\right)^2 \tag{2.3}$$

2.2 Depth profile measurements

In order to establish the limits of wrinkling for soft matter patterning, it was necessary to deepen the understanding of the PDMS frontal vitrification process, occurring as a consequence of surface oxidation. This was achieved by employing X-ray and neutron specular reflectivity, allowing for the determination of the depth

profile in the regions near the surface. Thanks to these non-destructive techniques we can characterise thin film structures [139–142] (up to few hundreds of nm thickness [143, 144]) with sub-nm resolution.

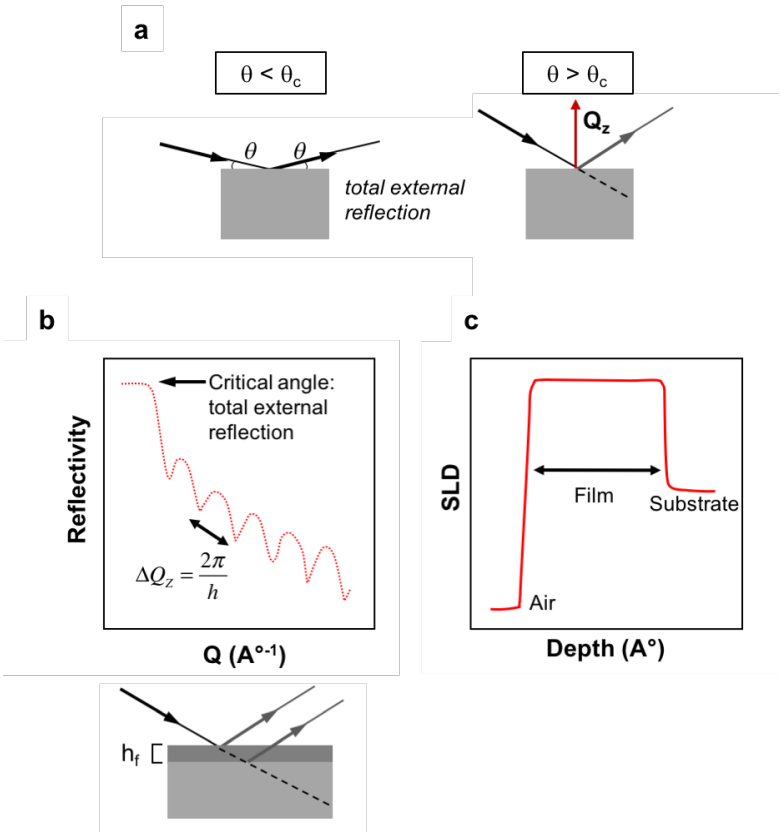

FIGURE 2.9: a) Schematic of a substrate analysed by means of specular reflectivity. The incident beam impacts the sample at an angle θ, and the reflection at the same angle is captured by a detector. If θ is lower than the critical angle θ_c we have total external reflection, whilst when $\theta > \theta_c$ only a portion of the incident radiation is reflected. b) Schematic of the reflection in case of a thin film/substrate system. The beam is reflected at both interfaces: interferences result in oscillations, known as 'fringes', in the reflectivity profile. The Q difference between two consecutive fringes is related to the film's thickness h_f. c) Typical SLD profile obtained from fitting the reflectivity data, in case of a single film sandwiched between air and a solid substrate.

In specular reflectivity, an X-ray (or neutron) beam, oriented at an angle θ, impacts the selected sample. If θ is lower than a critical value, θ_c, then the intensity of the incident beam is equal to the intensity of the reflected beam. This is referred to as *total external reflection* and θ_c depends on the material under analysis. For $\theta > \theta_c$, the beam is reflected and trasmitted; a detector then measures the intensity of the reflected beam in the specular direction (e.g. when the reflection and the incident

angles are equal). The angle θ is related to the momentum transfer Q through $Q = 4\pi \sin(\theta)/\lambda_r$, with λ_r being the wavelength of the radiation source employed (Figure 2.5a). The reflectance R, defined as the ratio between the reflected and incident beam intensities, is then expressed in terms of the component of the momentum transfer orthogonal to the reflecting surface Q_z as

$$R = \frac{16\pi^2}{Q_z^2}|SLD'(Q_z)|^2 \propto \frac{1}{Q_z^4} \tag{2.4}$$

where $SLD'(Q_z)$ indicates the Fourier transform of the gradient of the scattering length density (SLD) profile orthogonal to the reflecting surface [145]. The scattering length density essentially expresses the extent to which a material can scatter the incident radiations. It is defined as

$$SLD = \frac{\rho N_a \sum_{i=1}^{N} b_i}{\sum_{i=1}^{N} M_i} \tag{2.5}$$

where N_a is the Avogadro number, ρ is the bulk density of the material and b_i and M_i are respectively the scattering lengths and molecular weights of the N atomic species constituting the sample.

When dealing with multiple interfaces (as in the case of bi-(multi-)layers), each one reflects the beam and the different reflections interfere with each other, resulting in oscillations known as 'Kiessig fringes' [146]. In case of a thin film at a solid/air interface, the thickness can be estimated by the Q_z difference between two consecutive fringes ΔQ_z through $h_f = 2\ \pi/\ \Delta Q_z$ (Figure 2.5b). Although the film thickness can be readily determined, in first approximation, from the acquired reflectivity profile, extracting the full depth profile requires a more detailed and complex analysis (Figure 2.5c). Optical matrix methods are normally employed, where the sample is modelled as a defined number of stratified layers. Three parameters describe each layer, which are namely thickness, scattering length density SLD and interfacial roughness. The latter has to be taken into account as, in practice, nearly all the surfaces have imperfections and these affect the reflectivity profile, which appears to drop at a higher rate (compared to $1/Q_z^4$)

with dampened fringes at high Q_z values. These effects are taken into account by adjusting equation 2.4 with a Debye-Waller type factor [145, 147], which has the form

$$R_{rough} = Re^{-\frac{Q_z^2\sigma^2}{2}} \tag{2.6}$$

where σ is the root mean squared roughness (RMS).

There are currently a number of programs where these matrix methods have been implemented: we analysed the acquired curves using Motofit [148] and RasCal [149]. The value of the SLD (for X-ray) for neat PDMS was determined by simulating the corresponding reflectivity profiles assuming a single layer at air interface ($\text{SLD}_{air,X-ray}$= 0). We found $\text{SLD}_{PDMS,X-ray}$ = 9.61 × 10 $^{-6}\mathring{A}^{-2}$, which agrees with the value computed by considering the density and chemical structure of the polymer (repeating unit SiC_2H_6O, $\rho \approx 0.97\ gcm^{-3}$ [150], $\text{SLD}_{PDMS,X-ray}$ (calculated) = 9.23 × 10 $^{-6}\mathring{A}^{-2}$). Neutron reflectivity profiles acquired on PDMS samples were non-trivial to analyse, as the scattering is not significant because of no significant contrast with air. As a result, the PDMS neutron SLD was calculated from its density and chemical structure, obtaining a value of $\text{SLD}_{PDMS,neutron}$ = 6.35 × 10 $^{-8}\mathring{A}^{-2}$. The reflectivity profiles acquired for plasma oxidised PDMS were modelled considering a single layer sandwiched between air and the bulk PDMS: both the thickness (ranging between 1 to 20 nm) and the SLD profile were inferred from the curves' fittings. The SLD of the oxide layer was set to vary between the value of PDMS and the one of silica ($\text{SLD}_{SiO_2,X-ray}$ (calculated) = 2.3 × 10 $^{-5}\mathring{A}^{-2}$; $\text{SLD}_{SiO_2,neutron}$ (calculated) = 3.8 × 10 $^{-6}\mathring{A}^{-2}$). From the profiles obtained we could gain a deeper understanding of the mechanisms of film formation and densification, with an accuracy which is not found in other techniques. One thing to point out is that, in fitting the reflectance curves, the SLD and thickness are generally coupled, meaning that there are several combinations of the two parameters that can fit the curve. In order to decouple the two parameters and get an independent and reliable estimate of the thickness and SLD of the oxide layer the following strategy was adopted. At fixed process conditions, an estimate for

the thickness was obtained from the morphological characterisation of samples in their wrinkled state: a lower and upper bounds for h could then be assigned in the fitting. Moreover, neutron and X-ray reflectance data acquired on the same samples were fitted simultaneously: the difference between $\mathrm{SLD}_{neutron}$ and SLD_{X-ray} was exploited in obtaining the value of the thickness.

PDMS samples, with 1 cm thickness, for X-ray reflectivity (XRR) and neutron reflectivity (NR) were prepared by mixing the elastomer and crosslinker at a ratio 10:1. The mixture was then cast onto 3 inch diameter silicon wafers (Si-Mat, Landsberg/Lech, Germany) previously cleaned by UVO exposure. After degassing and subsequent curing (as described earlier in this Chapter), the samples were gently removed from the silicon wafers and the bottom surface was analysed with reflectivity, prior and after oxidation. By doing this, we minimised the effects of the substrate roughness.

Regarding the technical aspects, X-ray experiments were carried out by means of a PANalytical X'Pert PRO MPD instrument, with a 2.2 kW Cu/W/Si anode source emitting radiations with wavelength $\lambda_r = 1.54$ $\mathring{A}$. The incident beam was generated (generator power of 40 kV and 40 mA) using a parabolic X-ray mirror and a divergence slit of 0.05 mm, whilst the reflected beam was detected by a beryllium detector with a parallel plate collimator, equipped with a 0.1 mm slit. The angle of the incident beam was systematically varied by means of a ω - 2θ goniometer. The samples were mounted on a motorised stage whose position could be adjusted manually in order to ensure perfect alignment between the incident beam, the sample surface and the detector. The alignment was firstly done on the direct beam: the position of the goniometer was set at 0° and a 2θ scan was performed without the sample. In absence of offsets, a peak in the intensity is recorded at $2\theta = 0°$: deviations from this value were taken into account by defining the position of the peak as 0°, thus registering the corresponding offset. The value of the intensity at the peak is defined as I_{max}. Thereafter the sample was mounted on the stage, whose z position was varied until the measured intensity was approximately half of I_{max}. At this point, the goniometer was set to $2\theta = 0.4°$ ($\omega = 0.2°$) and a ω scan was performed. Any offsets on ω were recorded.

The values of the intensity at 0.1°, 0.15° and 0.2° were then compared: in case of significant differences, the tilt and the axial position of the sample were varied in order to minimise these, flattening the critical edge thus ensuring proper sample alignment. When changing the position of the sample, the ω scan was repeated to check whether the offsets remained unvaried. Once completed the alignment procedure, the reflectivity profiles were acquired at angles ranging between 0.1° to 0.3°.

Neutron reflectivity experiments were performed at the Figaro reflectometer (Institut Laue Langevin, Grenoble) at two angles 0.723° and 2.723°. In this case, alignment of the sample was performed automatically with the aid of the instrument software. The curves acquired at the two reflection angles were then scaled and stitched together using LAMP [151]. The resulting reflectivity profile was then analysed as described previously.

Chapter 3

Frontal vitrification of PDMS via air plasma and impact on surface wrinkling

Taking into account the considerations made in Chapter 1, to establish wrinkling as a scalable and cost-effective method for soft matter patterning, we start by studying the surface oxidation of polydimethylsiloxane (PDMS) by plasma exposure and its implications for the mechanically-induced wrinkling of the resulting glass-elastomer bilayers. We carry out a complete set of experiments in order to assess the effect of process variables on the glassy skin thickness, and therefore on the wrinkling morphology. Specifically, we vary the prestrain, plasma frequency (kHz and MHz), pressure ($0.5 \leq P \leq 1.5$ mbar), oxygen content (from O_2 to air), as well as exposure time and power. Equipped with this knowledge, we find the optimal set of parameters which allows expanding the existing capabilities of plasma oxidation for PDMS wrinkling at the nm scale. Moreover, the observed logarithmic dependence of the pattern dimensions on the exposure time allow for the modelling of the oxidation reaction. We therefore obtain a predictive tool to infer the wrinkling characteristic dimensions corresponding to selected process conditions. The results presented and discussed in this Chapter have been published in [152].

3.1 Methodology

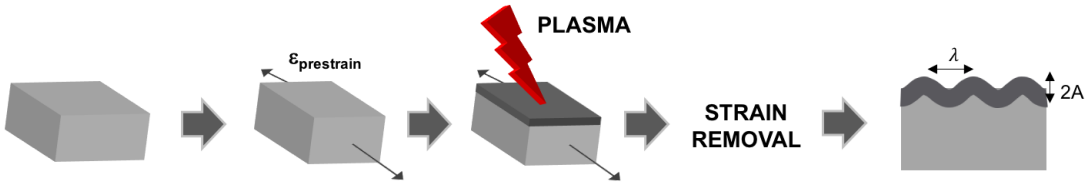

FIGURE 3.1: Formation of wrinkles on SiO_x-PDMS bilayers obtained by plasma oxidation: a neat PDMS specimen is pre-strained uniaxially by $\epsilon_{prestrain}$, exposed to plasma (for various gas mixtures, frequency, power, pressure and time), and then allowed to relax, forming sinusoidal wrinkling patterns with prescribed λ and A from which the glassy skin thickness h can be measured.

PDMS slabs of ≈ 2 mm thickness were obtained following the procedure detailed in Chapter 2. The slabs were cut into 1 cm $\times$ 2 cm coupons and stretched by $\epsilon_{prestrain}$ via a uniaxial strain stage. The stretched PDMS specimen was then placed in one of the plasma chambers (with kHz or MHz frequency, as detailed in Chapter 2) for oxidation, removed and released from strain, resulting in permanently wrinkled samples in the relaxed state for profile analysis. The experimental procedure is depicted in Figure 3.1.

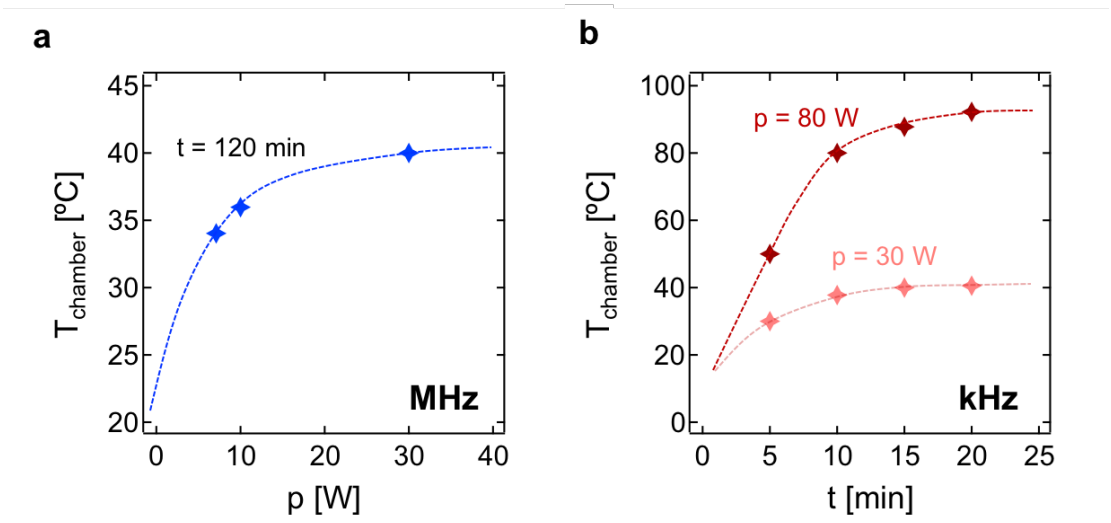

FIGURE 3.2: Plasma chamber temperature (a) within MHz air plasma chamber after 2 hours of operation, as a function of the induction power; (b) within kHz air plasma chamber as a function of time for two representative induction powers. The lines are guides to the eye.

It is important to notice that the temperature within a plasma chamber increases during exposure. Combined with glassy skin formation, the surface expansion

(upon heating) and contraction (upon cooling) can result in spontaneous, generally non-isotropic, wrinkle formation. Since the focus of this study is on mechanically-induced wrinkling, we quantify the temperature changes within the plasma chamber and evaluate a possible impact on surface topography. The plasma chamber temperature was thus monitored as a function of air plasma frequency (kHz, MHz), power (7 - 80 W) and duration (0 - 7200 s) using a calibrated thermocouple. These results are shown in Figure 3.2. We find the maximum chamber temperature to be 40 °C after 2 h exposure at the highest MHz air plasma induction power. Similar values are observed within the kHz air plasma at 30 W, which however reaches up to 90 °C at 80 W. Considering the thermal expansion coefficient of PDMS ($3.2 \times 10^{-4\circ}C^{-1}$[153]), the maximum thermal strain for the MHz plasma was estimated to be $\epsilon_{max} \approx 0.6\%$ at $T_{chamber} = 40$ °C. To evaluate the contribution of thermal effects on surface topography, we measured by AFM a PDMS surface exposed to air MHz plasma for 2 hours at $p = 30$ W in the absence of mechanical prestrain (Figure 3.3a) and a fresh PDMS surface (Figure 3.3b). These are confirmed to be effectively identical within measurement uncertainty, and no thermally-induced wrinkling is observed, meaning that the thermal strain is lower than the critical strain required for pattern formation.

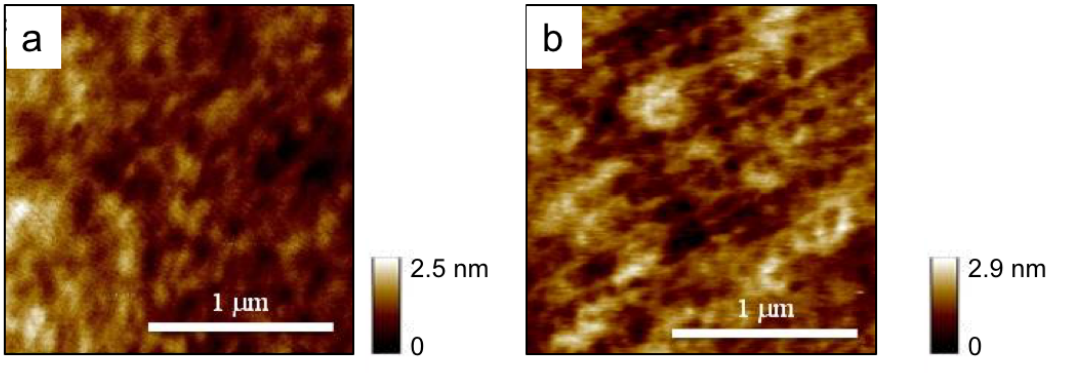

FIGURE 3.3: AFM topography images of (a) PDMS surface exposed to an air MHz plasma with induction power $p = 30$ W for 120 min, in the absence of pre-strain and (b) an unoxidised PDMS surface.

Similar results apply to the kHz plasma at $p = 30$ W, as the chamber reaches approximately the same maximum temperature. However at higher induction powers, the maximum temperature attained corresponds to more significant strain

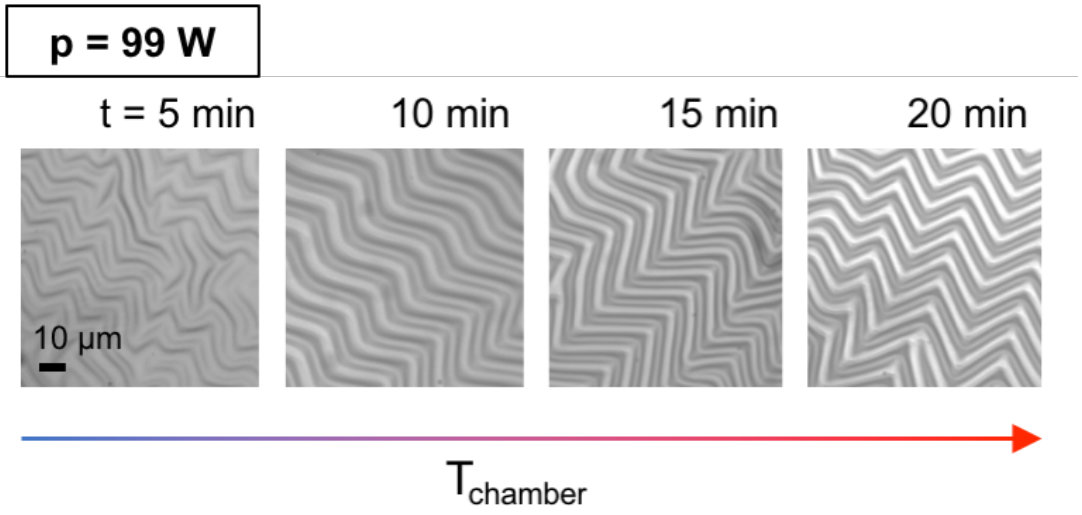

FIGURE 3.4: Formation of non-isotropic wrinkles on un-stretched PDMS exposed to kHz plasma at the maximum induction power of the chamber $p = 99$ W, for times ranging between 5 to 20 minutes.

($\epsilon_{max} \approx 2\%$). As a result, non-isotropic wrinkling is observed, in absence of any mechanical stretch, accompanied by significant surface cracking (Figure 3.4). These experiments were carried out for completion as exposure times employed in our study at such high power are much shorter, thus thermal effects on wrinkling morphology are negligible. Nevertheless, they prove the possibility of fabricating surfaces with 2-D patterns in the micron range by employing PDMS plasma oxidation, under specific conditions.

3.2 Impact of process variables on wrinkle morphology

3.2.1 Effect of prestrain

As discussed in Chapter 1, when strain is applied to a bilayer, wrinkling instabilities arise that can eventually result in sinusoidal pattern formation. In our experiments, this implies that we can induce sinusoidal wrinkling if $\epsilon_{prestrain}$ exceeds the critical strain, depending on the moduli contrast between the bulk PDMS and the oxide layer formed upon surface oxidation. At sufficiently low values of

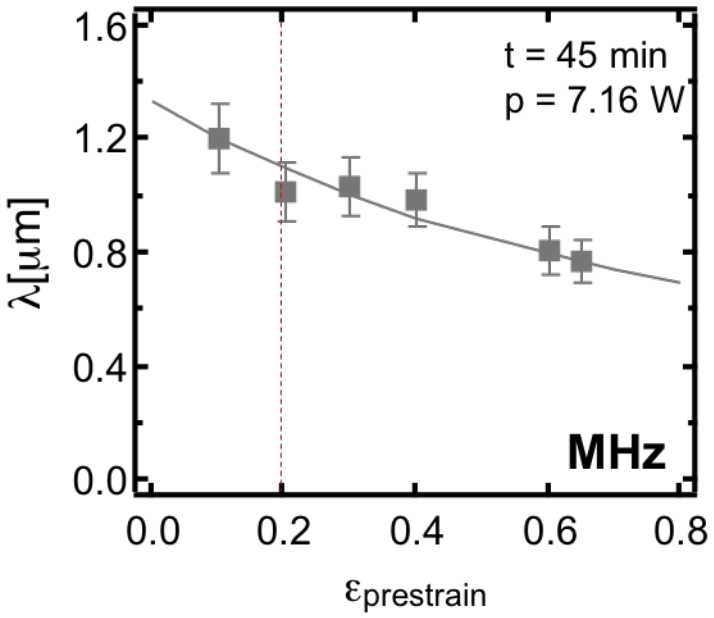

FIGURE 3.5: Dependence of the experimental wrinkle wavelength (λ) on prestrain $\epsilon_{prestrain}$ applied prior to MHz air plasma exposure at a constant pressure of $P \approx 0.93$ mbar, power $p = 7.16$ W and $t = 45$ min. The line is a fit to equation 3.1, with fitting parameter λ (at ideal conditions of 0% strain) = 1.4 ± 0.09.

prestrain the bilayer equations [1] presented in Chapter 1 hold [43, 46, 47]: the amplitude varies with prestrain according to $A \propto \epsilon_{prestrain}^{(1/2)}$ whilst the wavelength is practically independent of $\epsilon_{prestrain}$. However, beyond the limit of low deformation [138, 154–158], corresponding to $\epsilon_{prestrain} \gg \epsilon_c$ both the wavelength and the amplitude have been found to depend on the strain applied. The following expressions have been derived [156] for the wrinkle dimensions in the high deformation regime (λ_{HD}, A_{HD})

$$\lambda_{HD} = \frac{\lambda}{(1+\epsilon)\,(1+\xi)^{1/3}} \tag{3.1}$$

$$A_{HD} = \frac{A}{(1+\epsilon)^{1/2}\,(1+\xi)^{1/3}} \tag{3.2}$$

where λ and A are respectively the wavelength and amplitude as computed with the bilayer model, whilst $\xi = 5\epsilon(1+\epsilon)/32$. At even higher deformations, it has been previously reported that wrinkling is no longer sinusoidal, as higher modes

[1] $\lambda = 2\pi h(\bar{E}_f/3\bar{E}_s)^{1/3}$ and $A = h(\epsilon/\epsilon_c - 1)^{1/2}$

and folding eventually dominate [42, 53–60, 60, 62, 63] and the linear relationship between the wavelength and thickness no longer holds.

We carried out a set of control experiments, where we assessed the impact of variable prestrains between 10% to 65% on PDMS specimens oxidised via air plasma exposure at fixed process conditions (e.g. MHz chamber, P = 0.93 bar, p = 7.16 W). Figure 3.5 shows the resulting wrinkling wavelength as a function of $\epsilon_{prestrain}$. The experimental data were fitted to equation 3.1 where the single fitting parameter λ was obtained through data regression. In order to compare different plasma exposure conditions, we opt to select a constant value of $\epsilon_{prestrain} \approx 20\%$ that exceeds ϵ_c, while remaining relatively low to ensure sinusoidal wrinkling mode (Figure 3.6). By substituting this value of prestrain into equation (3.1), one obtains

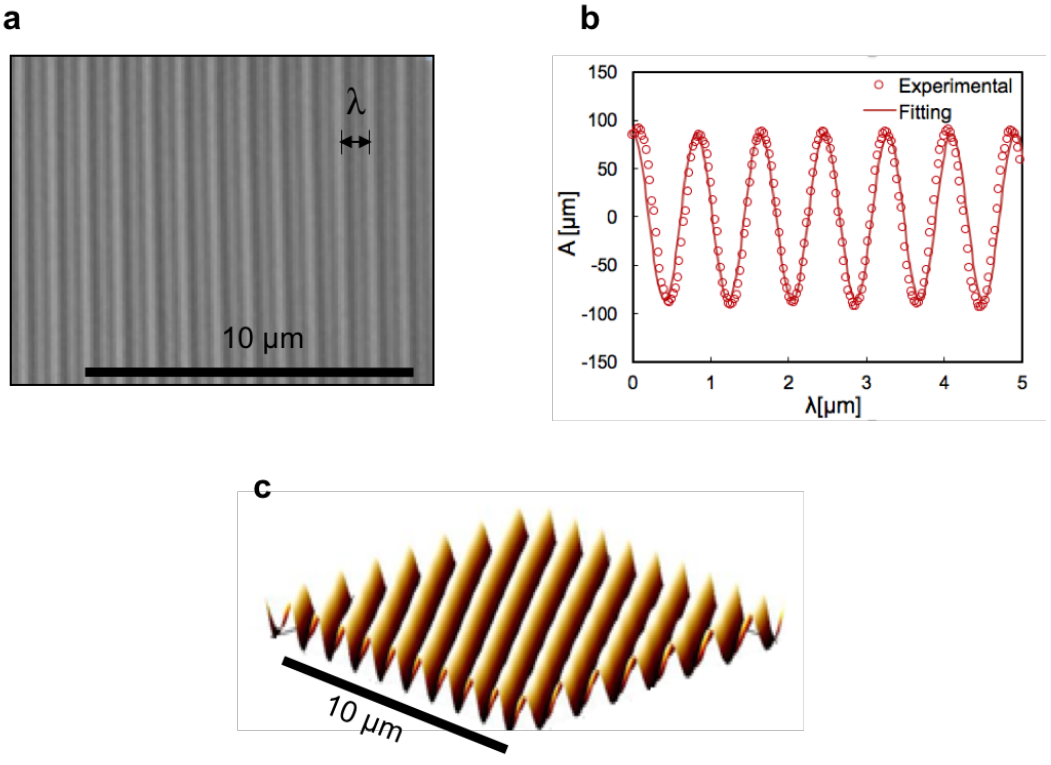

FIGURE 3.6: Representative wrinkling pattern obtained by plasma exposure of a PDMS specimen upon relaxation of uniaxial strain (air, MHz plasma, t = 50 min, p = 7.16 W, $\epsilon_{prestrain}$ = 20%): a) optical microscopy image, b-c) AFM tapping mode topography and corresponding 1D section profile, and fitted sinusoidal curve.

that $\lambda_{HD}/\lambda = 0.892$, which is verified experimentally within the measurement uncertainty. This suggests that, by using the simple bilayer equations, we could

underestimate the oxide layer thickness by 20%: therefore, we use equation 3.1 to infer the thickness from wrinkling experiments.

3.2.2 Effect of frequency, induction power and exposure time

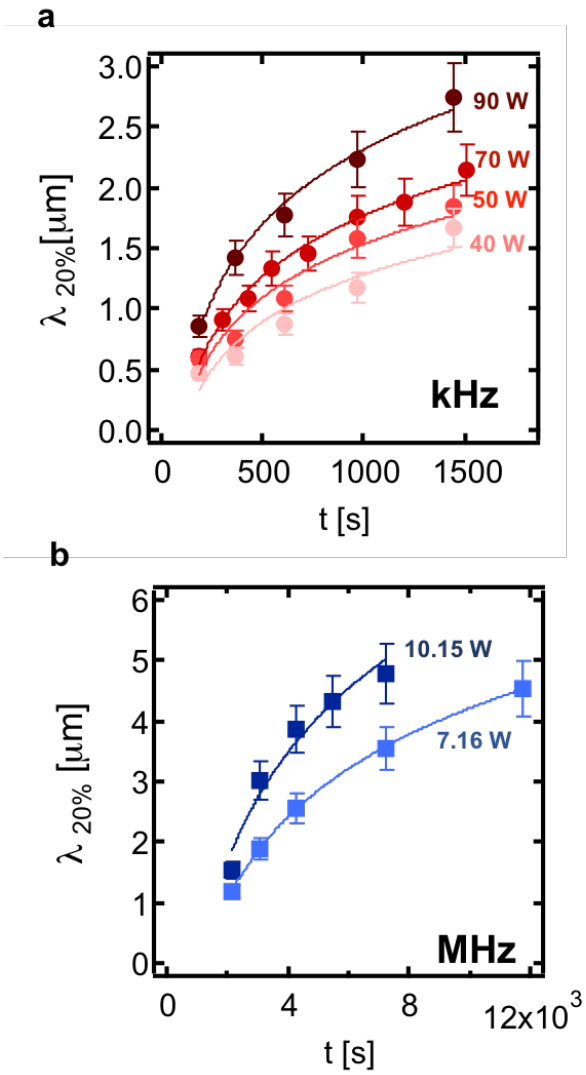

FIGURE 3.7: Wavelengths of sinusoidal wrinkles for samples prestrained by a $\epsilon_{prestrain} \approx 20\%$ and treated with (a) kHz and (b) MHz air plasmas, as a function of the exposure time for different power settings, where air pressure was kept constant at $P \approx 0.93$ mbar. The lines are logarithmic fits according to equation $\lambda = a\ln(t) + b$.

Following the procedure detailed in Figure 3.1, we oxidised PDMS samples pre-stretched by 20%, by utilising both kHz and MHz plasmas, using air as the ionising gas at pressure $P = 0.93$ mbar. Exposure time t and induction power p were tuned

in both chambers and the sample wavelength upon strain release was recorded by means of optical microscopy or AFM. Figure 3.7 summarises the results obtained. We found a logarithmic time dependence of wrinkling periodicity in all the cases investigated, which is in agreement with previous studies [90, 93]. Following earlier work on O_2 plasma oxidation of PDMS [93], we defined a new variable, namely plasma dose, as $\mathrm{D} \equiv p \times t$. By rescaling the acquired wavelength as a function of dose, we observed that the data at different p and t collapsed onto a single master curve for each plasma frequency, as shown in Figure 3.8.

In general, the impact of the process variables on the wrinkling wavelength (and amplitude) can be rationalised by recalling that λ is directly proportional to the thickness of the glassy layer, according to the bilayer model [43, 46, 47]. If the exposure time is increased (at fixed induction power), there is more time for oxygen to penetrate within the PDMS and react, leading to thicker films, thus larger λ. At constant exposure time, an increase in the induction power can lead to more radical species to be produced thus faster oxidation kinetics and increased h and λ. A similar effect can be considered for the plasma frequency: however, to appropriately quantify the effect of this variable, a more comprehensive number of chambers with varying frequencies would need to be employed. The trends observed for the wavelength result then from the dependence of the thickness h on the process variables, with λ varying between λ_{min} and λ_{max}, that correspond to h_{min} and h_{max} respectively.

3.2.3 Effect of pressure

We next consider the effect of gas pressure on the vitrification process induced by air plasma oxidation. Prestretched PDMS samples were oxidised within both MHz and kHz plasma chambers, with air pressure varying between 0.66 and 1.3 mbar. Figure 3.9 plots the wrinkles' wavelength upon strain release as a function of plasma dose for the different pressures explored. The results demonstrate that increasing pressure P decreases λ at a constant dose (illustrated in the inset, for both MHz and kHz frequencies). If we recall the proportionality between λ and the

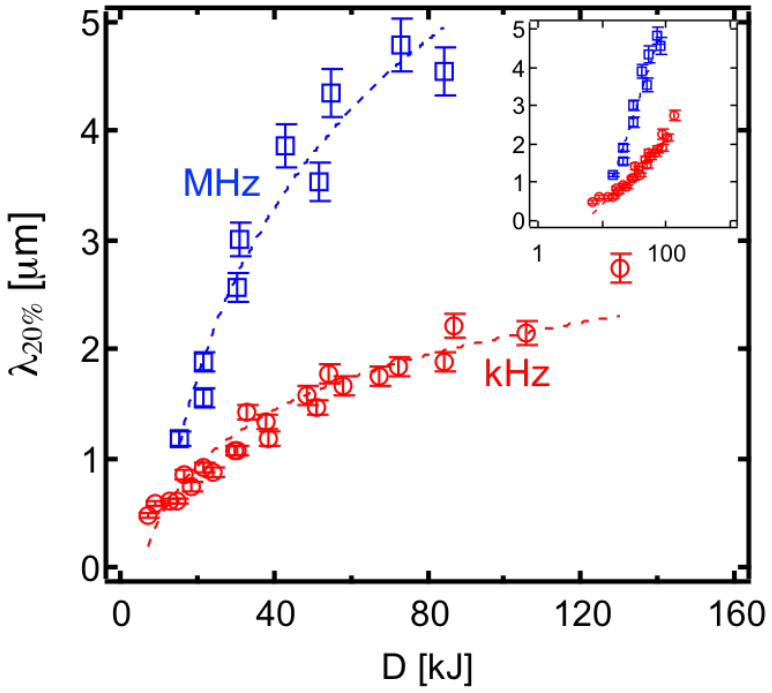

FIGURE 3.8: Wrinkling wavelengths λ of PDMS samples strained by $\epsilon_{prestrain} \approx 20\%$ and exposed to kHz and MHz air plasmas, at a constant pressure of $P = 0.93$ mbar, as a function of the plasma dose (D). The lines are logarithmic fits according to equation $\lambda = a\ln(D) + b$ ($a = 0.73 \pm 0.04$ and $b =$ -1.2 $\pm$ 0.1 for kHz, $a = 2.2 \pm 0.18$ and $b =$ -4.87 $\pm$ 0.6 for MHz). All data in Figure 3.7 collapse into single master curves for the two frequencies, well described by a logarithmic dependence. The inset shows the results in a lin-log scale.

thickness of the oxide layer h, the wrinkling experiments suggest that an increase in the plasma pressure slows down the kinetics of the oxidation reaction, yielding thinner skins. The result is not unexpected: as the collision rate in the plasma increases with pressure, the molecular mean free path decreases, which in turn compromises the ionisation process [131]. Since the oxidation reaction (leading to the formation of the glassy layer) proceeds with a radical mechanism, a decrease in the ionisation rate at higher pressures should slow down PDMS conversion and thus yield lower h (and lower wrinkling λ).

Inspired by the successful rescaling of wrinkling data at different powers p and exposure times t in terms of plasma dose D, we evaluated various rescaling variables involving pressure P. We found that, within the pressure range analysed in the experiments, all wavelength data collapse when plotted as a function of D/P, as

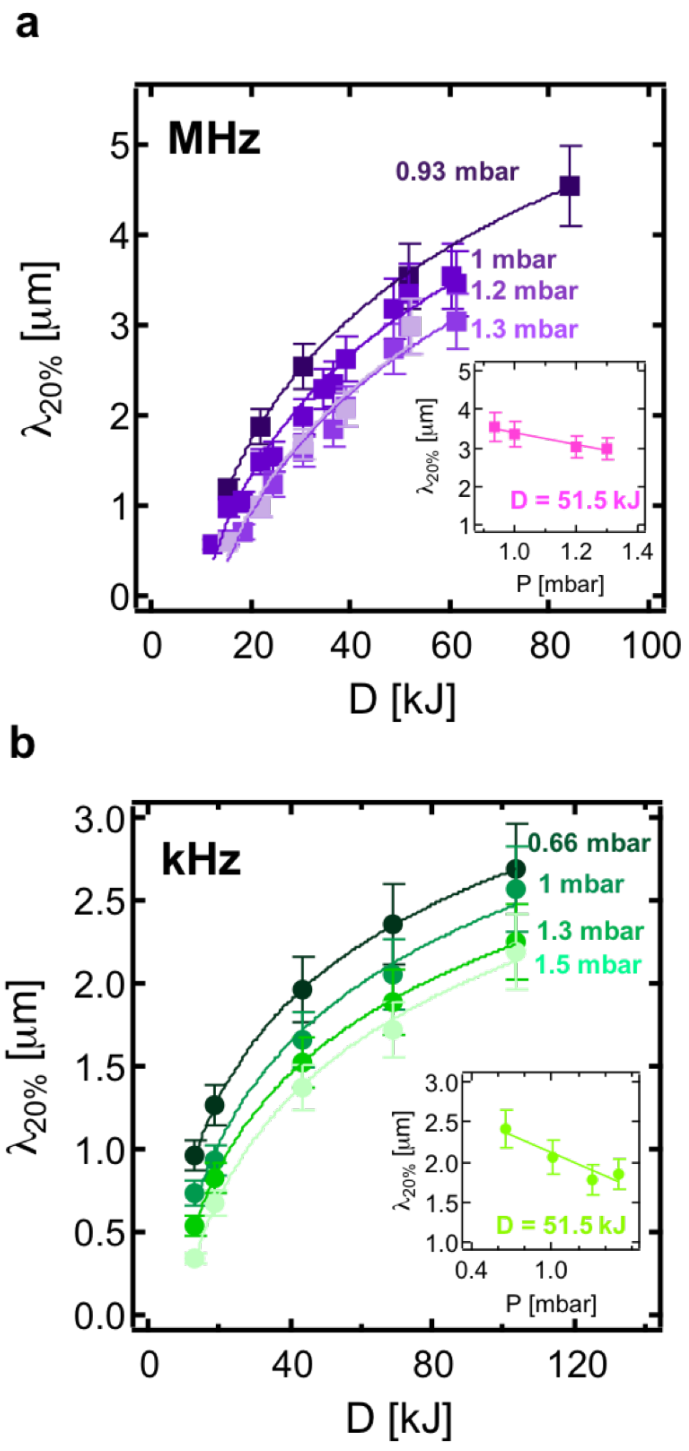

FIGURE 3.9: Sinusoidal wrinkle periodicity (λ) at 20% prestrain as a function of the plasma dose (D) for different values of air pressure (P) for (a) a MHz and (b) a kHz plasma. The lines are logarithmic fits according to equation $\lambda = a\ln(D) + b$. The inset shows dependence of λ with P at a fixed dose, which is found to be linear within this range.

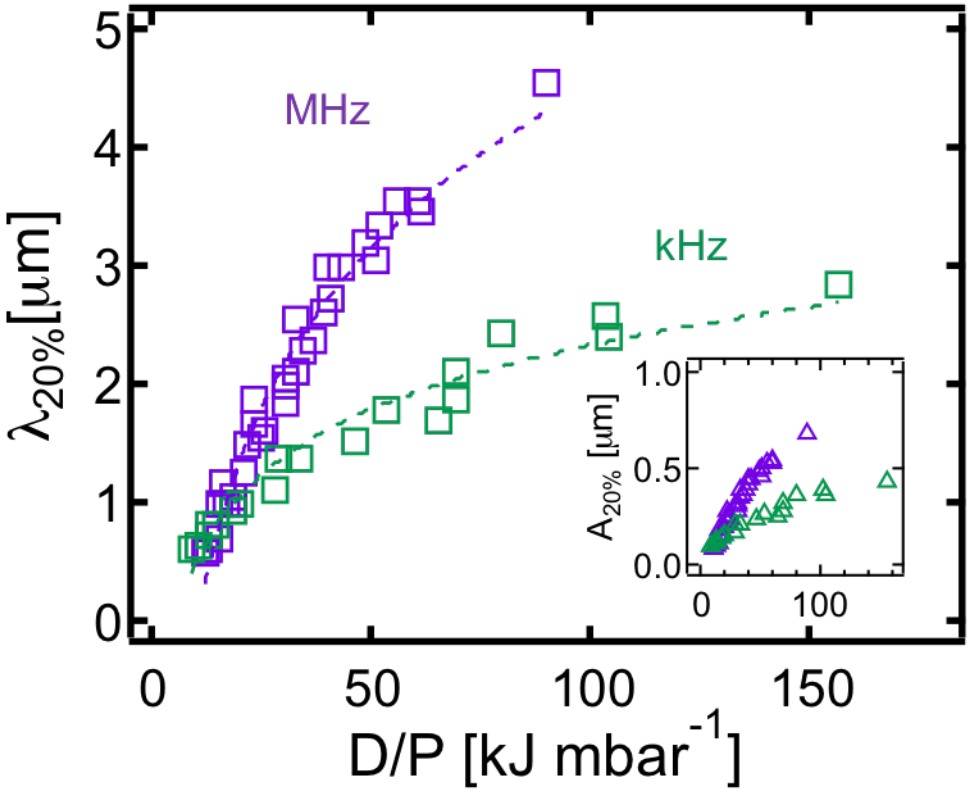

FIGURE 3.10: Wrinkling wavelengths (λ) of PDMS samples strained by $\epsilon_{prestrain} \approx 20\%$ and oxidised by kHz and MHz air plasmas, as a function of the ratio of the plasma dose/air pressure (D/P). The curves in Figure 3.9 collapse further into single master curves for each frequency. Lines are logarithmic fits according to equation $\lambda = a\ln(D/P) + b$. The inset shows the amplitude as a function of (D/P).

shown in Figure 3.10. This correlation provides useful guidance in designing the PDMS surface λ and A via plasma oxidation.

We next considered the effect of plasma pressure P on the wrinkling amplitude A, for completion. Since we found that increasing P decreases λ (and thus h), we expect the same linear dependence of the wrinkling amplitude A with the pressure, in accordance to the bilayer model. Figure 3.11 shows the wrinkling amplitude data for PDMS prestretched by $\epsilon_{prestrain}$ and exposed to air plasma in the MHz chamber and confirm our expectations. Moreover, considering the bilayer model equations [43, 46, 47] one can notice that the ratio A/λ, often referred as the *aspect ratio*, should only vary with the film's elastic modulus at constant strain. By plotting the aspect ratio as a function of D/P we can see that it does remain constant

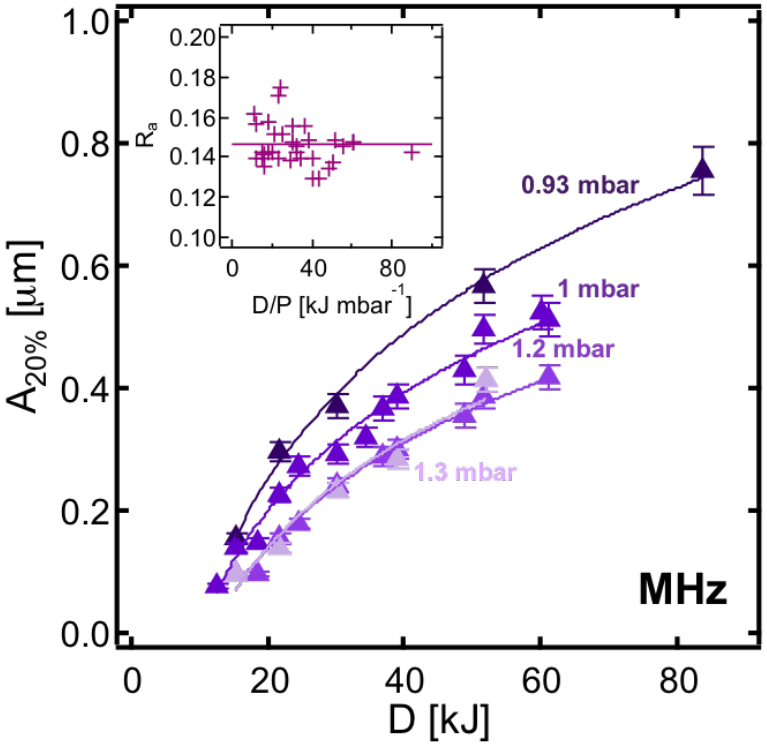

FIGURE 3.11: Sinusoidal wrinkling amplitude (A) as a function of the plasma dose (D) for different values of air pressure (P) within a MHz plasma. A constant value of $\epsilon_{prestrain} \approx 20\%$ was utilised to stretch the PDMS samples prior to plasma exposure. The lines are logarithmic fits according to equation $A = a\ln(D) + b$. The inset shows the aspect ratio A/λ as a function of D/P which is found to remain constant in this range within measurement uncertainty.

within the measurement uncertainty. These findings confirm that the pressure only affects the film thickness, whilst its mechanical properties remain unchanged, providing an effective way to tune the kinetics of the glassy skin propagation.

3.2.4 Effect of gas composition

So far all the results presented were referred to bilayers obtained via air plasma oxidation of PDMS (oxygen molar fraction in the gas $y_{O_2} \approx 0.21$) . However, previous literature studies on wrinkling of plasma oxidised PDMS employed oxygen as ionising gas [90, 92, 93, 159] . We therefore quantified the effect of the ionising gas composition on the wrinkling profile λ. To do so, the MHz plasma was operated with pure oxygen, air and an equimolar mixture of oxygen and nitrogen, at a

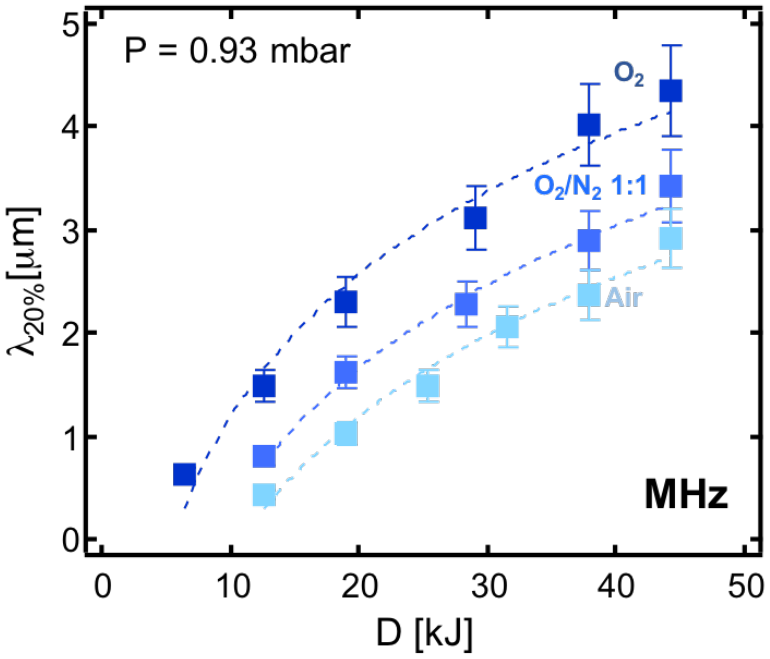

FIGURE 3.12: Wrinkling wavelengths (λ) of PDMS samples prestrained by $\epsilon_{prestrain} \approx 20\%$ and exposed to a MHz plasma, as a function of dose (D) for different ionising gases at a constant pressure of $P \approx 0.93$ mbar. Lines are logarithmic fits according to equation $\lambda = a\ln(D) + b$.

constant pressure of $P \approx 0.93$ mbar, and oxidation of prestrecthed PDMS samples was carried out at different values of the plasma dose. The wavelength of the wrinkles obtained upon strain release is plotted in Figure 3.12. We found that decreasing the concentration of oxygen results in smaller pattern dimensions, due to slower kinetics of glassy film formation. This behaviour is expected, since oxygen is the active species for the oxidation reaction which therefore slows down at lower O_2 concentrations. In practical terms, both increasing P and reducing the O_2 content, at constant plasma dose, are found to result in slower glass formation kinetics and thus thinner oxide layers and smaller pattern dimensions.

3.3 Modelling of the oxidation reaction

Thanks to the control experiments carried out, we could quantify the effect of a number of process variables on the oxide film formation via PDMS plasma oxidation, thus wrinkling morphology. The next step was to model the oxidation

reaction occurring upon plasma exposure to build a tool enabling the prediction of the pattern dimensions at selected conditions. In this study we observed a logarithmic dependence of the wrinkle wavelength, thus film thickness, with plasma exposure time, in accordance with previous studies on wrinkling of bilayers obtained through plasma oxidation of PDMS [90, 93]. The logarithmic trend suggested we could use a minimal spatiotemporal model to describe the glass formation process, borrowing concepts from well-established directional solidification via frontal photopolymerisation [11, 160, 161].

In accordance with the model, the extent of PDMS surface conversion into the glassy-like layer can be defined as $\phi(z,t)$ (corresponding to the volume of converted PDMS divided by the total volume), varying in both space and time, with the z axis being orthogonal to the top surface where it originates. We take $\phi(z,t)$ to range from 0, corresponding to neat PDMS ($\phi(z,0)$=0), to 1, indicating fully oxidised PDMS ($\phi(z,t\rightarrow\infty)$=1). The variation of $\phi(z,t)$ with time is tentatively described as [11, 160]

$$\frac{\partial\phi\left(z,t\right)}{\partial t}=K_t\left[1-\phi\left(z,t\right)\right]I\left(z,t\right) \tag{3.3}$$

with K_t being a kinetic constant (related to the oxidation reaction), and I the intensity. The latter, in case of photopolymerisation, varies with z with a non-monotonic relation which can be modelled as

$$\frac{\partial I\left(z,t\right)}{\partial z}=-\bar{\mu}\left(z,t\right)I\left(z,t\right) \tag{3.4}$$

relation which is analogous to the Beer-Lambert law [162], where $\bar{\mu}(z,t)$ is an attenuation coefficient, given by $\bar{\mu}(z,t)=\mu_\infty\phi(z,t)+\mu_0(1-\phi(z,t))$, with μ_0 and μ_∞ being the attenuation coefficients of the unconverted and fully converted material respectively. One thing to point out is that this model, yet simplified, has proven to effectively describe the polymerisation reaction occurring upon light exposure for a wide range of materials [15]. In the case of plasma oxidation, the frontal model can be applied, by considering the light intensity as the concentration

of radical species, whilst the attenuation constant can be treated as the inverse of the diffusivity of oxygen within the polymer.

Going back to the model, if $\bar{\mu}(z,t)$ is treated as a constant, assuming the oxidation reaction does not have a significant impact on the material properties, the equations can be solved analytically and an expression for the thickness of the glassy layer as a function of time can be obtained

$$h = \frac{\ln(t)}{\mu} - \frac{1}{\mu}\ln\left(\frac{1}{K_t I_0}\ln\left(\frac{1}{1-\phi_c}\right)\right) \tag{3.5}$$

where I_0 is the plasma intensity at the surface and ϕ_c is a critical value for the conversion required for film formation.

The model yields two main results:

i) First, we can see that once the oxide layer has formed, its thickness should increase with time with a logarithmic trend. If we go back to the wrinkling experiments assessing the plasma exposure time effect on the pattern wavelength, a logarithmic dependence was found. By recalling the relation between the wavelength and film thickness, we can conclude that also h depends logarithmically on the exposure time, giving us a first proof of the adequacy of the model chosen. Furthermore, we found that the plasma dose ($D \equiv p \times t$) captures the combined effects of the changing plasma power p and exposure time t, collapsing all the experimental results for λ thus h at different P and t. We can therefore rewrite equation 3.5 as

$$h = \frac{\ln(D)}{\mu} - \frac{1}{\mu}\ln\left(\frac{1}{K I_0}\ln\left(\frac{1}{1-\phi_c}\right)\right) \tag{3.6}$$

From this equation, we sought to obtain quantitative relationships for the model parameters μ and KI_0 as a function of plasma processing conditions (e.g. pressure and oxygen content). To quantify the effect of pressure, we inferred the oxide layer thickness from the wrinkling data plotted in Figure 3.9 (acquired using air as the ionising gas in both plasmas), using the modified bilayer model of equation 3.1. We thus fitted h vs. D using equation 3.6, at the different values of the pressure. The only two fitting parameters were μ and KI_0, which are plotted in

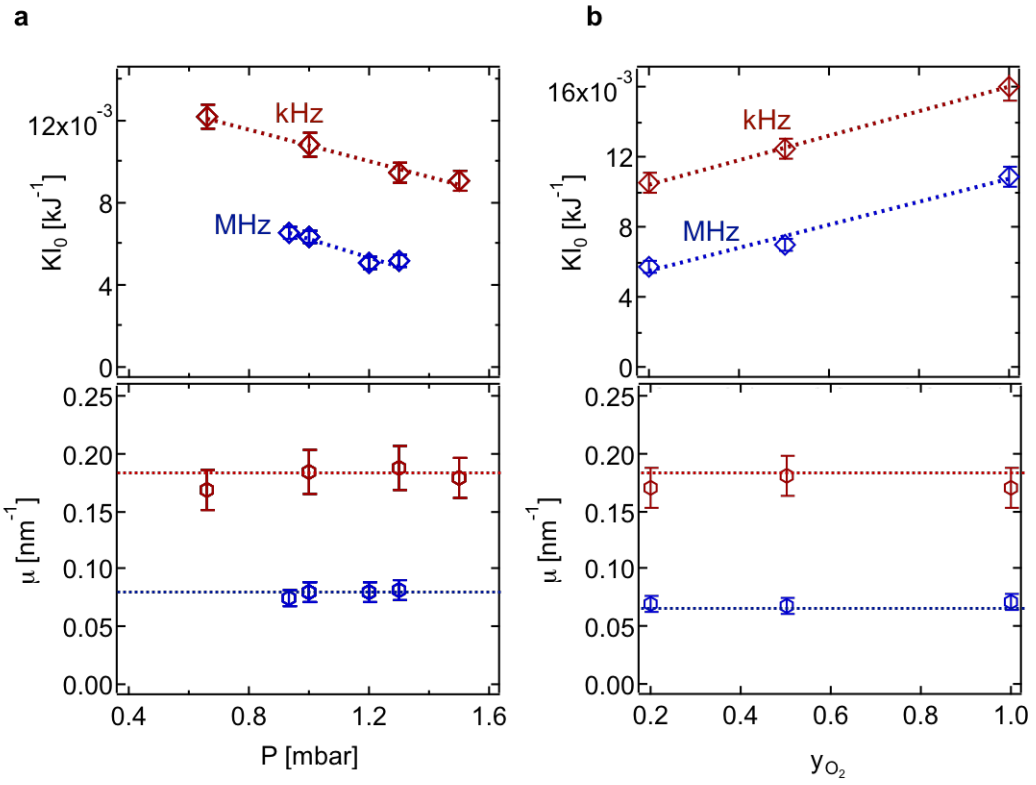

FIGURE 3.13: Pressure (a) and O_2 gas content (b) dependence of model parameters μ and KI_0, for all air plasma exposure doses and different frequencies. The parameters were computed from equation (3.5), inferring h from the λ data in Figure 3.9, 3.12 and taking $\phi_c = 0.06$.

Figure 3.13a as a function of the pressure. The ϕ_c was kept constant at 0.06 [93], but the fitting could also have been performed without assuming a value for ϕ_c and incorporating the parameter in KI_0. Evidently μ remains unchanged with P at each plasma frequency, whilst KI_0 decreases linearly with P, as expected since high pressures slow down the oxidation reaction.

Similarly for the effect of oxygen content we fitted the oxide layer thickness, inferred from wrinkling data of Figure 3.12 (acquired at constant pressure $P = 0.93$ mbar), and obtained μ and KI_0 for different values of the oxygen gas content. Interestingly, as shown in Figure 3.13b, the model parameter μ appears insensitive to gas composition, while KI_0 increases linearly with the O_2 content y_{O_2}, as a higher number of active species results in faster kinetics. Combining the findings above we can conclude that only plasma frequency, kHz or MHz, affects μ whilst the variation of KI_0 with both pressure P and y_{O_2} is linear within the range investigated and measurement uncertainty. The model parameters are summarised in

TABLE 3.1: Prediction of the thickness of the glassy layer h as a function of plasma dose D using the frontal model. The dependence of the model parameters on pressure and oxygen content is reported for two different plasma frequencies.

$h = \frac{ln(D)}{\mu} - \frac{1}{\mu} ln(\frac{1}{KI_0} ln(\frac{1}{1-\phi_c}))$		
f	μ [nm $^{-1}$]	KI_0 [kJ^{-1}]
13.6 MHz	0.065 ± 0.002	0.0072y_{O_2}-0.0061P+0.01053
40 kHz	0.136±0.006	0.0072y_{O_2}-0.0061P+0.0147

TABLE 3.2: Prediction of the wrinkling wavelength as a function of plasma dose D. The parameters in the logarithmic expression vary with pressure and gas oxygen content as reported.

$\lambda = \frac{ln(D)}{a} + b$		
f	a [μm $^{-1}$]	b [μm]
13.6 MHz	0.51 ± 0.002	1.68y_{O_2}-2.01P-2.81
40 kHz	1.07±0.4	1.04y_{O_2}-1.255P-2.42

Tables 3.1-3.2 and provide a useful tool to design a wrinkled sinusoidal topography with prescribed characteristic dimensions, by plasma oxidation of PDMS.

ii) Apart from an expression of $h(t)$, one can also extract the spatiotemporal variation of the conversion ϕ. Using the Matlab model implemented by Matthew G. Hennessy [163], we plot in Figure 3.14 $\phi(z)$ at different times. The plot reveals the existence of three regimes, namely *induction*, *formation*, and *propagation*. The induction regime is characterised by $\phi < \phi_c$, which corresponds to low plasma doses that cannot overcome the energy barrier for the conversion of PDMS and the formation of the glassy film.

At greater values of ϕ, between ϕ_c and ϕ_s we lie in the formation regime, where the thickness of the glassy film slowly increases with time, as the film simultaneously densifies. Indeed at these conditions, corresponding to low exposure times or plasma doses, it has been previously found [92, 93] that both the skin modulus and thickness increase during O_2 plasma exposure. This stage is particularly important as the modulus mismatch between the skin and the substrate continuously increases, which in turn sets the critical strain ϵ_c required for wrinkling to take place, which decreases following equation 1.8 [47, 50]. This inevitably sets a minimum λ achievable at constant $\epsilon_{prestrain}$. As ϕ becomes greater than the saturation value ϕ_s (assumed to be equal to 1), meaning that the layer is fully-oxidised, we

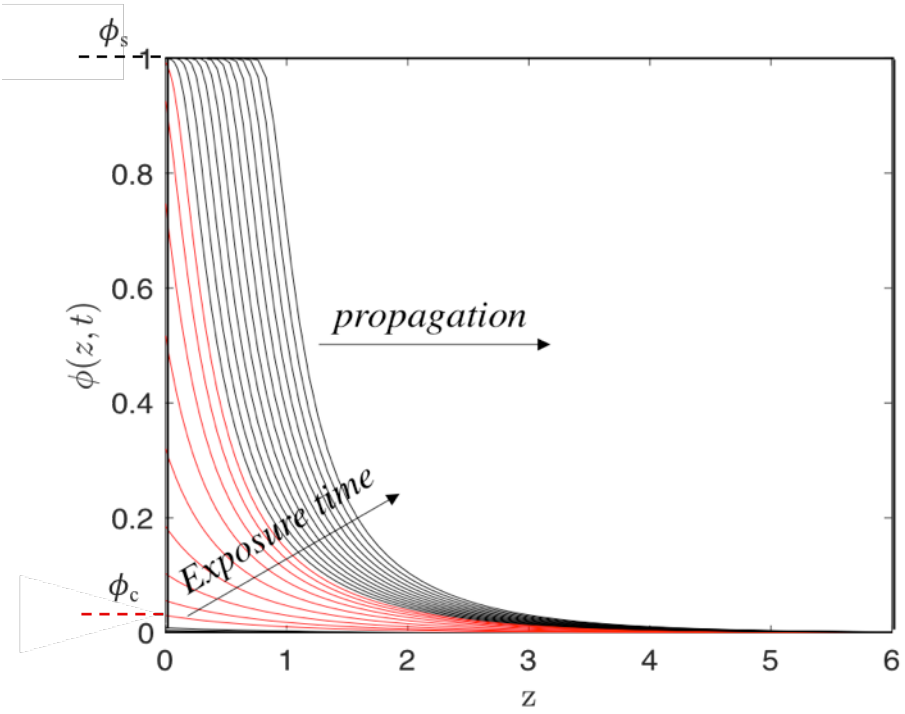

FIGURE 3.14: PDMS to glassy-layer conversion ϕ as a function of depth, z, for different times. ϕ_c and ϕ_s indicate the transition between the induction ($\phi < \phi_c$), formation ($\phi_c < \phi < \phi_s$, red curves) and propagation regimes (ϕ=ϕ_s).

enter the propagation regime corresponding to a steeper increase in the film thickness with time. The film largely propagates with a constant modulus and a sharp interfacial profile into the unconverted PDMS bulk layer. The plots of Figure 3.14 can be directly compared to measurements of real interfaces. Indeed, as discussed later in the thesis, the thickness of the glassy film varies between $\approx$ 2 and 20 nm at the plasma process conditions employed. Therefore by taking $z = h/h_{max}$ the plots effectively describe the observed surface conversion of PDMS upon plasma oxidation.

So far all the results presented were acquired using relatively high plasma doses $D > D_s$, where D_s is the dose required to achieve $\phi = \phi_s$, marking the transition between the formation and propagation regimes. In order to examine whether the predictions of the model picture apply to air plasma oxidation, we investigated very low air plasma doses, $D < D_s$, for two values of the gas pressure (Figure 3.15). Prestretched ($\epsilon_{prestrain} \approx 20\%$) PDMS samples exposed to MHz air plasma for doses lower than D_c did not show any pattern formation upon strain release. We

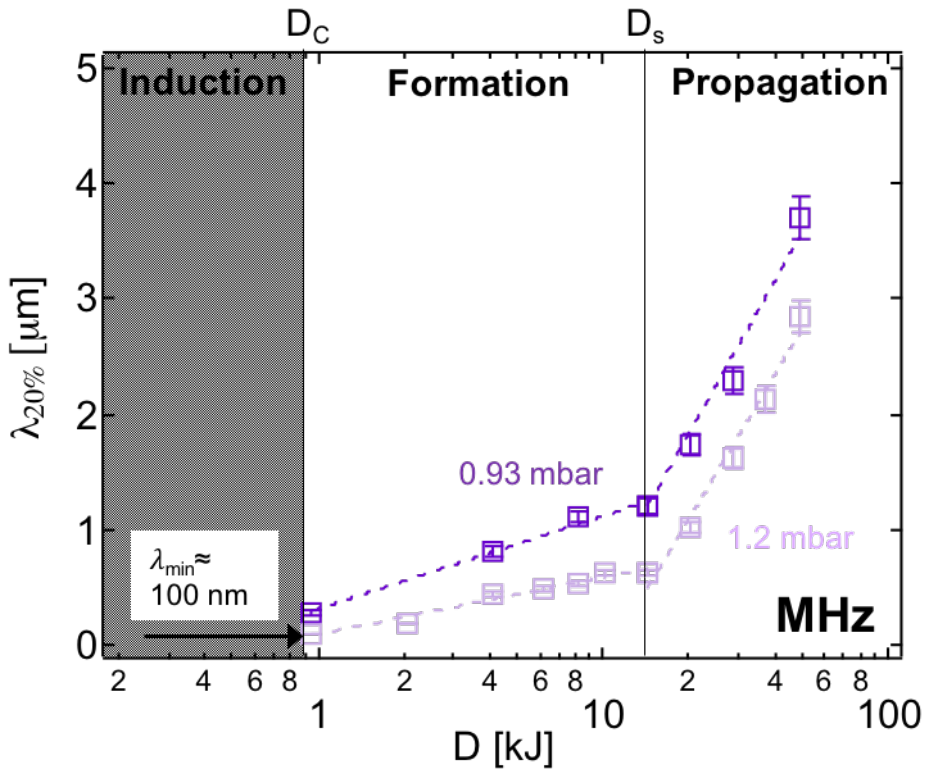

FIGURE 3.15: Wavelengths (λ) of wrinkled PDMS samples prestrained by $\epsilon_{prestrain} \approx 20\%$ and treated with MHz plasma, as a function of dose (D) for two values of air pressure $P = 1.2$ mbar and $P = 0.93$ mbar. The transition from film formation to propagation stages, defined by the saturation time/dose when the glassy skin reaches full conversion at the surface, is visible by a kink in the logarithmic propagation kinetics.

thought this could be due to the low modulus of the film during the initial stages of exposure, resulting in a high critical strain required for wrinkling. Experiments at $D < D_c$ were performed using $\epsilon_{prestrain}$ up to 60%, and still no wrinkling could be observed. We therefore hypothesise that, within this range, the film is yet to be formed, in line with the prediction of an *induction* regime. As $D \geq D_c$, wrinkles arise with an increasing wavelength as a function of plasma dose, decreasing with pressure at constant dose. The observed discontinuity in the logarithmic dependence of $\lambda(D)$ within this range marks the transition between the film *formation* and *propagation*, predicted by the model. The dose at which the 'kink' is observed is defined as the saturation dose D_s and corresponds to the extent of treatment required to reach the maximum conversion of the oxide layer. We can therefore conclude that, when varying the plasma dose within a wide range, wrinkling experiments on the resulting bilayers confirm the existence

of three regimes, reinforcing the adequacy of the frontal model in describing PDMS oxidation via air plasma.

3.3.1 Sub-140 nm patterning via wrinkling

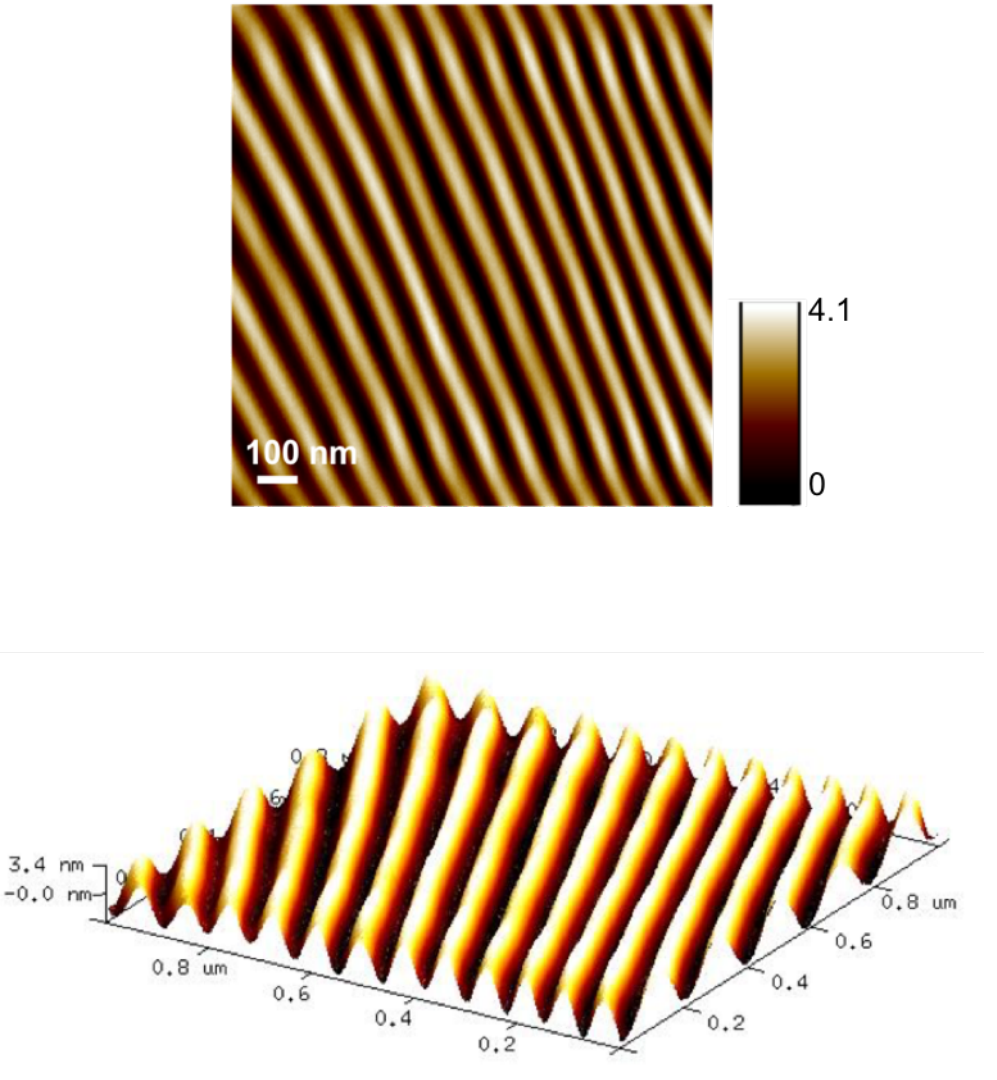

FIGURE 3.16: Illustrative AFM topography images (both 2-D and 3-D) of a 100 nm wavelength pattern achieved on PDMS by MHz air plasma oxidation with $\epsilon_{prestrain} \approx 20$ %, at $P = 1.2$ mbar, $p = 7.16$ W and $t = 90$ s.

The last experiments on wrinkling of plasma oxidised PDMS [93], prior to this work, showed that patterns with $\lambda_{min} \approx 140$ nm could be obtained, but with $\epsilon_{prestrain} \approx 200\%$, which brings the PDMS close to failure and compromises the reproducibility of the approach. The limit corresponded to PDMS oxidised with

a O_2 kHz plasma at $P = 0.6$ mbar and $D = D_c$. The control experiments we carried out established that, in order to reduce the pattern dimensions achievable via wrinkling of PDMS/PDMS oxidised bilayers one in turn has to lower the oxygen content in the gas whilst increasing its pressure, and lower the plasma dose. At these low doses, Figure 3.8 suggests that the MHz chamber is more effective at producing thinner/softer skins (thus smaller patterns), compared to the kHz plasma. As a result, the minimum λ is achieved when oxidising PDMS with air MHz plasma at $P = 1.2$ mbar and $D = D_c$ (corresponding to $D = 0.64$ kJ). We found that at these conditions we could achieve $\lambda_{min} \approx 100$ nm, employing a prestrain as small as 20% (Figure 3.17).

These findings suggest an attractive and facile route for sub-100 nm PDMS wrinkling with plasma exposure by further optimisation of plasma exposure and strain parameters.

Chapter 4

Towards sub-100 nm patterning via wrinkling of oxidised polydimethylsiloxane

So far we have demonstrated that wrinkling of plasma oxidised PDMS is an effective method to access patterns with λ as low as 100 nm [152]. We now seek to elucidate what sets this limit. The simple bilayer equations suggest that λ can be reduced by lowering film thickness or elastic modulus, or increasing the substrate elastic modulus. The relations valid in the high deformation regime give us another parameter, namely the strain $\epsilon_{prestrain}$, that we can tune to reduce the pattern wavelength. We firstly focused on h: we therefore carried out X-ray and neutron reflectivity experiments to elucidate the mechanism of glassy skin formation via plasma exposure. These experiments confirmed that a finite plasma dose is required for the film to form, and that dose corresponds to a minimum thickness and stiffness, due to the coupling of skin formation and front propagation. Having established this intrinsic limitation we then focused on the remaining two parameters. We evaluated the effect of increasing the strain, whose maximum is however set by material failure, as well as increasing the stiffness of PDMS by changing the elastomer:crosslinker ratio or the curing conditions. Implementing these measures only allowed for a small reduction of the minimum wavelength.

Inspired by this reduction we sought alternative ways to further stiffen substrates thus obtaining smaller pattern dimensions. We found that oxidising PDMS via ultra-violet ozonolysis prior to air plasma exposure resulted in the scope, allowing to reduce the surface topography down to $\lambda_{min} \approx 45$ nm. The results reported in this Chapter demonstrate the effectiveness of wrinkling for nano-scale patterning, with potential applications from optics and photonics from the visible to deep UV range, and have resulted in a publication [164].

4.1 An insight in the film formation and propagation: X-ray and neutron reflectivity studies

Our previous experiments on mechanical wrinkling of bilayers obtained via plasma oxidation of PDMS showed that, by employing a MHz chamber operated with air at relatively high pressure, patterns with $\lambda_{min} \approx 100$ nm could be observed upon strain release [152]. These minimum pattern dimensions correspond to a minimum plasma dose (D_c) or time (t_c) (assuming $p = 7.16$ W, corresponding to the lowest settable power). We thus could not see any pattern formation for $t < t_c$ within a range of $\epsilon_{prestrain}$ between 20 to 60% and this could be attributable to two phenomena: either (i) the glassy film was yet to be formed, or (ii) its conversion, thus elastic modulus, was still insufficient and the moduli contrast with the substrate resulted in a high critical strain required for wrinkling (leading to $\epsilon_{prestrain} < \epsilon_c$). If the first case (i) holds, this means that we cannot decrease h or $\bar{E}_f$ to lower λ_{min}. In an attempt to elucidate on the mechanism of glassy film formation on PDMS induced by plasma exposure, we carried out X-ray and neutron reflectivity experiments. As detailed in Chapter 2, these techniques allow for the determination of the density profile along the depth from the surface, thus providing with the information needed [85, 93, 143]. Samples in their relaxed state (prepared following the procedure detailed in Chapter 2) were oxidised with air MHz plasma at $P = 1$ mbar, and exposure times ranging from 30 s to 1200 s, and characterised with X-ray reflectivity first. The acquired reflectivity profiles are shown in Figure

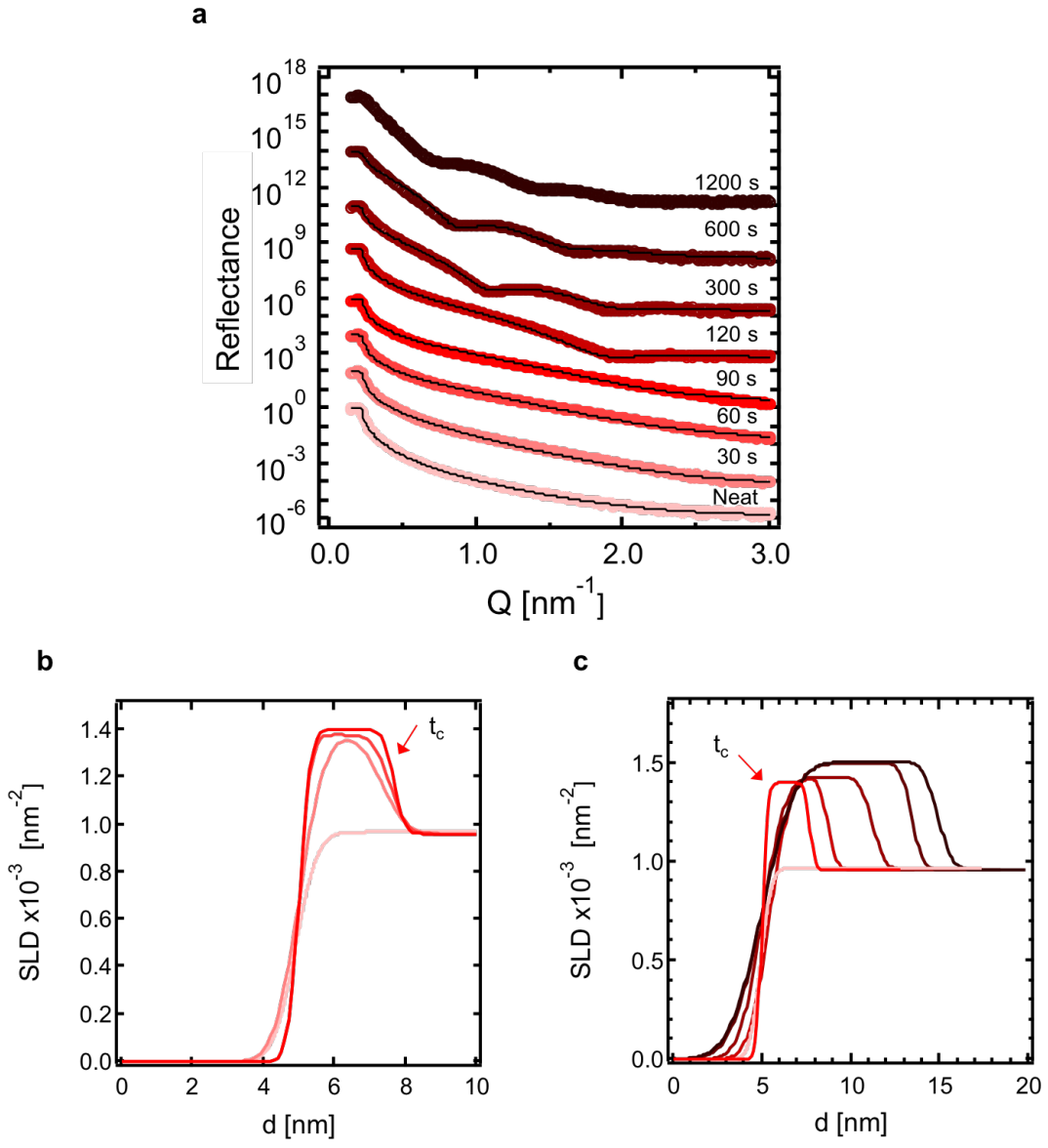

FIGURE 4.1: a) XRR of plasma-oxidised PDMS (MHz, air, $P = 1$ mbar, $p = 7.16$ W) for different time intervals, up to 20 min (scatter points). The black lines are the curve fittings obtained with Motofit and RasCal. Data are shifted vertically for clarity. b) SLD profiles derived from fitting reflectivity curves, for samples oxidised up to 90 s. Within the initial stages of plasma exposure the film slowly forms until it reaches a final value of the thickness and conversion at $t = t_c = 90$ s. c) SLD profiles derived from the XRR data fits, for exposure times from 90 s up to 1200 s. In b) and c) the colours of the different curves correspond to the exposure times, as defined in a).

4.1a and shifted vertically for clarity. A first inspection of the curves suggests that as the exposure time increases, 'Kiessig' [146] fringes appear, marking the formation of a layer with sufficient electron density contrast with PDMS; moreover the periodicity of these oscillations decreases as time increases, suggesting that the thickness of this glassy layer increases. All data acquired were then fitted using Motofit [148] and RasCal [149]. The fittings were performed with the assumption of a single oxide layer sandwiched between air (SLD=0) and a PDMS substrate ($\mathrm{SLD}_{PDMS,X-ray}$ = 9.61 × 10 $^{-4}$ nm^{-2}, h>> 1μm), with roughness at both interfaces. A value for the resolution $dQ/Q = 0.1$ was taken. The corresponding density profiles obtained from the analysis are plotted in Figures 4.1b-c. Specifically, Figure 4.1b shows the SLD as a function of the depth from the surface, for exposure times ranging between 0 s (neat PDMS) to 90 s. Within this range one can notice that the film starts forming: its thickness eventually reaches a finite value whilst the density approaches a first plateau. From $t = 90$ s onwards, the evolution of the SLD profiles is plotted in Figure 4.1c. The profiles suggest that during the first stages, both the thickness and density of the oxide layer increase: eventually, the SLD saturates and time only affects film thickness.

Having now a full picture of the mechanism of glassy film formation we can make several considerations. First of all, the X-ray reflectivity experiments further confirm the existence of the three regimes predicted by the frontal model [11, 160, 161] and corroborated by wrinkling data [152]. Indeed at selected process conditions (MHz, air, $p = 7.16$ W, $P = 1$ mbar) a minimum exposure time of 90 s is required to obtain a glassy layer with finite thickness and sufficient conversion ϕ_c (*induction*). Once the film is formed, it starts growing in thickness whilst simultaneously densifying (*formation*), until the maximum PDMS to SiO_x conversion (ϕ_s) is reached and only an increase in h is observed (*propagation*). What is interesting is that the time required for the film to be formed coincides with the exposure yielding the smallest λ in mechanical wrinkling experiments, i.e. t_c. This corroborates interpretation (i): unless a finite thickness ($h \simeq 3$ nm) and sufficient PDMS conversion are reached, the wrinkling instability cannot be triggered therefore alternatives to lowering h or $\bar{E}_f$ have to be sought to push the λ_{min} down to sub-100 nm.

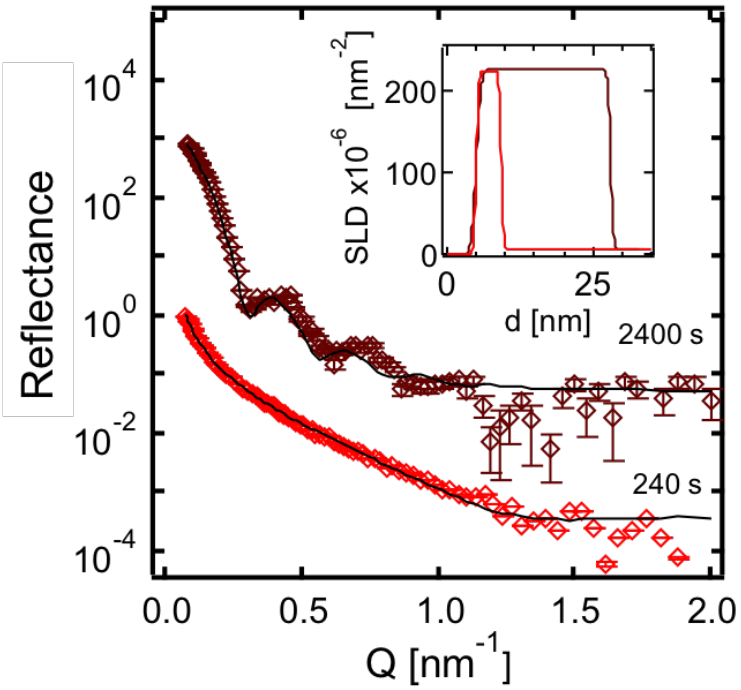

FIGURE 4.2: NR profiles of plasma oxidised (MHz, air, $p = 7.16$ W, $P = 1$ mbar) PDMS samples for exposure times $t = 240$ s and $t = 2400$ s. The black lines indicate the curves' fittings. The corresponding SLD profiles are shown in the inset.

The XRR measurements were further complemented by neutron reflectivity experiments on the same laminate profiles, whose contrast now arises from the neutron SLD, as shown in Figure 4.2. Data were fitted with the same model, but now with $\mathrm{SLD}_{PDMS,neutron} = 6\times\ 10^{\ -6}\ \mathrm{nm}^{-2}$. A value for the resolution $dQ/Q = 0.05$ was taken. The oxide layer thicknesses inferred from the fittings of both XRR and NR data were plotted as a function of plasma exposure time and compared with the values computed from the wrinkling experiments. These were obtained recalling the dependence between λ and h according to which

$$\lambda_{20\%} = \frac{\lambda_{0\%}}{1.21} = \frac{2\pi h}{1.21}\left(\frac{\bar{E}_f}{3\bar{E}_s}\right)^{1/3} \tag{4.1}$$

where the correction factor 1.21 is added to the classic bilayer equation to take into account the effect of $\epsilon_{prestrain} = 20\%$ on the wrinkling wavelength [156] . A value of $\bar{E}_s = 2.13$ MPa was taken for the elastic modulus of PDMS and values of $\bar{E}_f$ from ≈ 3 to ≈ 23 GPa, depending on the regime. The three independent

measurements are in good agreement and establish the kinetics of the glassy skin formation (Figure 4.3). As predicted by the front propagation model [11], a double logarithmic kinetics is found, where $h = a\ \ln(t) + b$ (a = 2.3988, b = -47.76532 in the 'formation regime'; a =15.247, b = -97.081 in the 'propagation regime').

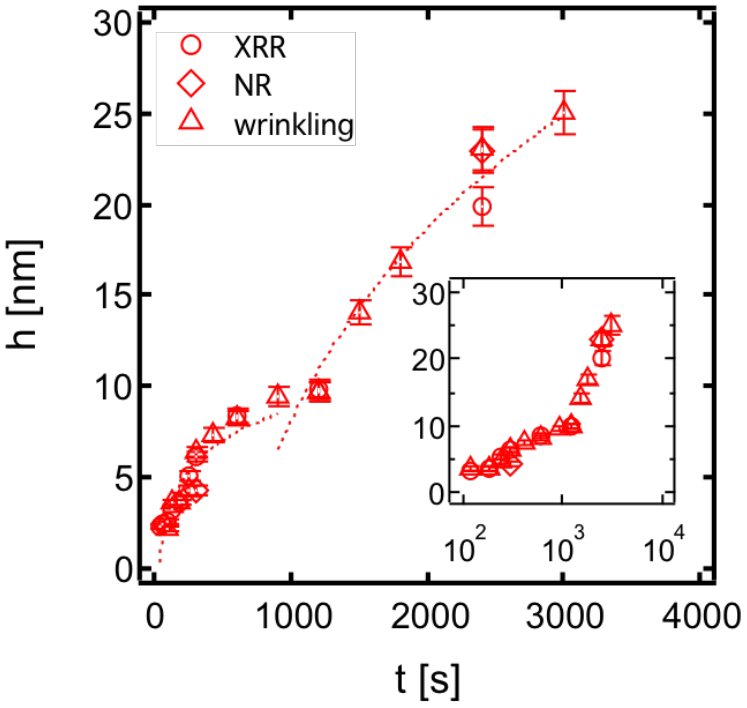

FIGURE 4.3: Oxide layer thickness as a function of plasma exposure time (MHz, air, P = 1 mbar, p = 7.16 W) obtained from XRR, NR and wrinkling data ($\epsilon_{prestrain} \approx 20\%$), according to equation 4.1. The inset shows the data in a lin-log scale.

4.2 PDMS modification and strain tuning : effect on wrinkling morphology

Having shown that h and $\bar{E}_f$ cannot be lowered further by reducing the plasma exposure time (or dose), we considered next increasing strain or $\bar{E}_s$ as a strategy to reduce λ_{min}. We started with a reference sample, obtained by oxidising prestretched ($\epsilon_{prestrain} \approx 20\%$) PDMS with exposure time t = 2400 s (MHz, air,

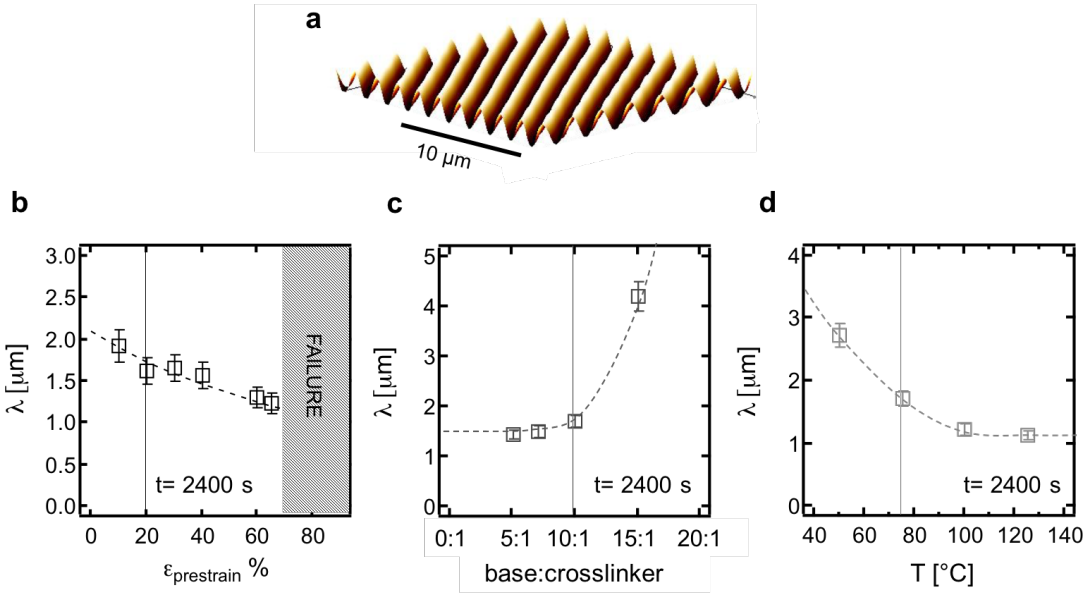

FIGURE 4.4: a) AFM scan of a wrinkling pattern obtained by uniaxial strain relaxation with $\epsilon_{prestrain} \approx 20\%$ of surface oxidised PDMS, using reference parameters: base:elastomer ratio 10:1, curing $T_{crosslinking} = 75$ °C, MHz air plasma, $t = 2400$ s, $P = 1$ mbar, and $p = 10.16$ W. b) Effect of varying $\epsilon_{prestrain}$, c) base:crosslinker ratio and d) curing temperature on surface λ, with respect to reference parameters. Line in b) is a fit to the bilayer model in high deformation [156] with fitting parameter $\lambda_{0\%} = 2.2 \pm 0.1$, whilst lines in c) and d) are guides to the eye.

$P = 1$ mbar, $p = 10.16$ W). Figure 4.4a shows an AFM image of the sample's morphology observed upon strain release.

We first evaluated the reduction in wavelength that can be achieved by tuning the strain applied to the PDMS/glassy film bilayers. As seen in previous experiments, increasing the prestrain leads to a decrease in pattern wavelength, according to the predictions of the bilayer model in the high deformation regime [156]. Figure 4.4b shows the effect of increasing $\epsilon_{prestrain}$ on λ, for the reference sample. An upper limit for the prestrain applied of approximately 65% was set: higher values can result in wrinkling modes other than sinusoidal and eventually material failure. As seen from the measurements, the λ reduction with respect to reference $\epsilon_{prestrain} = 20\%$ strain is limited to less than 15% decrease. In other terms, when we applied the maximum strain, impractical and resulting in significant surface cracking, we could only achieve a negligible reduction in pattern wavelength. We therefore concluded that increasing the prestrain is not an effective strategy for the purpose

of reducing λ_{min} and we opted to fix $\epsilon_{prestrain} = 20\%$ in the experiments.

We then moved to devise strategies aiming to increase $\bar{E}_s$. Stiffening the PDMS substrate can be trivially achieved by decreasing the base:crosslinker ratio, by varying curing temperature (or time) or by addition of fillers. The impact of changing these variables on the PDMS modulus increase has been studied in some detail [109, 129, 130] as well as the resulting effect on the wrinkles' dimensions [165]. In assessing how PDMS modification impacts the wrinkling morphology we will refer as *conventional* PDMS to indicate the curing conditions normally utilised in the experiments carried out to date (base:crosslinker = 10:1, $T_{crosslinking}$ = 75 ° C, $t_{crosslinking}$ = 1 hour). We then evaluated how the patterns changed when varying the base:crosslinker ratio of PDMS. PDMS slabs were thus prepared using the conventional approach (described in Chapter 2), where only the ratio between the amount of base and crosslinker was varied. We expect that higher quantities of crosslinker, thus lower ratios, lead to stiffer substrates. The slabs were then prestretched and oxidised at the same conditions as the reference sample. The wavelength of the surface patterns was then plotted as a function of the base:crosslinker ratio (Figure 4.4c). We found that λ decreases when increasing the amount of crosslinker relative to the elastomer, as expected as the elastic modulus of the substrate increases. However the reduction is limited since doubling the crosslinker content only reduces λ by $\approx 15\%$.

Therefore, the PDMS modification induced by varying the temperature employed for curing was assessed. Substrates were prepared using again the conventional procedure, but this time changing the curing temperature between 50 °C and 120 °C. Prestretched slabs were oxidised using the same process conditions as the reference sample and the wavelength of the arising wrinkles was measured (Figure 4.4d). An increase in the curing temperature led to a decrease in λ, as the PDMS becomes stiffer when cured at high temperatures. The maximum reduction in the pattern wavelength amounted to 30%.

The results confirm that PDMS modification is an effective strategy in lowering

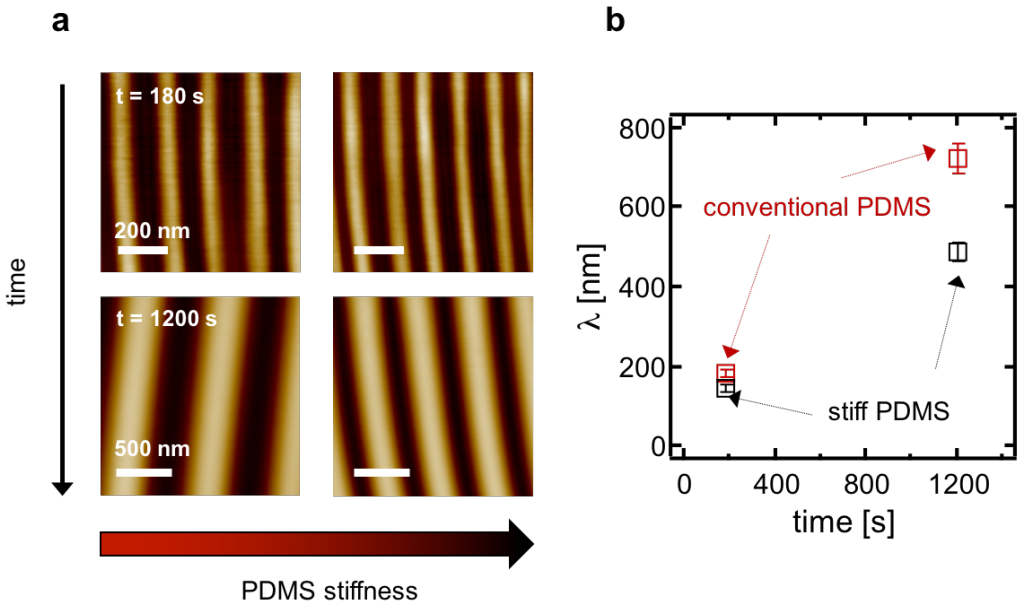

FIGURE 4.5: a) AFM images of wrinkling patterns obtained on PDMS slabs cured at different conditions (Conventional: $T_{crosslinking}$= 75° C, base:crosslinker = 10:1, Stiff: $T_{crosslinking}$ = 120 ° C, base:crosslinker = 5:1), prestretched by 20% and oxidised within a MHz plasma chamber for t = 180, 1200 s (P = 1.2 mbar, p = 7.16 W) and b) corresponding wavelength of the patterns.

pattern wavelength. Specifically, we found that 'optimal' substrates should be prepared with elastomer:crosslinker = 5:1 and $T_{crosslinking}$ = 120 ° C. However, it has to be noticed that the results presented referred to a reference sample treated with a relatively high plasma dose, and characterised by a wavelength λ in the micron range. Considering our aim of lowering the minimum wavelength achievable via wrinkling of plasma oxidised PDMS, we had to assess whether the same considerations apply at very low plasma doses. With this in mind, PDMS coupons were prepared using the optimal conditions identified before and oxidised at t = 180 s and t = 1200 s (MHz, air, P = 1 mbar, p = 7.16 W). Mechanical wrinkling was induced on the resulting bilayers. As seen from Figure 4.5, the observed decrease in wrinkle wavelength is a function of plasma exposure time (dose), going from approximately 32% at high doses to 19% at low doses. We therefore conclude that these incremental methods are not effective enough to access sub-100 nm patterning by plasma oxidation and mechanical-induced wrinkling of PDMS.

4.3 Substrate stiffening via ultra violet ozonolysis exposure

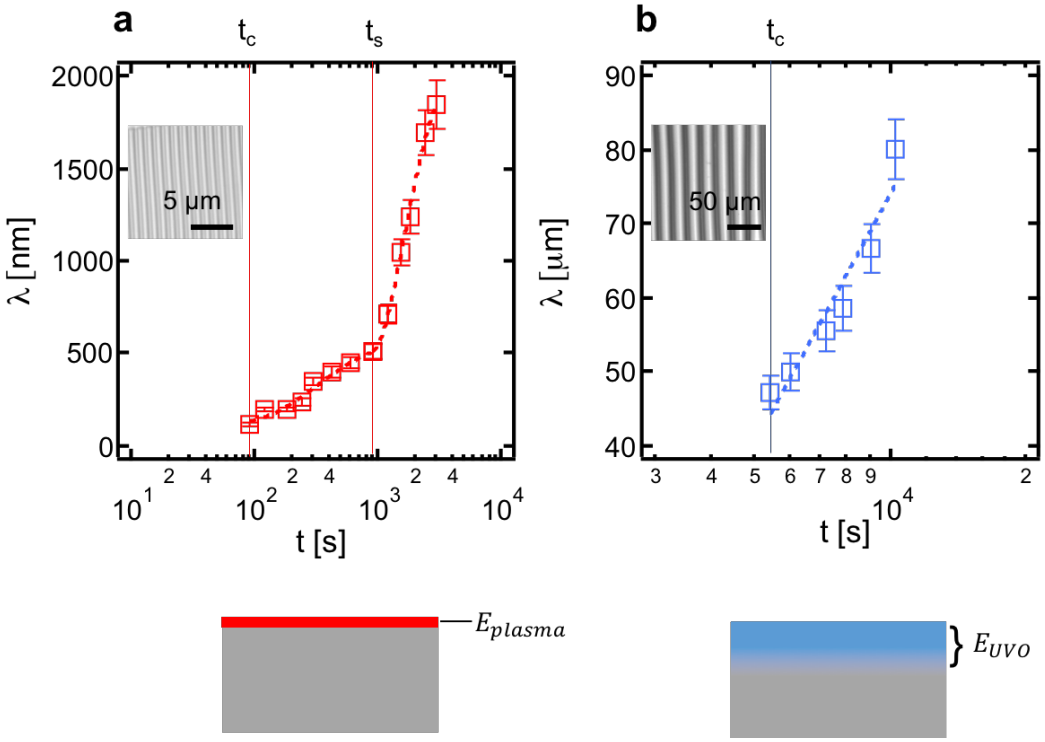

FIGURE 4.6: a) Sinusoidal wrinkle wavelengths for PDMS samples prestretched by $\epsilon_{prestrain} \approx 20\%$ and oxidised by means of MHz plasma, as a function of exposure time. The lines correspond to logarithmic fittings. The values t_c and t_s correspond to 90 and 900 s, respectively. Induction power and air pressure were kept constant respectively at $p = 7.16$ W and $P = 1$ mbar. b) Wavelength of wrinkles obtained by applying mechanical strain $\epsilon_{prestrain} \approx 20\%$ to bilayers resulting from UVO treatment of PDMS, as a function of exposure time. The line represents a logarithmic fitting. The value t_c corresponds to 90 min. Optical microscopy images of representative wrinkled samples are shown in the insets of both panels. The schematics below the panels show the impact of the two oxidative processes on bulk PDMS. Plasma oxidation results in the formation of a thinner, stiffer oxide layer compared to UVO, which leads to gradient layers [85]. The differences in layer elastic moduli and thicknesses justify the different pattern dimensions attainable with the two processes.

The results presented so far are somewhat discouraging: after eliminating the possibility of tuning the prestrain, the experiments demonstrated that increasing $\bar{E}_s$ (by tuning base:crosslinker ratio or curing temperature) is not effective for patterning in the deep UV range. Nevertheless, only the PDMS curing process was devised to obtain stiffer substrates, and this method yielded at best $\bar{E}_{s,max} \approx$

7 MPa at 'optimal' curing conditions. We therefore sought alternative strategies to achieve an increase of at least one order of magnitude compared to the plane strain modulus of PDMS ($\bar{E}_s \approx 2.13$ MPa).

We note that the oxidative processes themselves produce *'glassy'* layers, with significant moduli contrast with the bulk elastomeric substrate. So far, we have only focused on plasma oxidation. As stated in Chapter 1, however, ultra violet ozonolysis (UVO) can also be employed. When oxidising prestretched ($\epsilon_{prestrain} \approx 20\%$) PDMS via this method, much larger pattern dimensions compared to air plasma oxidation were observed [94–98]. Our results, as shown in Figure 4.6, agree with the expectations.

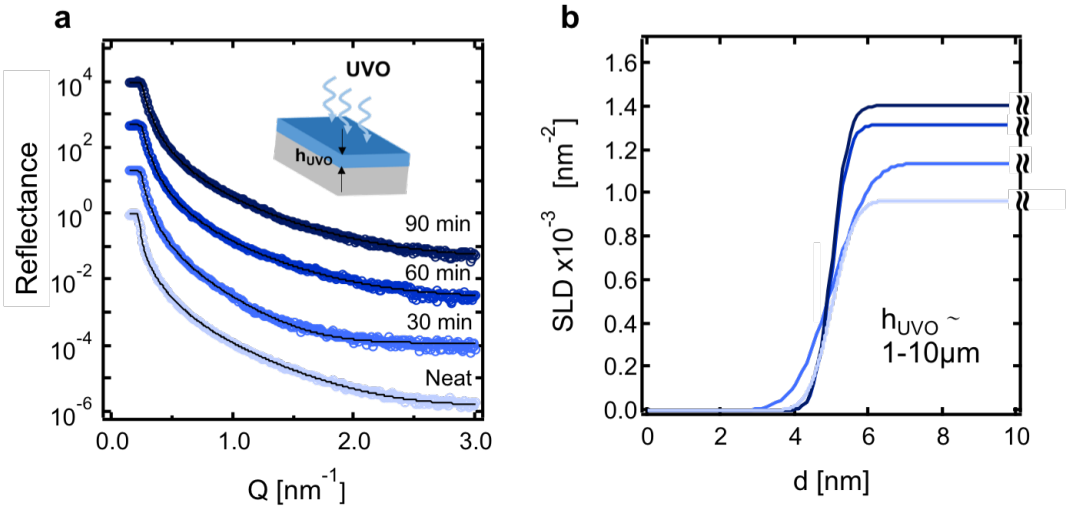

FIGURE 4.7: a) XRR measurements of PDMS specimens treated by UVO oxidation for up to 90 min exposure, along with a schematic of a PDMS sample oxidised via UVO, yielding a thick surface glassy skin with thickness h_{UVO}. The reflection profiles are normalised and shifted vertically for clarity. The black lines are the corresponding fits. b) XRR SLD profiles obtained from data fits in (a).

Plasma exposure yields bilayer wrinkling with λ ranging between ≈ 100 nm and ≈ 5 μm, compared to a much greater ≈ 20 to 100 μm for UVO (as inferred from the morphological characterisation, given the dependence between λ and h). Despite the scale difference, the front kinetics remain qualitatively similar, with $\lambda \propto ln(t)$ and a 'critical time' t_c required for plasma or UVO exposure, at constant $\epsilon_{prestrain}$,

below which the surface instability is not triggered. Recalling the dependence between λ and h the wrinkling experiments suggested that UVO exposure yields $h_{UVO} \gg h_{plasma}$ and/or $E_{UVO} \ll E_{plasma}$. Again X-ray reflectivity came in handy to resolve the PDMS densification upon UV-ozonolysis. Figure 4.7a plots the reflectivity curves acquired at different exposure times, ranging between 0 min (neat PDMS) to 90 min. As opposed to plasma exposure, the reflectivity profiles in this case did not show any Kiessig fringes, even at prolonged exposure. This is attributed to the fact that the thickness of the oxide layer resulting from UVO oxidation is above the spatial window of the technique (capable of determining thicknesses up to ≈ 1 μm, depending on interfacial width). Indeed when attempting to fit the data, we found that the assumption of a single layer model yielded the best results. We could therefore determine the roughness of the oxide layer at the interface with air, as well as the SLD profile in proximity to the surface (a value for the resolution $dQ/Q = 0.1$ was taken). As seen from Figure 4.7b, a densification of the oxide layer occurs upon exposure, which is however less pronounced compared to plasma oxidation. These results are in agreement with previous studies of PDMS vitrification via UVO oxidation [85, 97, 166].

Now we have to come back to the initial aim, which was to obtain stiffer substrates for bilayer wrinkling via air plasma oxidation, in order to access sub-100 nm patterns. These are of significant importance for the development of nanotechnologies that can precisely manipulate individual molecules [167]. So far we demonstrated, through the combination of wrinkling and reflectivity measurements, that UVO exposure results in the formation of thick ($\sim$ μm) layers, with lower mechanical properties compared to air plasma. We next evaluate whether the UVO oxide layer could act as a substrate for wrinkling of the plasma induced glassy layer. In principle, this should be possible, as the relative thickness and elastic moduli of the two layers satisfy the requirements to induce the wrinkling instability. A double oxidation approach could potentially result in the facile fabrication of laminate structures with optimal moduli contrast.

4.4 Double frontal UVO and air plasma oxidation approach

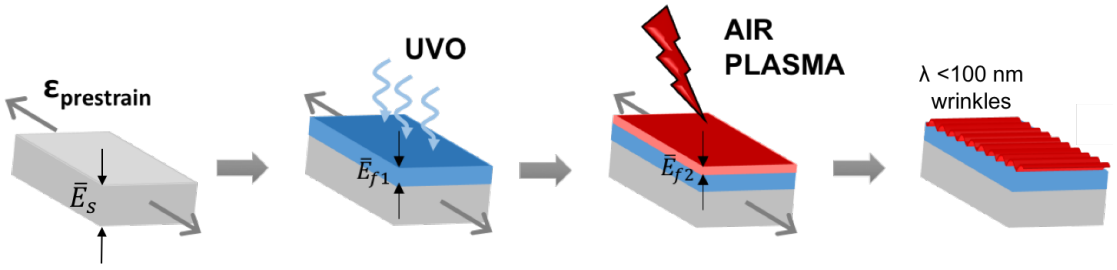

FIGURE 4.8: Formation of wrinkles on air plasma oxidised/UVO oxidised PDMS bilayers. A neat PDMS specimen is pre-strained uniaxially by $\epsilon_{prestrain}$, then exposed to UVO for t_{UVO}, leading to the formation of a layer with plane elastic modulus $\bar{E}_{f1}$, followed by air plasma exposure for t_{plasma} (MHz, $p = 7.16$ W, $P = 1$ mbar) resulting in the formation of a second layer with plane modulus $\bar{E}_{f2}$. Henceforth the strain is removed and sinusoidal wrinkling patterns with sub-100 nm λ are observed.

Based on the findings above, a double oxidation approach was implemented and evaluated, where prestretched PDMS is oxidised via UVO prior to air plasma treatment. We expect this double oxidation to yield two distinct layers, on top of the bulk PDMS. Therefore, two wrinkling mechanisms could be induced upon compression: one between the UVO oxide layer and the bulk PDMS and the second involving the plasma-oxidised film and the UVO oxide layer. The coupling of the two may eventually result in multiple frequency, hierarchical patterns. In order to obtain single frequency, sub-100 nm, sinusoidal wrinkles, the wrinkling mechanism between the UVO oxide layer and PDMS had to be suppressed

What we know from structural mechanics is that pattern formation on bilayers is conditional to the applied strain exceeding a critical strain ϵ_c, related to the moduli contrast between the substrate and the film [47, 50]. In the case of double oxidation, we could define two critical strains as follows:

- $\epsilon_{c,1}$ given by

$$\epsilon_{c,1} = \frac{1}{4}\left(\frac{3\bar{E}_s}{\bar{E}_{UVO}}\right)^{2/3} \tag{4.2}$$

referred to the wrinkling between the PDMS (substrate) and the UVO oxide layer (film);

- $\epsilon_{c,2}$ given by

$$\epsilon_{c,2} = \frac{1}{4}\left(\frac{3\bar{E}_{UVO}}{\bar{E}_{plasma}}\right)^{2/3} \tag{4.3}$$

determining the pattern formation due to wrinkling between the UVO oxide layer (substrate) and the plasma glassy layer (film).

Based on the definitions above, we conclude that the UVO oxide layer could be prevented from wrinkling by tuning the strain applied to the 'trilayer' such as $\epsilon_{c,2} < \epsilon_{prestrain} < \epsilon_{c,1}$. The wrinkling experiments on UVO oxidised PDMS presented in the previous sections established that, when employing a $\epsilon_{prestrain} \approx 20\%$, no wrinkling could be observed at exposure times lower than 90 minutes. Therefore, by choosing a treatment time of $t_{UVO} = 60$ min and $\epsilon_{prestrain} \approx 20\%$ we could not observe wrinkling of the UVO oxide layer, whilst still having a film with a finite thickness and conversion, as demonstrated by X-ray reflectivity measurements.

PDMS slabs were then prestretched by $\epsilon_{prestrain} \approx 20\%$, oxidised via UVO for $t_{UVO} < 90$ min, then treated with air plasma (MHz, $p = 7.16$ W, $P = 1$mbar) for variable times t_{plasma}. Upon strain removal only wrinkling of the top layer was observed, with sub-100 nm wavelength (Figure 4.8). X-ray reflectivity experiments on relaxed samples treated with the same procedure were also performed to verify the existence of two separate layers. The reflectivity curve of Figure 4.9a was acquired by oxidising PDMS with UVO for $t_{UVO} = 60$ minutes followed by air plasma for $t_{plasma} = 30$ min. Fitting was performed (with a resolution $dQ/Q = 0.1$) by assuming a single layer (plasma oxide film) sandwiched between air and the UVO oxide layer, acting as the bulk substrate. The data were successfully described by the model, and confirmed the assumption of the formation of two distinct layers with mismatched SLDs, thus mechanical properties, upon subsequent oxidation treatments (Figure 4.9b).

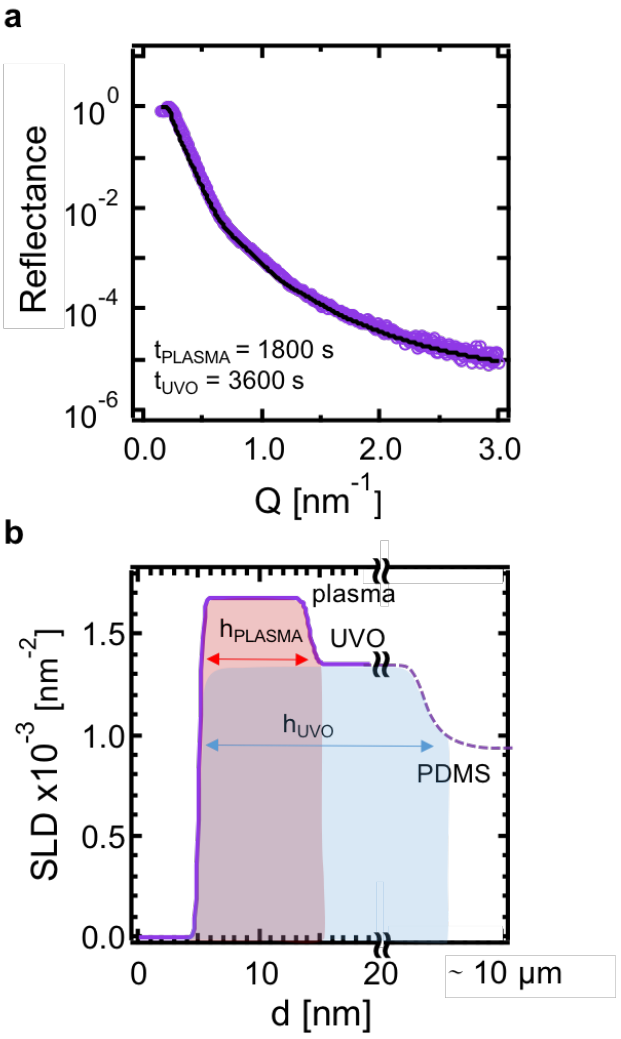

FIGURE 4.9: a) XRR measurements on PDMS specimens treated with subsequent UVO (t_{UVO} = 3600 s) and air plasma oxidation (t_{plasma} = 1800 s, P = 1 mbar, p = 7.16 W) according to the process in Figure 4.8. Normalised scattered intensity is plotted as a function of Q. Both experimental data (scatter) and the corresponding fittings using RasCal are presented. b) XRR scattering length density profile obtained from the reflectivity curves fittings. Two distinct layers could be identified, of thicknesses h_{UVO} and h_{plasma}, resulting from the subsequent oxidative processes.

Extensive wrinkling experiments were carried out following the procedure of Figure 4.8, at constant t_{UVO} = 30 and 60 min and variable t_{plasma}. The resulting surface morphology was characterised by means of AFM. Figure 4.10a shows the wavelength as a function of plasma exposure time for the two t_{UVO}, as well as the data previously acquired in case of simple plasma oxidation (t_{UVO} = 0). We find that the UVO pre-treatment does not impact the plasma oxidation mechanism, which can still be described with a frontal model, as indicated by the logarithmic

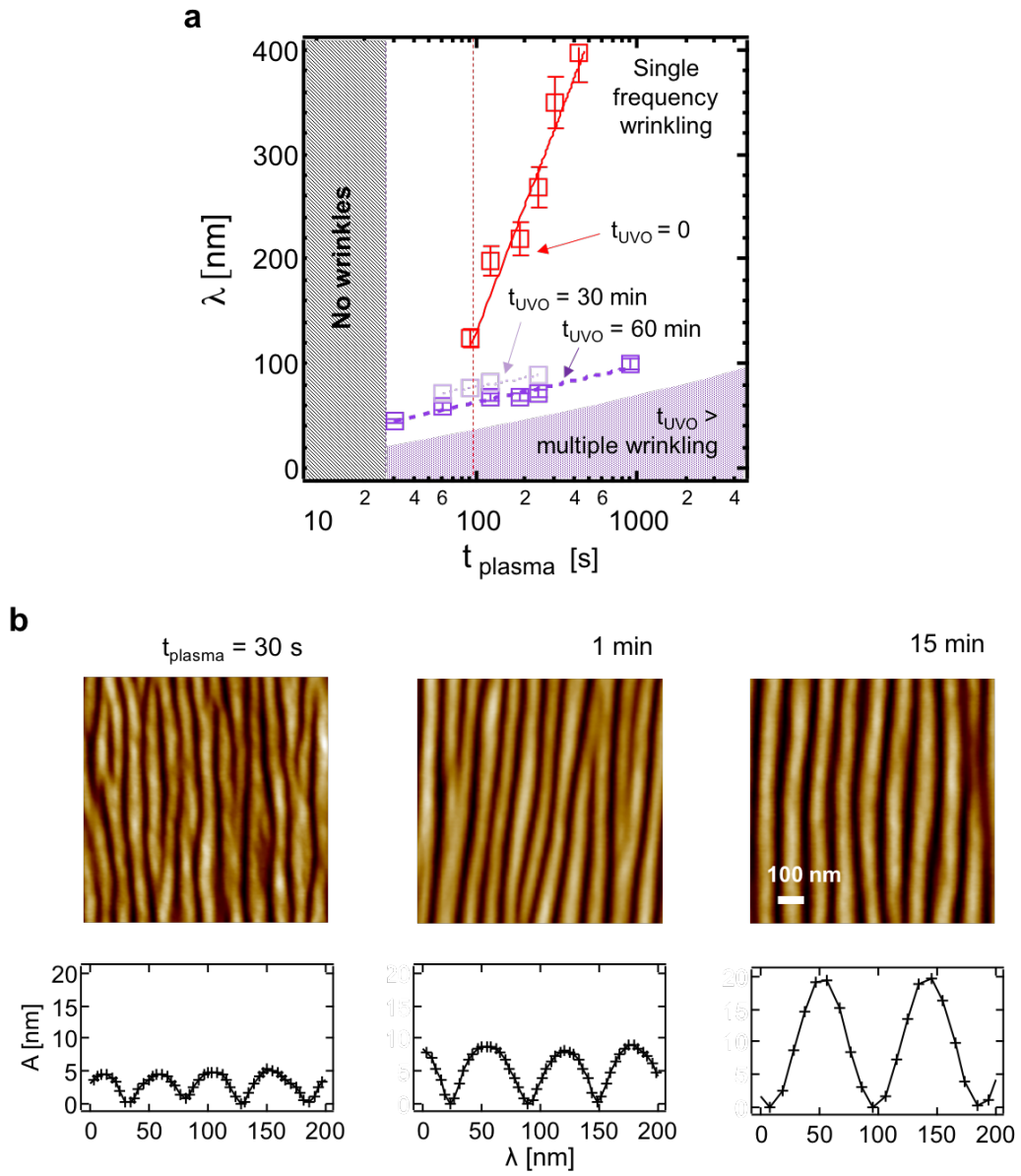

FIGURE 4.10: a) Wavelength of the wrinkles obtained using the procedure detailed in Figure 4.8, as a function of air plasma (p = 7.16 W, P = 1 mbar) treatment time, for species prestrained by $\epsilon_{prestrain}$ and pre-treated via UVO exposure for 0, 30 and 60 minutes. The lines correspond to logarithmic fittings according to equation $\lambda = a\ln(t) + b$. b) AFM tapping mode topographies of wrinkling patterns obtained by subsequent UVO (t_{UVO} = 60 min) and air plasma (P = 1 mbar, p = 7.16 W) exposure of a PDMS specimen, upon relaxation of uniaxial strain $\epsilon_{prestrain} \approx 20\%$.

trend observed for the wavelength. However, by comparing the results at different UVO treatment times, one can clearly notice that an increase in t_{UVO} results in a decrease of λ. This was expected, considering that the UVO oxide layer acts as the substrate for wrinkling of the plasma glassy film and it stiffens upon exposure

time, as indicated by the XRR experiments presented in the previous sections. The extent of UVO pretreatment also impacts the critical time required for wrinkling, which shifts from 90 s, in case of sole plasma exposure, to 60 s (for t_{UVO} = 30 min), eventually reaching 30 s when t_{UVO} = 60 min. This result is expected as the UVO treatment leads to a partial conversion of the PDMS surface: therefore a lower energy barrier has to be overcome in order to form the oxide layer via plasma oxidation. This leads to a decrease in the critical time t_c. Therefore the UVO pretreatment not only increased the substrate's elastic modulus, but also allowed for film formation via plasma oxidation to be reached at shorter times, leading to smaller h_{min} and $\bar{E}_{f,min}$ compared to the case when $t_{UVO} = 0$. The coupling of these effects yielded a significant reduction in the minimum pattern wavelenght attainable with PDMS oxidation. A λ_{min} = 45 nm was thus readily obtained with t_{UVO} = 60 min and t_{plasma} = 30 s, at modest $\epsilon_{prestrain}$=20% and without PDMS modifications. Representative AFM images of wrinkled surfaces produced by t_{UVO} = 60 min and various t_{plasma} are shown in Figure 4.10b.

Based on the results presented above, we can make three main considerations:

- The minimum wavelength reported was observed by employing a value of $\epsilon_{prestrain} \approx 20\%$. We have previously reported on the reduction of the wavelength that can be induced by an increase in the prestrain utilised. Therefore one could argue that even lower values of λ can be accessed just by stretching the laminate structures to higher extents. However, increasing $\epsilon_{prestrain}$ resulted in triggering the wrinkling mechanism between the UVO oxide layer and the PDMS, and is therefore not applicable.

- We found that λ_{min} = 45 nm can be achieved by double oxidation of 'conventional' PDMS. However, in the previous sections we discussed how modifying PDMS curing conditions can lead to a reduction in the pattern wavelength. Therefore, can we further lower λ_{min} by optimally-curing the PDMS substrates? Unfortunately, this was not possible due to the nature of the process. Modifying PDMS curing conditions would simply impact the wrinkling

instability occurring between the bulk PDMS and UVO layer, deliberately suppressed with the prestrain chosen.

- Finally, we have seen how both the substrate elastic modulus increases and the critical time required for wrinkling decreases when prolonging the UVO pretreatment of PDMS. However, the highest value of t_{UVO} employed was 60 min. Is it possible to increase t_{UVO} further thereby lowering λ_{min}? Disappointingly, the answer is 'no'. If indeed we look at the wrinkling experiments on UVO oxidised PDMS bilayers, we can see that pattern formation readily occurs at $\epsilon_{prestrain} \approx 20\%$ when t_{UVO} approaches 90 minutes.

Thus patterns with a minimum λ of 45 nm can be achieved via wrinkling of PDMS oxidised with subsequent UVO and air plasma exposure. The double oxidation method yields a reduction of 55% in pattern wavelength, well above the other solutions presented. We have therefore demonstrated that wrinkling is effective at patterning in the nano-scale, down to the deep UV-range.

Chapter 5

Wrinkling at the micron-scale: UVO oxidation of PDMS for single and double frequency patterns

As discussed in Chapter 1, the purpose of this work was to find a scalable method for soft matter patterning from the nano- to the macro-scale. So far, the focus has been on the nanoscale. We demonstrated that, by wrinkling of bilayers obtained via air plasma oxidation of PDMS, sinusoidal patterns with a minimum wavelength of 100 nm can be observed [152]. We then further lowered this limit to 45 nm, by employing a two-step process to oxidise PDMS, involving ultra-violet ozonolysis (UVO) followed by air plasma [164]. In assessing the double oxidation approach, we carried out a set of wrinkling experiments on laminate structures resulting from UVO oxidation of PDMS: the results showed that the induced wrinkles are characterised by wavelengths ranging between tens to hundreds of microns. In order to establish wrinkling of bilayers as a valid patterning method at the 'macro' scale, we start by systematically studying the vitrification of PDMS induced by UVO and its impact on surface wrinkling. We find that the process is effective at impressing single frequency, sinusoidal patterns within the μm range. Further, we demonstrate that, at selected conditions, double-frequency, hierarchical features arise. This Chapter summarises these findings, reported in [168].

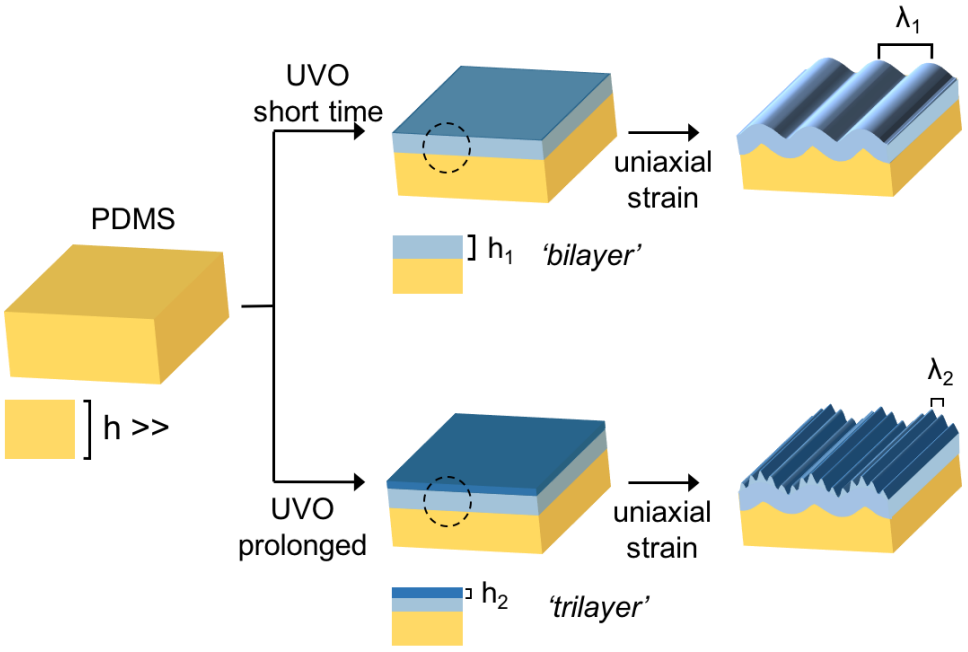

FIGURE 5.1: Schematic of the glassy skin formation for PDMS oxidised via UVO, and consequences on mechanical wrinkling. PDMS coupons are subject to short and prolonged UVO exposure. Low treatment times result in the formation of a single layer (light blue, thickness h_1) on top of the compliant substrate. By applying uniaxial strain to the bilayer, sinusoidal wrinkles with wavelength λ_1 arise. Prolonged UVO exposure contributes to a further conversion of the top surface, leading to the formation of a second layer (dark blue, thickness h_2); a second generation of sinusoidal wrinkles emerges (with wavelength λ_2), following the application of an uniaxial strain.

5.1 Frontal oxidation of PDMS using ultraviolet ozonolysis and consequences on surface wrinkling

We start by focusing on wrinkling of bi-(multi-)layers obtained via UVO oxidation of PDMS. Specifically, PDMS slabs were stretched uniaxially by $\epsilon_{prestrain}$, placed in the UVO chamber (at a distance $d_{lamp} = 1$ cm from the lamp) and treated for short ($t \approx 60$ min) and long ($t \approx 120$ min) times. Upon strain release, two different morphologies were observed, depicted in Figure 5.1. At low treatment times single frequency sinusoidal patterns with wavelength λ_1 arose; when increasing the UVO exposure, a second generation of sinusoidal features with λ_2 emerged. This

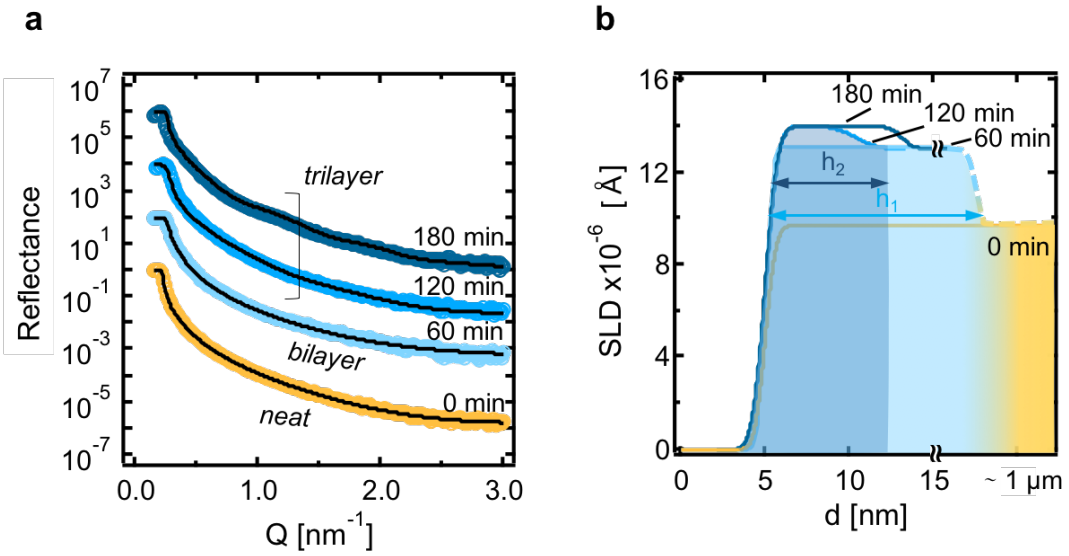

FIGURE 5.2: a) X-ray reflectivity of UVO-oxidised PDMS ($d_{lamp} \approx 1$ cm) for time intervals up to 180 min, and corresponding fittings (black lines). For clarity purposes, curves have been shifted vertically. b) SLD profiles obtained from fits in (a).

behaviour can be justified if we consider that, during the first stages, the oxidation treatment leads to the formation of a thick (h_1) layer on top of the compliant substrate (indicated with light blue in Figure 5.1); as the treatment proceeds, the surface of this thick layer further oxidises leading to a stiffer top film (thickness h_2, dark blue in Figure 5.1).

To corroborate this hypothesis X-ray reflectivity experiments were carried out on relaxed samples, oxidised for various times (from 0 to 180 min). The reflectivity profiles acquired are shown in Figure 5.2a. Data relative to samples exposed for times up to 60 min could only be modelled using a single layer at a air interface (SLD=0), as at these conditions the thickness of the glassy skin is above the resolution of the technique. By comparing the resulting scattering length density profiles at 0 and 60 min (Figure 5.2b), we can notice that the thick oxide layer has a relatively low conversion. Reflectivity curves for samples subject to prolonged UVO exposure ($t \geq 120$ min) could be fitted using a model comprising a film sandwiched between air and the thick oxide layer resulting from the first stages of the oxidation. A value of the resolution $dQ/Q = 0.1$ was taken for all the fittings. The SLD profiles show a further, top layer, with thickness h_2 of a few nm.

XRR coupled with wrinkling experiments demonstrated that oxidation of PDMS via UVO proceeds via the propagation of two fronts, the second arising when exceeding a critical exposure time (at constant distance d_{lamp} from the lamp), thus concentration of radical species.

5.1.1 Effect of UVO duration and sample position

Having identified the range of exposure times where two layers are present, we carried out a series of control experiments driven by the wish of being able to control and predict the hierarchical morphologies. We first elucidated the effect of exposure time on the two generations of wrinkles. PDMS slabs were stretched by $\epsilon_{prestrain} \approx 20\%$ and UVO-treated for 120, 180, 240 and 300 min at constant distance $d_{lamp} \approx 1$ cm from the lamp. Figure 5.3a compiles both λ_1 and λ_2 as a function of exposure time. Due to the different scale of the two generations of wrinkles, AFM was employed to characterise λ_2 whilst λ_1 was inferred by surface profilometry. Figure 5.3b shows in turn surface profilometry and AFM scans of the samples depicting the two morphologies making up the hierarchy. Based on the data we can first deduce that the thicknesses of both layers, therefore λ_1 and λ_2, increase over time, suggesting we cannot decouple and tune independently the two generations of wrinkles (as shown in the schematic in Figure 5.3a); furthermore we can conclude that both layers grow with a frontal mechanism, as the logarithmic trend suggests.

We next evaluated the effect of the sample distance from the lamp. As reported in Chapter 2, the distance affects the intensity of the light emanated from the source: specifically the intensity was found to decrease at increasing distances from the lamp. The purpose of the UV-light is to break down the molecules and to create the radical species responsible for the oxidation reaction: a lower intensity thus leads to a lower number of reactive species and a 'weaker' treatment. The experiments were performed applying a constant prestrain of $\approx 20\%$ to the PDMS coupons prior to UVO oxidation for a constant time of 120 minutes. Figure 5.4 shows images acquired with both surface profilometry and atomic force microscopy,

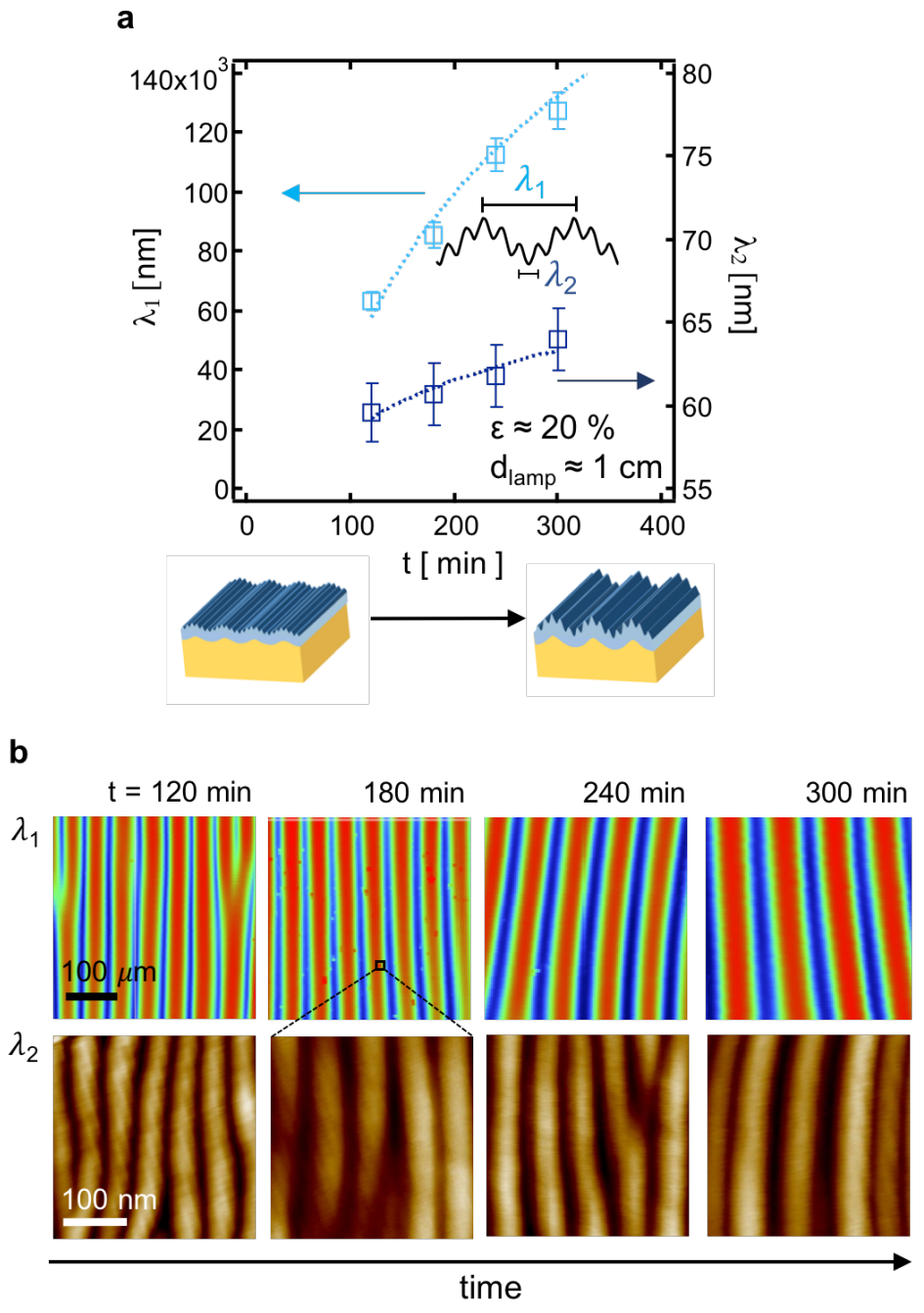

FIGURE 5.3: a) Effect of UVO exposure time on the wavelengths λ_1 and λ_2 of the two generations of wrinkles. Data were acquired by using a constant value of $\epsilon_{prestrain} \approx 20\%$, and placing the samples at a distance $d_{lamp} \approx 1$ cm from the lamp. Lines corresponds to logarithmic fits according to equation $\lambda = a\ln(t)+b$. b) Surface profilometry and AFM scans showing the two morphologies constituting the hierarchical pattern.

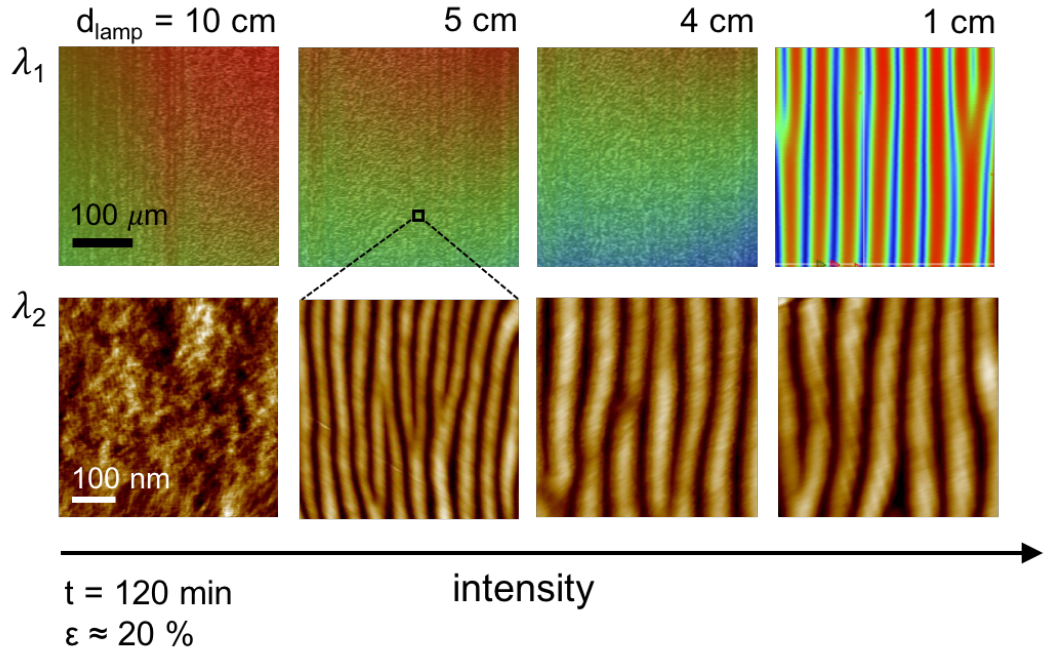

FIGURE 5.4: Surface profilometry and AFM scans of samples obtained by UVO-treating for 120 min PDMS samples prestretched by $\epsilon_{prestrain} \approx 20\%$, placed at different distances from the UV lamp.

to obtain qualitative information about the two generations of wrinkles on the samples in their relaxed state. The experimental observations suggest that, at constant strain, the $'small'$ wrinkles arise already when $d_{lamp} = 5$ cm, where the $'large'$ ones are absent. The fact that a 'weaker' treatment is sufficient to induce wrinkling between the top and intermediate layer suggests that these two have a higher modulus contrast compared to the intermediate layer and the bulk PDMS. Moreover one can notice that both λ_1 and λ_2 increase when decreasing the distance from the lamp.

The experiments on air plasma oxidation of PDMS demonstrated that a single master curve can be obtained by rescaling wrinkling data acquired at different power settings and exposure times in terms of a variable defined as dose D ($\equiv$ power $\times$ time) [152]. Having established the dependence between the light intensity I and the distance d_{lamp} within the UVO chamber, we evaluated various rescaling variables involving I. Similarly to air plasma oxidation, we found that all the wrinkling data acquired at different intensities I [$W\ m^{-2}$] and exposure times t [s] collapsed when plotted as a function of the equivalent dose $D_{equivalent}$, defined

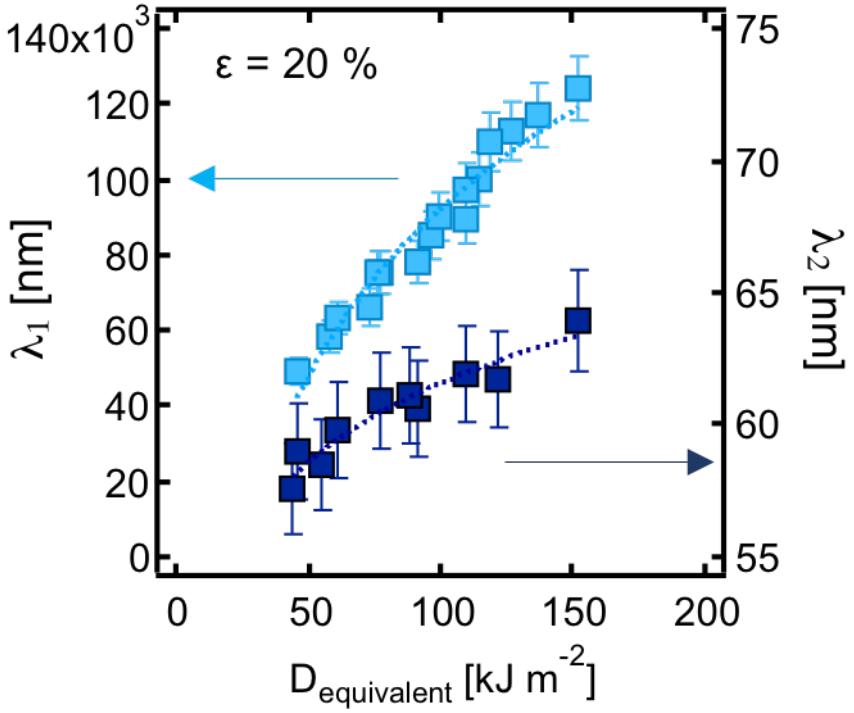

FIGURE 5.5: Wrinkling wavelengths (λ_1 and λ_2) of PDMS samples strained by $\epsilon_{prestrain} \approx 20\%$ and oxidised by UVO, as a function of the equivalent dose defined as $D_{equivalent} \equiv I \times t$. Lines are logarithmic fits according to equation $\lambda = a \ln(D_{equivalent}) + b$

as $D_{equivalent} \equiv I \times t$ (Figure 5.5). This correlation allows the generalisation of the results obtained and is useful in designing hierarchical morphologies via UVO oxidation of PDMS.

5.1.2 Effect of prestrain

The top layer requires a higher equivalent dose (compared to the intermediate, thick layer) to be observed (as demonstrated by both XRR and mechanical wrinkling measurements): however, within the 'trilayer' regime, wrinkling experiments at constant prestrain demonstrated that this top layer wrinkles at a lower $D_{equivalent}$. This suggests that, provided both layers are present, the critical strain needed for patterns with wavelength λ_2 to arise is lower that the one inducing wrinkles with wavelength λ_1. This hypothesis can be validated by performing wrinkling experiments at constant equivalent dose and variable prestrains.

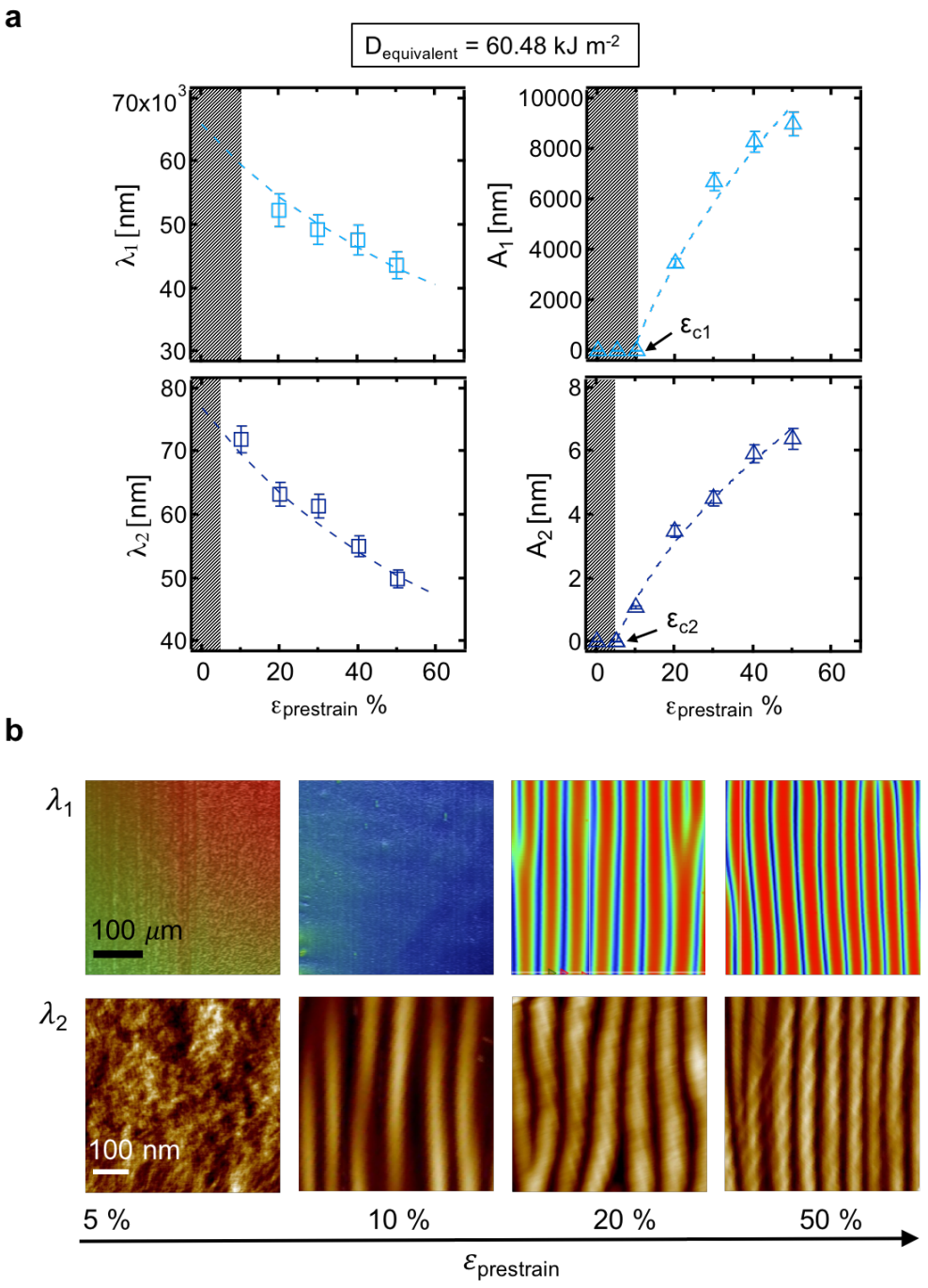

FIGURE 5.6: Wavelength and amplitude of the two generations of sinusoidal wrinkles for PDMS samples oxidised via UVO at constant equivalent dose $D_{equivalent} \approx 60.48$ [kJ m^{-2}], prestretched by $\epsilon_{prestrain}$ ranging between 5% and 50%. Lines are fit to the modified bilayer model in the high deformation regime [156] for the wavelength and the bilayer model for the amplitude [43, 46, 47]. b) Surface topography of the samples as acquired through optical profilometry and AFM.

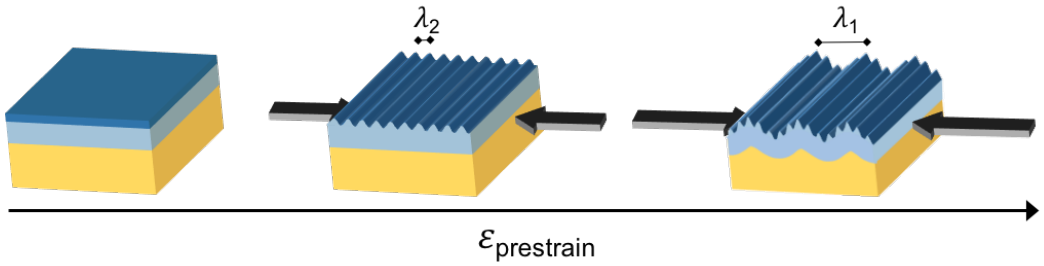

FIGURE 5.7: Schematic of the effect of strain on wrinkling of trilayers obtained via prolonged UVO exposure of PDMS. When increasing the strain applied, the top layer first buckles, resulting in single frequency, sinusoidal patterns with nm-scale feautures. Wrinkling of the intermediate layer also occurs when further increasing the strain, leading to hierarchical pattern formation.

PDMS slabs were prestretched by various $\epsilon_{prestrain}$ and oxidised via UVO at constant $D_{equivalent} = 60.48$ kJ m^{-2}. The effect of increasing $\epsilon_{prestrain}$ on the wavelength and amplitude of both generations of patterns is shown in Figure 5.6. We found that the trends for both λ_1 and λ_2 are well described by the bilayer model in the high deformation regime [156] (as reported previously in case of plasma oxidation)[1], whilst A_1 and A_2 data can be fitted using the simple bilayer model [43, 46, 47] [2]. The sample topography at the two different scales is presented in Figure 5.6b.

These experiments confirm that, at constant $D_{equivalent}$, the critical strain for wrinkling between the top and intermediate layer ϵ_{c2} is lower than ϵ_{c1}, describing the mechanism between the intermediate layer and the bulk PDMS where the two are given by [47, 50]

$$\epsilon_{c,1} = \frac{1}{4}\left(\frac{3\bar{E}_s}{\bar{E}_{UVO,1}}\right)^{\frac{2}{3}} \tag{5.1}$$

$$\epsilon_{c,2} = \frac{1}{4}\left(\frac{3\bar{E}_{UVO,1}}{\bar{E}_{UVO,2}}\right)^{\frac{2}{3}} \tag{5.2}$$

By appropriately varying the prestrain, we were then able to suppress one generation of these hierarchical patterns, otherwise strictly linked to each other. Figure

[1] $\lambda \propto \frac{1}{(1+\epsilon)[1+(\epsilon+\epsilon^2)]^{1/3}}$
[2] $A \propto \epsilon^{1/2}$

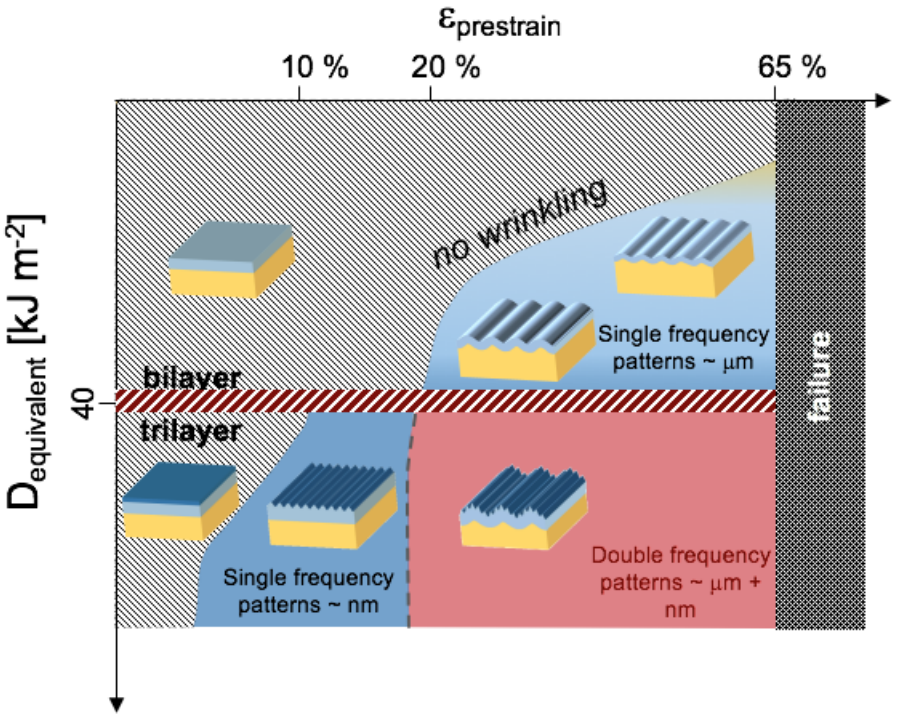

FIGURE 5.8: Map of the different morphologies attainable by UVO oxidation of PDMS, as a function of $D_{equivalent}$ and $\epsilon_{prestrain}$.

5.7 is intended to highlight the effect of the prestrain in the 'trilayer' regime.

5.2 Conclusions

Based on the results reported above, important conclusions can be drawn. When PDMS is oxidized by means of ultra violet ozonolysis, a single, 'thick' layer forms initially: if sufficient prestrain is applied, the bilayer wrinkles, giving rise to single frequency sinusoidal patterns with characteristic dimensions in the micron range. The critical strain needed for pattern formation decreases as a function of UVO dose, considering that the top layer densifies, as demonstrated by XRR experiments. By further increasing the plasma dose, we enter in the 'trilayer' regime, meaning that a second oxide film forms on top of the bilayer consisting of the thick layer and the bulk PDMS (as corroborated by XRR experiments). When gradually applying strain to this laminate structure, we demonstrated that the wrinkling

mechanism between the top and intermediate layers is triggered first, giving rise to single frequency, sinusoidal patterns with $\lambda_{min} \approx 55$ nm. Higher values of $\epsilon_{prestrain}$ led to wrinkling of the intermediate layer as well, resulting in double frequency sinusoidal patterns: these comprise sinusoidal patterns with $\lambda \sim \mu$m with a second generation with wavelengths of tens of nm superposed. By prolonging further the treatment time, both fronts propagate leading to an increase in both λ_1 and λ_2 which are thus coupled. Therefore we demonstrated that, by tuning the dose and the prestrain, we can obtain a variety of patterns, with a single step process: from nano to micron scale single frequency patterns to hierarchical wrinkles. Figure 5.8 summarises schematically all these findings.

Chapter 6

From single to double frequency sinusoidal patterns via wrinkling

The experiments on prestretched, PDMS samples treated with UVO, identified the conditions of dose and strain leading to hierarchical patterns, characterized by λ_1 and λ_2. However, we found that the two generations of patterns are strictly linked, with both increasing with dose and decreasing with $\epsilon_{prestrain}$.

Surfaces with hierarchical patterns have drawn a significant interest due to their unique wetting and superhydrophobic properties [118–123]. We thus seek to be able to fabricate surfaces with these characteristic morphologies, where we can independently tune the dimensions of the two generations of wrinkles constituting the hierarchy. Moreover, we aim to generalise the findings and identify which sequence of thicknesses/elastic moduli in the laminate structures subject to strain gives rise to double frequency patterns. Finally, we intend to model this wrinkling mechanism, thus relating λ_1 and λ_2 to the mechanical and geometrical properties of the multilayer. By doing this, we establish multi-layer wrinkling as a method for nested pattern formation. This Chapter discusses the broad role of trilayer wrinkling, summarising the results presented in [168].

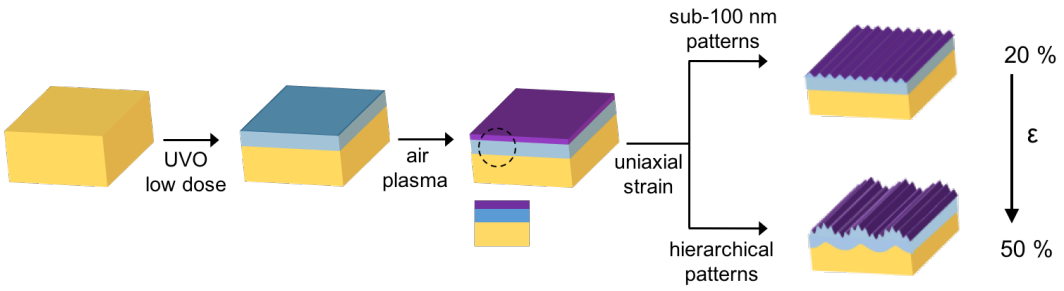

FIGURE 6.1: Formation of wrinkles using a 'two step' procedure. A PDMS slab is first oxidised with UVO at low equivalent dose (corresponding to t_{UVO} = 60 min, d_{lamp} = 9 cm), leading to a single layer of thickness h_1 and modulus $\bar{E}_{f1}$(shown in light blue). Subsequent air plasma exposure (MHz, p = 7.16 W, P = 1 mbar) on these bilayers results in the densification of the top surface, leading to the formation of a top film (thickness h_2, elastic modulus $\bar{E}_{f2}$). When uniaxial strain is applied to these tri-layer laminates two possible scenarios are observed. At low strain ($\approx$ 20 %) only the top layer wrinkles, giving rise to single frequency sinusoidal patterns with nm scale features; increasing the strain results in wrinkling of the intermediate, UVO oxide layer, leading to morphologies characterised by double frequency sinusoids.

6.1 Mechanical wrinkling of designed trilayers and resulting hierarchical patterns

We have demonstrated that, under specific experimental conditions, a simple exposure to UVO yields the formation of a bi-layer structure on a polydimethylsiloxane substrate, where hierachical wrinkling, with features ranging from tens of μm to tens of nm, can be mechanically induced. However, this $'single-step'$ method has an intrinsic limitation associated to the impossibility of controlling the thickness of the two layers, thus independently tuning the characteristic dimensions of the two generations of wrinkles. A viable solution may be found by moving from a single to a double step process, where each step contributes to the formation of one layer.

6.1.1 Double oxidation of PDMS for double frequency sinusoidal patterns

As reported in Chapter 5, we have been able to obtain sinusoidal wrinkles with $\approx$ 45 nm wavelengths, by fabricating laminate structures via subsequent UVO and air plasma exposure [164]. By appropriately selecting the UVO treatment time, we can obtain a single layer whose surface can be further converted by means of air plasma exposure, resulting in the formation of a second film. Using low prestrain values we could only allow wrinkling of the top layer, leading to single frequency, sinusoidal features with characteristic dimensions in the deep UV range. By increasing the prestrain, we can potentially trigger the instability between the intermediate UVO oxide layer and the bulk PDMS, thus obtaining a hierarchical pattern. The process is shown schematically in Figure 6.1. By employing this approach, we could reduce the limitations of wrinkling as a way to obtain hierarchical patterns: indeed, by keeping constant the UVO treatment time or equivalent dose (thus thickness of the corresponding layer and λ_1), we can independently tune λ_2 by varying the extent of plasma exposure (where longer exposure times correspond to thicker oxide layers).

Control experiments were thus performed on PDMS slabs, prestretched by $\epsilon_{prestrain} \approx$ 50 % and treated with UVO ($D_{equivalent,UVO} = 30.24$ kJ m^{-2}, $t_{UVO} = 60$ min) prior to plasma exposure for variable times (t_{plasma} ranging between 1 to 120 min). The UVO dose was chosen within the 'bilayer' regime ($D_{equivalent,UVO} < 40$ kJ m^{-2}, as reported in Chapter 5), to ensure the formation of a single oxide layer on top of the bulk PDMS. Experimental results are plotted in Figure 6.2. We first notice that the $\lambda_{2,plasma}$ increases logarithmically with the plasma exposure time, according to two different regimes (namely *'film formation'* and *'film propagation'*), previously observed in case of single plasma oxidation. On the other hand, $\lambda_{1,UVO}$ does not seem to be affected by the second exposure, remaining only dependent on the UVO treatment time, as shown in the inset. The different behaviour of the two wavelengths can also be visualised through the schematic.

AFM scans for samples at variable plasma exposure times are presented in Figure

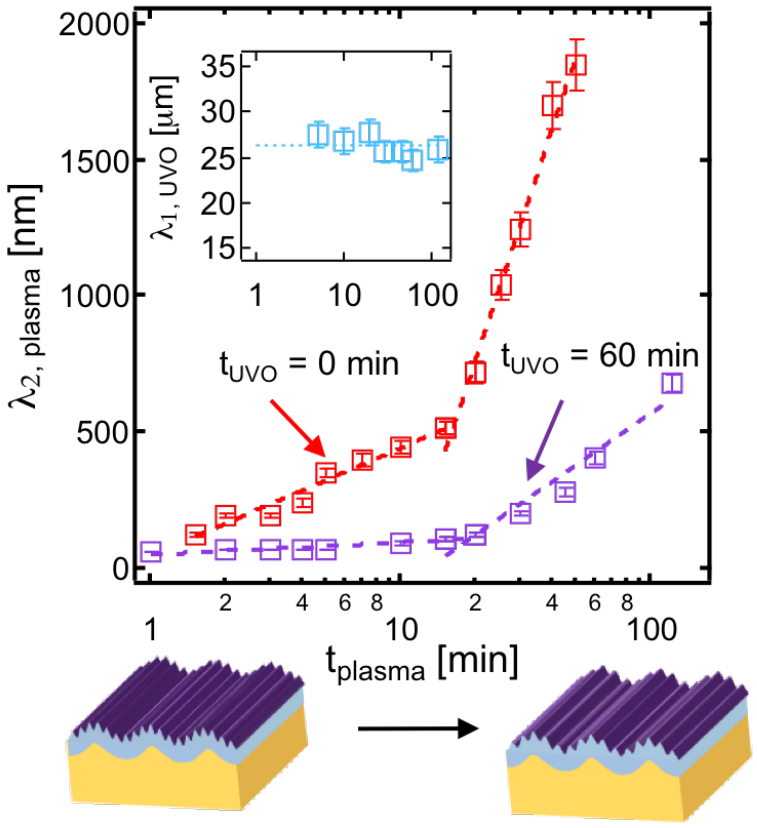

FIGURE 6.2: Wrinkling wavelength $\lambda_{2,plasma}$ as a function of air plasma (MHz, $P = 1$ mbar, $p = 7.16$ W) exposure time, for prestretched PDMS samples by $\epsilon_{prestrain} \approx 50$ %, pretreated with UVO for $t_{UVO} = 60$ min, corresponding to $D_{equivalent,UVO} = 30.24$ kJ m^{-2}. The graph also reports $\lambda_{2,plasma}$ as a function of t_{plasma} in absence of UVO pretreatment. The inset shows the wrinkling wavelength $\lambda_{1,UVO}$ as a function of t_{plasma}, at constant $t_{UVO} = 60$ min. The schematic highlights that, by varying t_{plasma} at constant t_{UVO}, one can succeed in tuning only one generation of patterns ($\lambda_{2,plasma}$).

6.3: when $\lambda_{2,plasma}$ lies in the micron range, we are able to capture the two generations of wrinkles by means of AFM only, without recurring to surface profilometry. By employing this double oxidation approach we were thus able to create surfaces with double frequency sinusoidal patterns, where we can arbitrarily vary the ratio between the two wavelengths λ_1/λ_2 from 10 up to 1000.

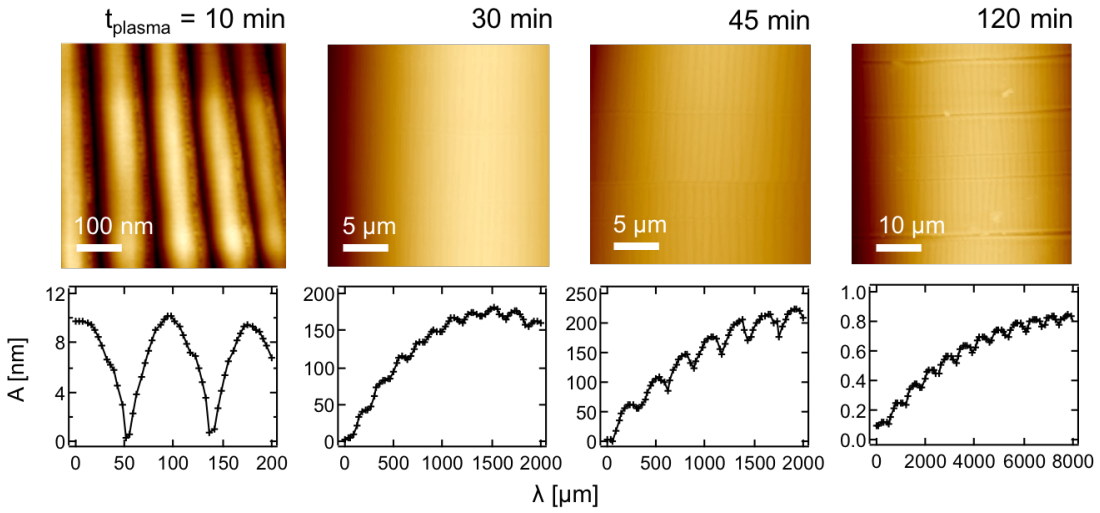

FIGURE 6.3: AFM scans for samples prestretched by $\epsilon_{prestrain} \approx 50$ % and oxidised via UVO ($D_{equivalent,UVO} = 30.24$ kJ m^{-2}) prior to air plasma oxidation (MHz, $P = 1$ mbar, $p = 7.16$ W) for variable times.

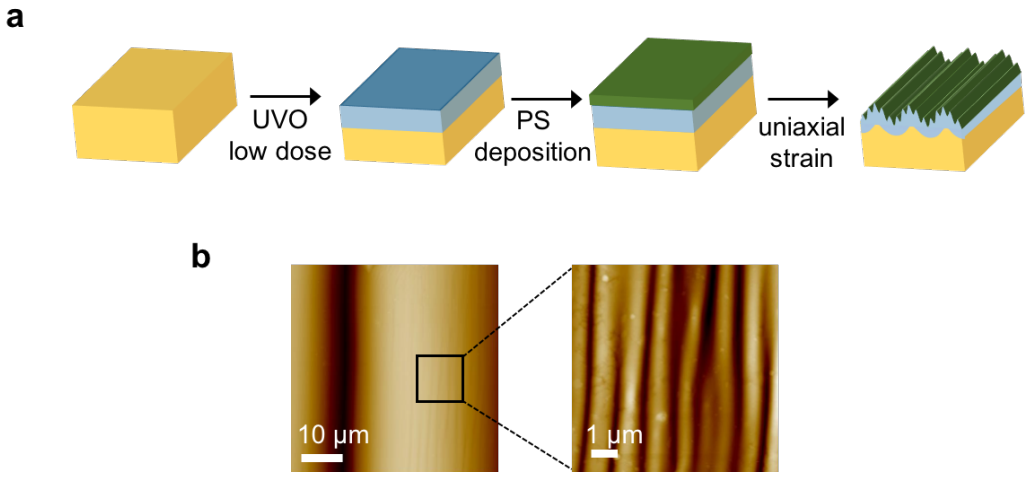

FIGURE 6.4: a) Formation of wrinkles using a 'two step' procedure. A PDMS slab is first oxidised with UVO at low equivalent dose (corresponding to $t_{UVO} =$ 60 min, $d_{lamp} = 1$ cm), leading to a single layer of thickness h_1 and modulus $\bar{E}_{f1}$ (shown in light blue). Subsequently, PS films are deposited onto the oxidised PDMS, leading to a trilayer structure. Hierarchical patterns are observed when uniaxial strain is applied to these tri-layer laminates, whose AFM scans are shown in (b).

6.1.2 Subsequent PDMS oxidation and film deposition for hierarchical morphologies

Apart from the double oxidation approach, a two step process involving PDMS oxidation followed by polystyrene film deposition has also been tested. PDMS slabs were stretched by $\epsilon_{prestrain} \approx 50$ % and treated with low UVO doses ($D_{equivalent} = 30.24$ kJ m^{-2}) to ensure a single layer was formed. PS films were then deposited on the stretched, oxidised slabs. Polystyrene (PS) films were prepared using the procedure described by Stafford *et al.* [70]. PS pellets ($M_w = 250000$ g mol$^{-}1$, Polymer Source) were dissolved into toluene to have solutions with $c_{PS} \approx 10$ mg/l. The solution was then spun coated onto Si wafers (cut into ≈ 1 cm^2 pieces and treated with UVO for 15 minutes) for 30 s at a speed of 2000 rpm, to allow for toluene evaporation and PS film formation. The wafer was then placed on the prestretched substrate, with the PS side adhering to the surface. The sandwich was then transferred to a Petri dish, which was filled with DI water: as the water wets the interface between the SiO_2 layer on the Si wafer and the film, the latter detaches and adheres to the PDMS surface. After 10 minutes the Si wafer was removed and the sample dried for 3 hours at 30 °C. Strain was then gently released and hierarchical patterns appeared, whose AFM scans are shown in Figure 6.4, along with a schematic of the process.

This double step approach also allows for an independent tuning of both generations of patterns. Indeed, the PS films fabricated according to the described procedure were characterised by a thickness of ≈ 87 nm. This was computed by fitting X-ray reflectivity data acquired on the samples, presented in Figure 6.5. By changing the solution composition or the speed at which the spin coating is carried, the thickness of the PS layer can be varied thus λ_2 can be tuned whilst λ_1 remains unchanged (provided the UVO treatment dose is kept constant).

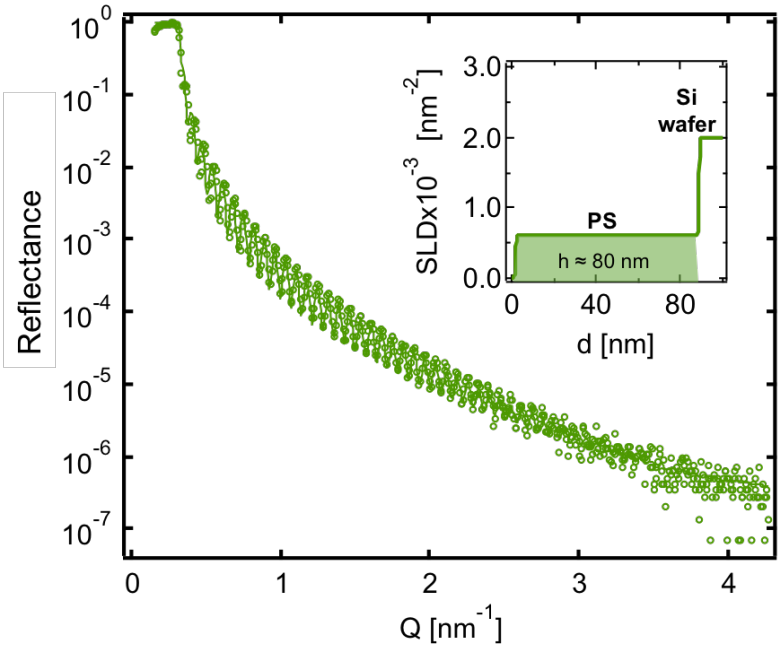

FIGURE 6.5: XRR profile acquired for a polystyrene film (fabricated according to the described procedure) deposited on a *Si* wafer. The profile was fitted with Motofit assuming a single layer sandwiched between air and the substrate. The inset shows the SLD profile.

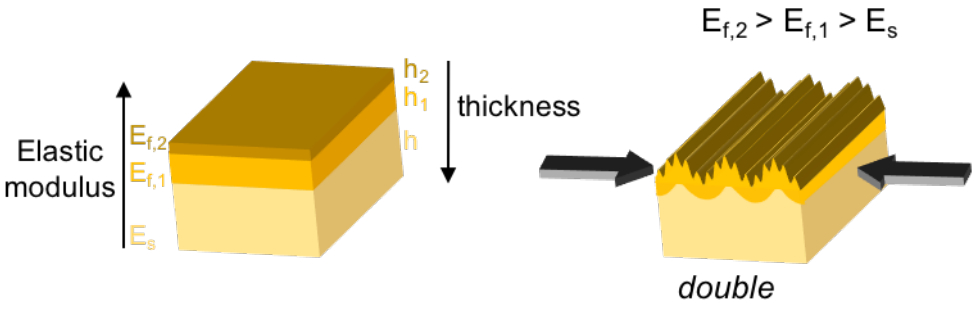

FIGURE 6.6: Schematic of the trilayer structure giving rise to double frequency sinusoidal patterns by uniaxial strain application. The layers are ordered such as the elastic modulus increases, whilst the thickness decreases from bottom to top.

6.2 Modelling of the hierarchical patterns

6.2.1 Does the order matter?

We have presented two distinct processes, each one comprising two steps, that allow creating trilayer laminates where the thickness of the two layers on top of the substrate can be independently tuned. As a result, we were able to fabricate

surfaces with hierarchical patterns with a wider range of dimensions as compared to those induced on trilayers originating via single, prolonged UVO exposure of PDMS coupons. If we look at the trilayer structures which give rise to hierarchical patterns under uniaxial strain, we can notice that they all have specific characteristics. In particular, the elastic modulus increases from the substrate to the top film which has the lowest thickness, followed by the intermediate layer, as illustrated in Figure 6.6. We have previously demonstrated through XRR experiments that prolonged UVO exposure gives rise to a top film, which is denser, thus stiffer than the intermediate one. Similarly when studying the double UVO-air plasma oxidation for nanoscale PDMS patterning, XRR proved the formation of two oxide layers, with the top one (arising from air plasma exposure) being thinner and stiffer than the compliant one. Finally, for film deposition on UVO oxidised PDMS, XRR experiments corroborated by literature data on PS films, confirmed that the same type of structure is formed, with decreasing elastic modulus and increasing thickness from top to bottom (given $\bar{E}_{PS} \approx 2.8$ GPa [169, 170] and $\bar{E}_{UVO} \approx 60$ MPa [97], corroborated by nanoindentation experiments) .

We next seek to elucidate the role of the order of the layers. Can double frequency patterns be obtained by compression of trilayers, if the order of the layers is reversed? A study carried by Nolte *et al.* [171] provides useful insights. The authors studied trilayers consisting of thick, polyelectrolyte multilayers (PEM) (thickness ranging between 80 to 200 nm, depending on the number of layers), on top of a thinner ($\approx$ 20 nm) polystyrene film, the two laying on a PDMS support. The two layers have very similar mechanical properties ($\bar{E}_{PEM} = 6.38 \pm 0.3$ GPa at ambient relative humidity, $\bar{E}_{PS} = 2.58 \pm 0.2$ GPa as reported by the authors [171]): by inducing wrinkling on these structures simple sinusoidal wrinkles were found. The wavelength of these patterns could be described by the simple bilayer model

$$\lambda_1 = 2\pi h_{tot} \left(\frac{\bar{E}_{eff}}{3\bar{E}_s} \right)^{\frac{1}{3}} \tag{6.1}$$

where one has to consider the total thickness $h_{tot} = h_1 + h_2$, and the elastic modulus of the film is replaced by an effective elastic modulus ($\bar{E}_{eff}$). The latter

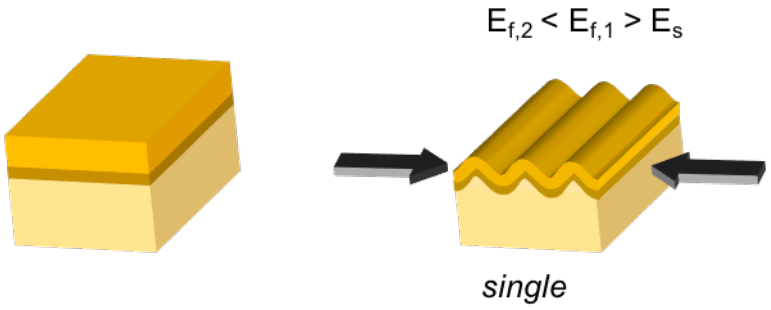

FIGURE 6.7: Schematic of the trilayer structure giving rise to single frequency sinusoidal patterns by uniaxial strain application.

can be expressed as a function of the thicknesses and mechanical properties of the layers, considering the sum of the flexural rigidities of both films to compute the resistance to buckling [43]. The relation derived is reported as follows

$$\bar{E}_{eff}/4 = \bar{E}_{f,2}\left[\left(1-\frac{k}{2}\right)^3 - \left(\phi_1 - \frac{k}{2}\right)^3\right] + \bar{E}_{f,1}\left[\left(\frac{k}{2}\right)^3 + \left(\phi_1 - \frac{k}{2}\right)^3\right] \quad (6.2)$$

where ϕ_1 is given by $\phi_1 = h_1/(h_1 + h_2)$, whilst k can be expressed as $k = \frac{1+\phi_1^2(\bar{E}_{f,1}/\bar{E}_{f,2}-1)}{1+\phi_1(\bar{E}_{f,1}/\bar{E}_{f,2}-1)}$

Based on their findings, we hypothesised that single frequency patterns appear when applying strain to trilayer laminates with a different order of the layers, presented schematically in Figure 6.7. To validate this, we had to fabricate laminate structures with $\bar{E}_{f,2} < \bar{E}_{f,1} > \bar{E}_s$ and $h_2 > h_1$. Given PDMS as the substrate, the first layer has to be as thin and stiff as possible: to this effect the oxide film resulting from air plasma exposure appears as a good candidate. In the previous sections, we have reported on the frontal vitrification of PDMS occurring via air plasma, and inferred the thickness of the oxide layer forming on the surface, which ranges between 1-20 nm, by employing both X-ray and neutron reflectivity [164]. Single frequency sinusoidal patterns were found to arise when applying uniaxial strain to the resulting bilayers, whose characteristic dimensions were previously reported as a function of the experimental conditions. By recalling that, at $\epsilon_{prestrain} \approx 20$ %, the pattern wavelength is expressed as $\lambda_{20\%} = \frac{2\pi}{1.21}(\bar{E}_{plasma}/3\bar{E}_{PDMS})^{1/3}$, the

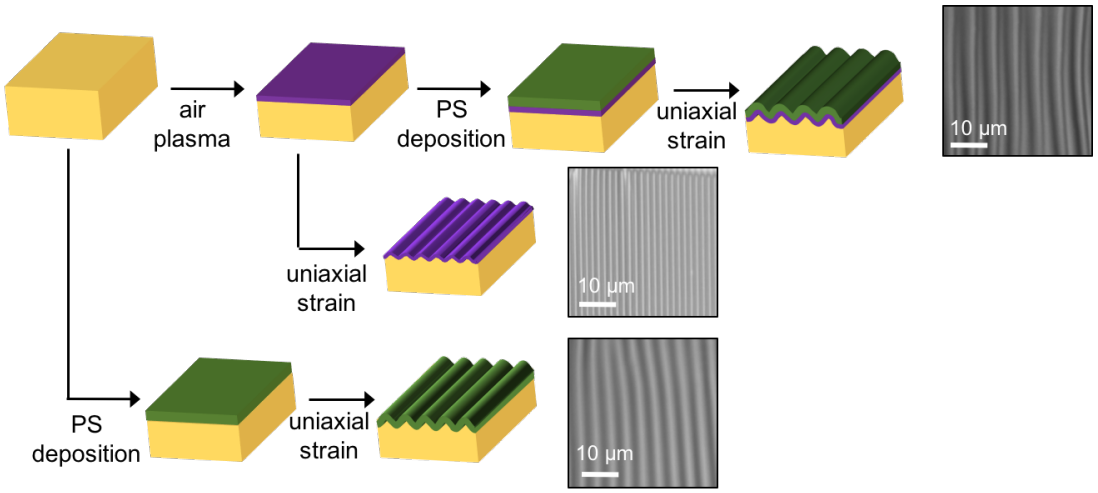

FIGURE 6.8: Schematic of pattern formation by wrinkling of multilayers. PDMS samples are oxidised via air plasma, resulting in the formation of a thin, stiff layer; PS film deposition is carried subsequently, leading to trilayer structures. Single frequency sinusoidal patterns arise when uniaxial strain is applied, as illustrated by optical microscopy images. The characteristic dimensions of the wrinkles are larger as compared to those arising on plasma oxidised PDMS/PDMS or PS/PDMS bilayers, whose optical microcopy images are also reported.

measured λ and h at fixed conditions allow estimating $\bar{E}_{plasma} \approx 24$ GPa (given $\bar{E}_{PDMS} = 2.13$ MPa). Now, on top of this glassy layer, a third layer, thicker and softer, has to be placed. We opted for a polystyrene film, which was floated on the oxidised PDMS. The thickness of these PS films was determined by means of XRR at ≈ 87 nm. To determine the elastic modulus, we performed wrinkling experiments by depositing PS films on prestretched PDMS substrates: knowing the thickness, by measuring the wavelength we obtained a value of $\bar{E}_{PS} \approx 2.5$ GPa from the bilayer model in the high deformation regime. The fabricated PS films characteristics thus comply with the requirements, having a bigger thickness and a lower elastic modulus compared to the plasma oxide layer.

We therefore induced wrinkling on the resulting PS/PDMS oxidised/PDMS trilayers by applying uniaxial stran. As expected, single frequency, sinusoidal wrinkles were obtained, confirming our hypothesis that hierarchical patterns are subject to a specific order of the layers. To describe this wrinkling mechanism, we took advantage of the model presented previously [171]. Knowing the thickness and

elastic modulus of the oxide layer at the conditions chosen (h_{plasma} from reflectivity experiments, $\bar{E}_{plasma} \approx 24$ GPa from the previous wrinkling experiments), as well as the thickness of the PS layer, we first computed $\bar{E}_{eff}$ from the morphological characterisation (equation 6.1), thus utilised the effective modulus to obtain $\bar{E}_{PS}$ (equation 6.2). We found that the value inferred $\bar{E}_{PS}$ was in agreement with the previous one evaluated in case of a bilayer. This validates the findings and the applicability of the model.

The findings are shown schematically in Figure 6.8 which also reports representative optical microscopy images of sample morphologies.

6.2.2 Double bilayer model for hierarchical patterns characterisation

We thereby established the sequence of thicknesses and elastic moduli which gives rise to nested sinusoidal patterns by mechanical wrinkling. It is now interesting to evaluate how the wavelengths of the two generations of patterns relate to the layer thicknesses and elastic moduli. Our hypothesis is that, under certain conditions, each wrinkling mechanism can be described using the simple bilayer model, which applied in this case would yield

$$\lambda_1 = 2\pi h_1 \left(\frac{\bar{E}_{f1}}{3\bar{E}_s} \right)^{\frac{1}{3}} \tag{6.3}$$

$$\lambda_2 = 2\pi h_2 \left(\frac{\bar{E}_{f2}}{3\bar{E}_{f1}} \right)^{\frac{1}{3}} \tag{6.4}$$

To validate this, we first focused on laminate structures obtained via PDMS oxidation. When simply oxidising PDMS by air plasma exposure, we demonstrated that a single layer is formed [164], whose elastic modulus can be inferred from the morphological characterisation (at selected process conditions MHz, $p = 7.16$ W, $P = 1$ mbar, $t = 30$ min) by using the simple bilayer model ($\bar{E}_{plasma} \approx 24$ GPa). We demonstrated that trilayer laminates are formed by treating the PDMS with

UVO ($D_{equivalent}$ = 30.24 kJ m^2) prior to air plasma. We computed the thickness of the top layer (resulting from air plasma exposure) at the same plasma process conditions employed previously. When releasing $\epsilon_{prestrain} \approx 50$ %, we reported that double frequency sinusoidal patterns are observed, with wavelengths λ_2 (arising from the mismatch between the plasma and the UVO oxide layers) and λ_1 (arising from the moduli contrast between the UVO oxide layer and the PDMS substrate). The wavelength λ_2 was measured: by assuming a value of $\bar{E}_{UVO} \approx 60$ MPa, we applied equation 6.4 and got $\bar{E}_{plasma} \approx 23$ GPa. This value is well in agreement with the one computed previously in case of a simple bilayer.

Thereafter, we considered bi- and multi- layers comprising PS films. We started by simple PS/PDMS bilayers giving rise to single frequency, sinusoidal patterns upon uniaxial strain application. By measuring the wavelength, knowing the thickness of the PS film and the elastic modulus of the substrate, we calculated $\bar{E}_{PS} \approx 2.5$ GPa. We next turned to laminate structures obtained by PS deposition on oxidised PDMS. First, we considered wrinkling of trilayers obtained by depositing PS on air plasma oxidised PDMS, resulting in single frequency sinusoidal features, and inferred the PS modulus by applying the model [171] ($\bar{E}_{PS} \approx 2.3$ GPa). Finally, we focused on the double frequency sinusoidal features observed upon wrinkling of PS/UVO oxide/PDMS trilayers. We applied equation 6.4 to compute $\bar{E}_{PS}$ from the measurement of λ_2, by assuming $\bar{E}_{UVO} \approx 60$ MPa. Again, we found that $\bar{E}_{PS} \approx 2.6$ GPa, which agrees with the values previously calculated as well as with those reported in the literature [169, 170].

These findings (grouped in Tables 6.1-6.2) corroborate our initial hypotheses and confirm the possibility to model double frequency pattern formation via the simple bilayer model applied twice. These results are of significant importance as they enable us to predict the feature sizes arising from wrinkling of tri-layer laminate structures.

			Bilayer			
	Film		*Substrate*	$\bar{E}_s$ *[GPa]*	h *[nm]*	λ *[nm]*	$\bar{E}_f$ *[GPa]*
single	Plasma$_{ox}$ PDMS		PDMS	0.00213	14	1350	24 ± 1.2
			Trilayer				
	Film 2 (top)	*Film 1 (bottom)*	*Substrate*	$\bar{E}_{f,1}$ *[GPa]*	h_2 *[nm]*	λ_2 *[nm]*	$\bar{E}_{f,2}$ *[GPa]*
double	Plasma$_{ox}$ PDMS	UVO$_{ox}$ PDMS	PDMS	0.06	8	250	23.1 ± 1.1

TABLE 6.1: Summary of the results obtained when applying the simple bilayer model [43, 46, 47] (**bilayer**), and equations 6.3-6.4 (**trilayer**, *double* frequency patterns), to infer the elastic modulus of the PDMS plasma oxide layer (purple).

				Bilayer				
	Film		*Substrate*	$\bar{E}_s$ *[GPa]*	h *[nm]*	λ *[nm]*		$\bar{E}_f$ *[GPa]*
single	PS		PDMS	0.00213	87	4000		2.5 ± 0.2
				Trilayer				
	Film 2 (top)	*Film 1 (bottom)*	*Substrate*	$\bar{E}_{f,1}$ *[GPa]*	h_2 *[nm]*	λ_1 *[nm]*	λ_2 *[nm]*	$\bar{E}_{f,2}$ *[GPa]*
single	PS	Plasma$_{ox}$ PDMS	PDMS	24	87	-	5500	2.3 ± 0.2
double	PS	UVO$_{ox}$ PDMS	PDMS	0.06	87	26000	1300	2.62 ± 0.18

TABLE 6.2: Summary of the results obtained when applying the simple bilayer model [43, 46, 47] (**bilayer**), equations 6.1-6.2 (**trilayer**, *single* frequency patterns) and equations 6.3-6.4 (**trilayer**, *double* frequency patterns), to infer the elastic modulus of the PS layer (green).

6.3 Impact of morphology on surface wetting

So far we have demonstrated the possibility of fabricating surfaces with tunable hierarchical patterns. These morphologies play an important role in modifying the wetting properties of a substrate, as discussed previously.

We thereby wanted to test how different patterned surfaces affected wetting. To do this, we fabricated samples following three different methods. PDMS slabs were stretched by $\epsilon_{prestrain} = 50$ % and oxidised via UVO alone ($D_{equivalent} = 30.24$ kJ m^{-2}) as well as subsequent UVO and air plasma (MHz, $p = 7.16$ W, $P = 1$ mbar) for variable times ($t_{plasma} = 5$ and 45 minutes). By keeping the UVO exposure constant, upon strain removal we obtained patterns with constant $\lambda_1 \approx 40$ μm and λ_2 variable between 0, 50 nm and 1μm. The oxidative treatment results in the loss of PDMS hydrophobicity. The fabricated samples were thus utilised as stamps,

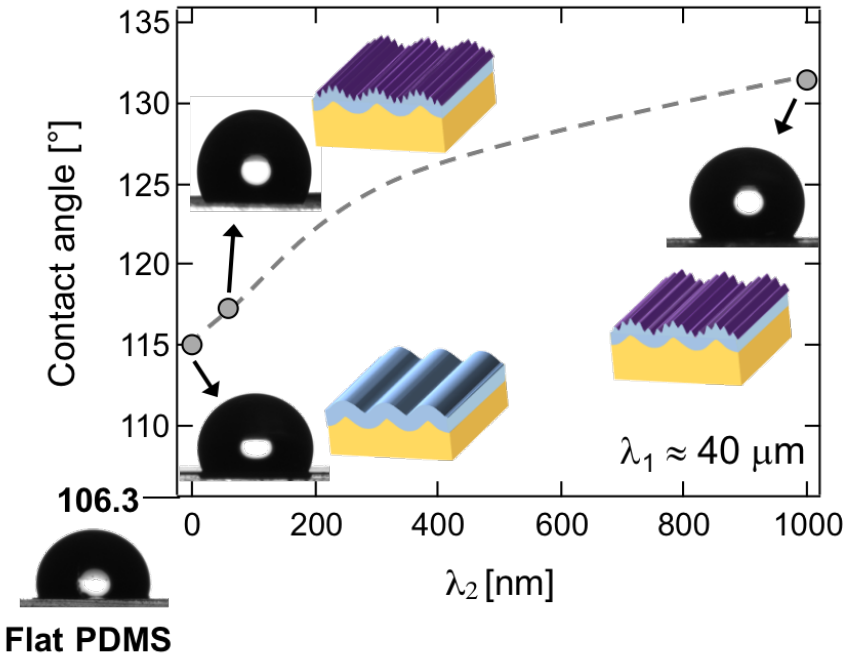

FIGURE 6.9: Variation of water contact angle on PDMS as a function of surface patterns. Schematics of the different morphologies tested are also presented: in all samples λ_1 was constant whilst we changed λ_2. The contact angle is reported also for a flat PDMS slab. The line serves for guidance only.

and the patterns were replicated into fresh PDMS. A rectangular hole of ≈ 1 cm^2 area was cut into neat PDMS coupons (area ≈ 2 cm^2). The frame was placed on the patterned surface, so that the hole was enclosing the wrinkled area. Fresh, uncrosslinked PDMS was then poured to fill the hole and the sample was cured at the conventional conditions. The neat PDMS slab was then removed from the patterned (oxidised) surface. By doing this we transferred the morphology on a hydrophobic substrate.

Basic water contact angle experiments were then performed on the replicas, employing a contact angle goniometer (Rame-hart). The results are presented in Figure 6.9. We notice that the presence of single frequency sinusoidal patterns already results in an increase in the contact angle as compared with flat PDMS. The effect of the morphology becomes more significant in presence of a second generation of patterns: more specifically, the water contact angle was found to increase going from nm to μm scale secondary features. Superhydrophobicity results from the combined effect of roughness and low-surface energy. The preliminary results

obtained thus open an attractive route for the fabrication of superhydrophobic surfaces (water contact angle > 150 °) through the use of appropriate low-surface energy coatings [172].

Chapter 7

Measuring the mechanical properties of thin drying films via wrinkling

Up to now, we have focused on establishing wrinkling of multilayers as a scalable patterning method from the nano to the macro scale. We carefully engineered both the geometrical and mechanical properties of the layers in order to vary the dimensions of the patterns resulting from mechanically induced wrinkling. We wanted specific λ and A and we thus employed a series of single or double step processes to vary h and E_f as well as the number of layers, resulting in a wide range of single frequency and double frequency sinusoidal patterns.

Now, what if we look at the problem from a different perspective? Or, in other terms, what if we have films and we want to determine their mechanical properties? Intuitively, if we deposit these films on appropriate substrates and induce mechanical wrinkling on the resulting bilayers, we can use the measured characteristic dimensions to compute the elastic modulus of the film, making use of the bilayer equations. The literature has plenty of examples where wrinkling is utilised to mechanically characterise thin films [41, 70, 71, 126, 128], through a method known as SIEBIMM [70, 126]. This has proven to be more effective than

conventional methods, as for example nanobubble inflation or AFM nanoindentation. In the first case the thin film is deposited to cover a circular hole on a substrate, and clamping at the edges occurs by means of adhesive forces: when pressure is applied from underneath the hole, the film deforms, creating a 'bubble'. The resulting change in shape can be related to its mechanical properties. The method has proven to be suitable when dealing with films down to 10 nm thicknesses: however it implies a very complex and generally expensive setup [173]. AFM nanoindentation measurements on thin films, on the other hand, can be severely affected by the mechanical properties of the substrate supporting the film: a prerequisite for obtaining accurate estimates of the elastic modulus is that the nanoindentation depth is no larger than 10 % of the film's thickness [174]. Moreover the technique requires sophisticated probes to indent the surface and the data analysis is generally non-trivial [127].

Therefore wrinkling has been established as a powerful tool for the mechanical characterisation of thin films. Wrinkled patterns have been mechanically induced on films whose properties remain unchanged with time, and the elastic modulus inferred from the mophological characterisation. Dynamic experiments have also been employed to determine the viscoelastic response of polymer thin films, by evaluating how stress induced patterns on those films evolve with time [175, 176].

What if we have films whose elastic modulus changes over time, for example as a result of water loss during drying? In this case we had to employ the wrinkling method in a time-resolved way. Our main motivation is that there are a lot of fields, ranging from paints, foods, agrochemicals, and personal care, including deodorants and cosmetics, which deal with thin films whose mechanical properties evolution is of fundamental importance [177]. In this study, as a model system we selected a ternary blend comprising an inorganic salt, aluminum chlorohydrate (ACH), and a humectant, glycerol, in water. This mixture was found to form a glass upon water loss and film formation, and crystallisation was not observed unlike other ACH species [178–181]. Hydroxyaluminum solutions have diverse applications such as coagulants in wastewater treatments and catalyst support in pillared clays [182] as well as being the main active ingredient in antiperspirant formulations

[180, 181], one of the largest health and beauty product categories. However, their rheomechanical behavior and speciation remains poorly understood. In this Chapter, we propose a method to induce wrinkling on these films as they dry and dynamically infer their mechanical properties under a wide range of conditions. This work was carried out in collaboration with Giulia Ferretti and the main results have been published in [183].

7.1 Methodology

7.1.1 Solution Preparation

The ternary solutions were prepared by mixing aluminum chlorohydrate (ACH) (50 wt % hydrated dialuminum chloride pentahydroxide aqueous solution; Summit Research Laboratories Inc.), glycerol (purity $\geq$ 99.5%; Sigma-Aldrich), and deionised water (obtained from a Milli-Q source). The mixtures were homogenised, and equilibrated overnight. The amount of ACH was determined in order to have a fixed mass composition of 15%, whilst the glycerol content was varied from 0 to 15 wt %, with the remainder of the solution being composed of water. Upon drying, only water is lost from the system [184]. As the initial mass fraction of ACH is kept constant in all solutions, throughout the next sections the compositions are indicated via the initial mass fraction of glycerol $c_{0,glycerol}$.

7.1.2 Substrate Choice

Following the preparation of the model solution, we then had to choose an optimal substrate on which depositing the solution which eventually solidifies upon drying, leading to film formation. In all the experiments presented in the previous Chapters, PDMS was utilised as the substrate, due to its unique features like near-incompressibility (Poisson ratio, $\nu \approx 0.5$ [109]), tunable modulus, and large elongation at break ($\epsilon \approx 200$ % [110]), which are extremely convenient for wrinkling experiments. However, native PDMS is hydrophobic: this means that,

when depositing the solution on the surface, wetting is not observed. Wetting of the substrate is of upmost importance if we want to ensure the formation of a planar film upon solution drying.

This issue can be solved by prior PDMS oxidation, which renders the substrate hydrophilic, permitting full wetting of the aqueous solution and planar film formation. Oxidised PDMS is therefore selected as the optimal substrate. However, trilayer analysis of the wrinkling data may thus be required, as detailed below.

7.2 Bilayer formation and mechanical wrinkling

Figure 7.1 illustrates the procedure adopted to form the bilayers and then inducing wrinkling. We started by prestretching PDMS slabs (prepared according to the procedure detailed in Chapter 2) by $\epsilon_{prestrain}$. The prestretched coupons are then treated by air plasma oxidation (MHz, p = 7.16 W, P = 1 mbar), to render the surface hydrophilic. An initial wet film thickness of $\approx$ 30 μm was deposited on the oxidised PDMS slabs, by covering an area of 1.5 cm $\times$ 1.5 cm with a volume of 7 μL of solution. The liquid films were allowed to dry over time, at ambient temperature (25 °C) and relative humidity of 25 %, while mass changes were monitored with a Sartorius 1702 balance. Three different stages could be identified during drying. Initially, the film is liquid: directional solidification then occurs, starting from the surface, leading to the formation of a crust on top of the bulk liquid, corroborated by tack measurements [184]. Eventually the entire film solidifies. At different stages during the drying process, strain can be released and the surface morphology can be characterised. We expect diverse buckling responses as a function of water content: within the sinusoidal regime, we can utilise the measurement of λ and A to infer the plane elastic modulus $\bar{E}_f$. From $\bar{E}_f$, the elastic modulus can be obtained by assuming $\nu = 0.27$ for the inorganic salt film [185].

The method proposed resulted in samples exhibiting wrinkling in the relaxed state, previously defined as ON samples. Alternatively, OFF samples can be fabricated:

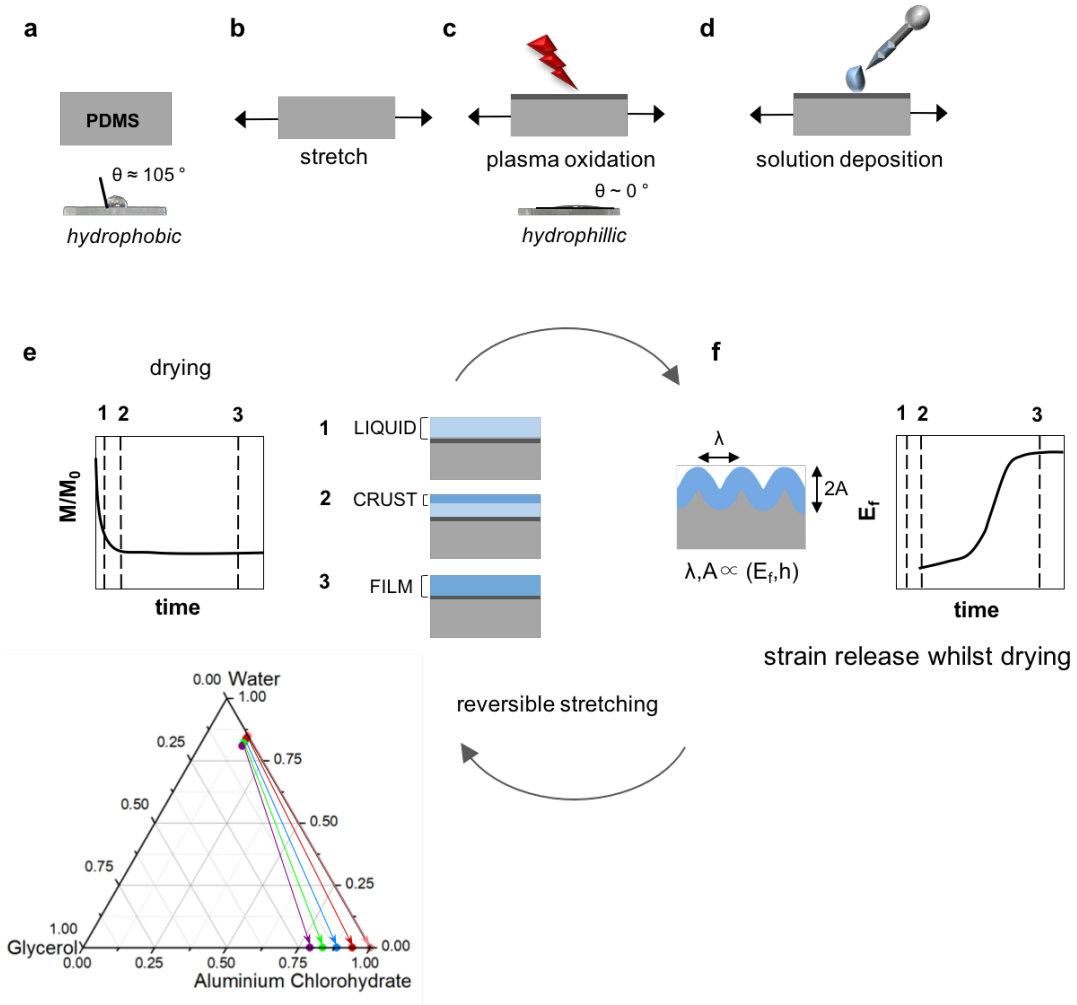

FIGURE 7.1: Schematic of the proposed experimental approach. A hydrophobic PDMS substrate (a) is stretched (b) and then (c) oxidised to enable wetting and planar film formation; (d) the solution of interest is then deposited and allowed to dry for prescribed time intervals; the ternary diagram drying pathways as a function of initial solution concentration are illustrated. The liquid film starts drying (e) and may form a transient 'crust' before entirely hardening. During the drying process, the film mass decreases until an asymptote is reached, while (f) the sandwich layer is mechanically interrogated by releasing strain. Topographic analysis of the wrinkling profile enables the calculation of the elastic modulus of the film throughout the pathway.

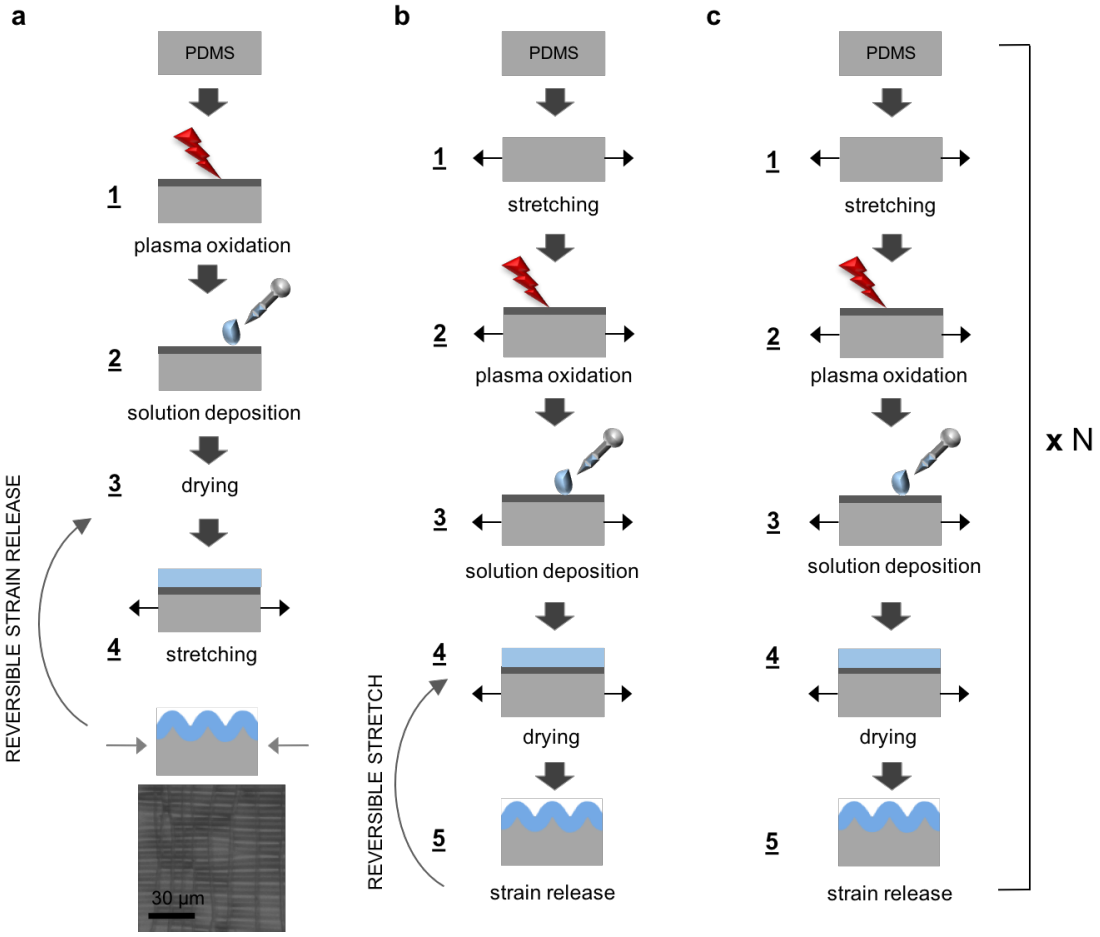

FIGURE 7.2: Schematic of three different procedures utilised to induce wrinkling on drying films. The samples prepared through (a) show wrinkles in the strained state (OFF samples). An optical microscope image of a wrinkled OFF sample is reported ($c_{0,glycerol}$ = 2 wt %, RH = 40%, T = 20 °C). Samples prepared following (b) show wrinkles in the relaxed state, allowing N measurements to be made on a single sample. Procedure (c) is analogous to (b), except that each measurement is taken on a fresh sample, corresponding to N measurements on N samples, but further reducing surface cracking.

in this case substrate oxidation and solution deposition take place in absence of strain. At different stages of drying, wrinkling can be induced upon stretching and consequent orthogonal compression. The procedures leading to the two distinct samples are illustrated in Figure 7.2a (for OFF samples) and b (for ON samples). The comparison between the two shows that in case of OFF samples, the film is formed when the substrate is in the relaxed state and, while the procedure requires fewer steps, these samples present two main drawbacks. Firstly, when applying this method cracks were found to form in the orthogonal direction of application of tensile strain, as shown in a representive optical microscopy image (Figure

7.2a). Secondly, as wrinkling occurs under tension, the samples needed to be characterised mounted on the strain stage, requiring a more complex experimental setup.

ON samples thus proved to be more suitable for our purposes. As shown in the schematic in Figure 7.2b, after a certain drying time, strain is released and sinusoidal wrinkles are observed in a certain range of conditions, whose characteristic dimensions can be measured and then directly related to the mechanical properties of the drying film. Afterwards, the sample can be stretched again and allowed to dry further until the desired time, at which point the strain can be released and the elastic modulus computed again from the sample morphology. Therefore, the mechanical characterisation of thin drying films can be carried by taking N measurements on a single sample via reversibly releasing and applying the same strain during drying. However, repeated stretching inevitably increases cracking on the surface. To further eliminate crack-formation, the more laborious procedure in Figure 7.2c has been applied for the experiments (unless otherwise stated), which requires one sample per measurement.

7.2.1 Substrate oxidation for minimal impact in drying kinetics

As discussed previously, PDMS oxidation is performed prior to solution deposition. On one hand this process ensures wetting of the hydroxyaluminium solutions; on the other hand the surface treatment can potentially alter the drying kinetics. We thus prepared a series of PDMS substrates, oxidised with air plasma (MHz, p = 7.16 W, P = 1 mbar) for variable times t_{exp} = 2, 20 and 40 minutes. The model solution was deposited on the substrates and allowed to dry at (T = 25 °C and RH = 25 %). An impermeable polyester support sheet was used as a reference substrate. Right after the film deposition we measured the overall mass of PDMS support and film $M(t_{drying}{=}0)$: the mass evolution $M(t_{drying})$ was recorded as a function of time. Normalised mass loss $M(t_{drying})/M(t_{drying}{=}0)$ is plotted in Figure 7.3 for the different substrates. From the graph one can notice that, for

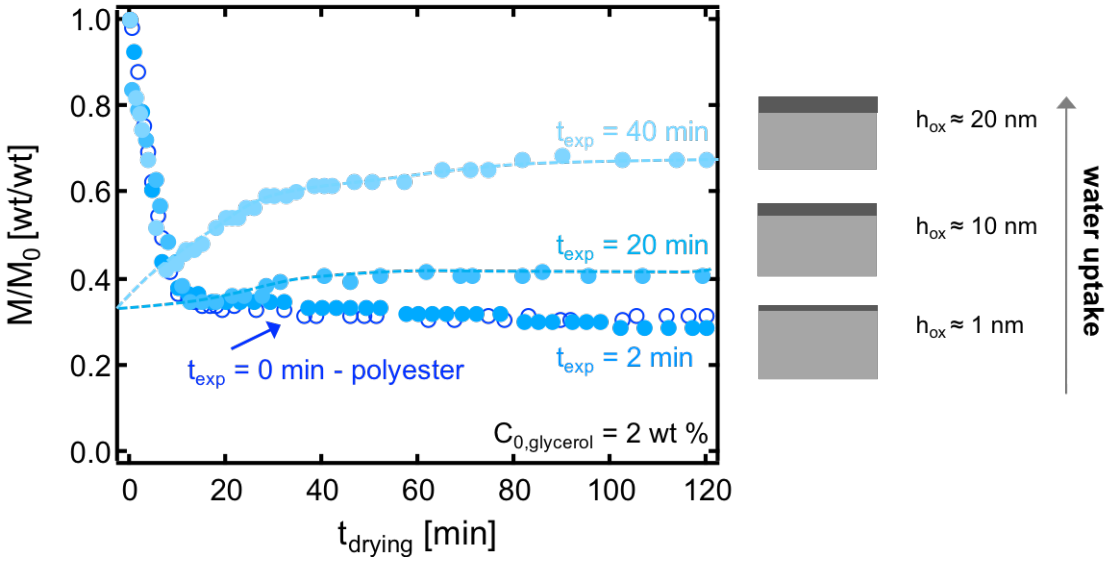

FIGURE 7.3: Normalised mass loss of a film of initial glycerol composition $c_{0,glycerol}$ = 2 wt % during drying (T = 25 °C and RH = 25%) on various substrates: (○) polyester sheet (impermeable reference) and (●) PDMS oxidised in air plasma at P = 1 mbar and p = 7.16 W, for 2 to 40 min. Increasing oxidation causes PDMS swelling by water uptake, but a plasma exposure of t_{exp} = 2 min yields wetting surfaces with comparable drying profile to the polyester reference.

the longer plasma exposures (t_{exp} = 20 and 40 min), after an initial mass loss decay due to water evaporation, the film mass appears to increase again at long times. Evidently, long plasma exposures cause the hydrophilic PDMS to uptake water and swell, at time scales commensurate with film drying. However, shorter plasma exposures cause negligible swelling, yielding mass loss profiles indistinguishable from the control measurements and enabling surface wetting and planar film formation. Based on these observations, we chose to expose PDMS samples to air plasma for 2 minutes: this ensures simultaneous wetting of the substrate by the ternary solution, to enable planar film formation, and impermeability of the support, preventing inadvertent composition and dimensional changes. Shorter exposure times did not guarantee adequate wetting of the substrate.

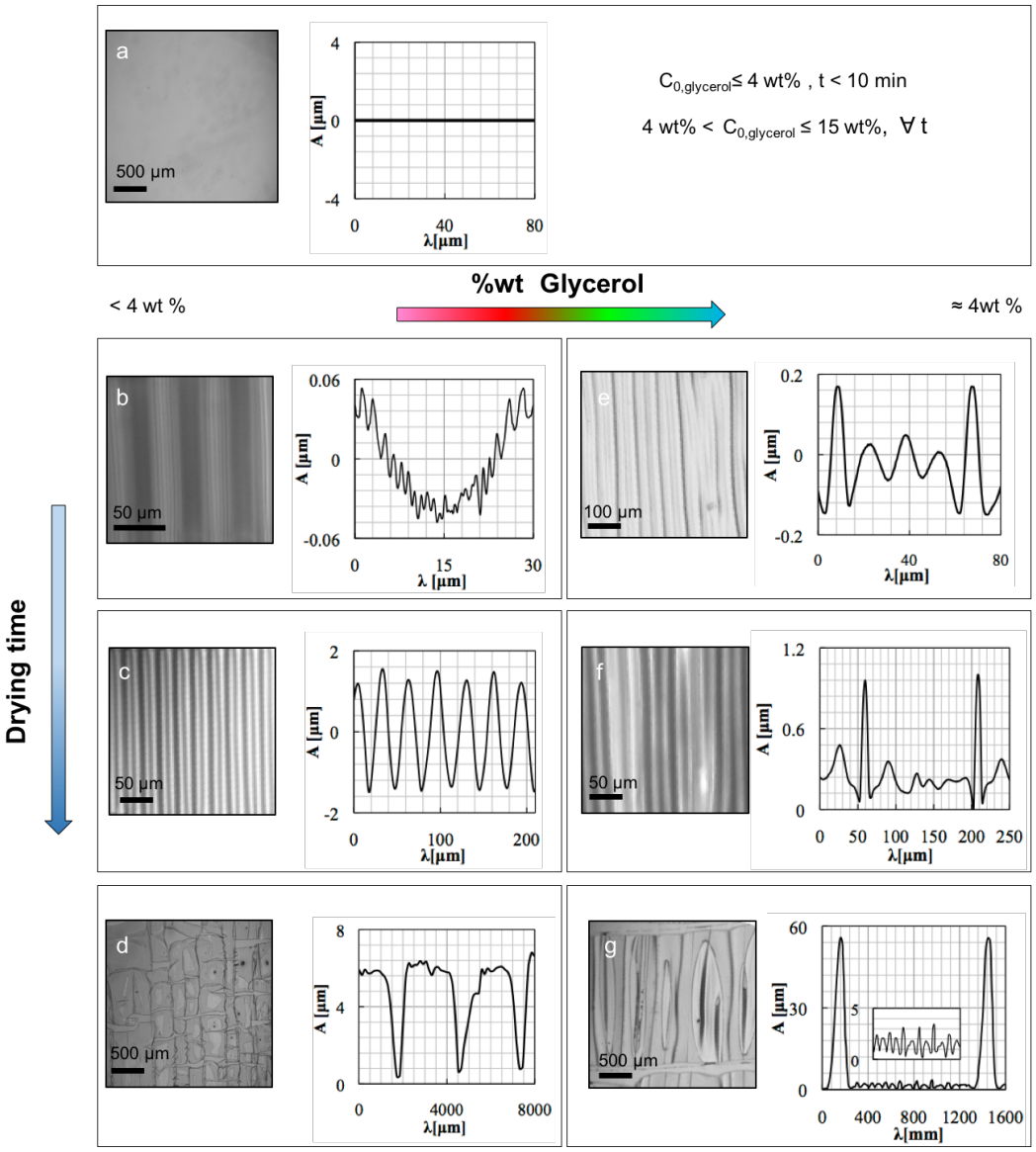

FIGURE 7.4: Optical microscopy, profilometry, and AFM data of surface patterns observed in the films upon strain removal after drying. a) Absence of wrinkles ($c_{0,glycerol}$= 0-4 wt %, $t_{drying} < 10$ min; $c_{0,glycerol} > 4$ wt %, for all drying times). b) Double frequency sinusoidal patterns ($c_{0,glycerol}$= 2 wt %, t_{drying}= 10 min). c) Sinusoidal wrinkles ($c_{0,glycerol}$= 2 wt %, $t_{drying} = 12$ min). d) Film fracture and crack formation ($c_{0,glycerol} = 2$ wt %, $t_{drying} = 150$ min). e-g) Patterns deriving from stress localisation and ridging effects ($c_{0,glycerol} = 4$ wt %, $t_{drying} = 30$ min to 2 h). All data refer to drying conditions of $T = 25$ °C and $RH = 25\%$ and PDMS substrates oxidised at $P = 1$ mbar, $p = 7.16$ W, and $t_{exp} = 2$ min.

7.3 Evolution of wrinkling morphologies with drying time and solution composition

Having established the experimental procedure, we performed a series of experiments, where we evaluated how both $c_{0,glycerol}$ and drying time impact the films responses to buckling. Films with different initial compositions were allowed to dry for selected time intervals on 2 min oxidised, PDMS supports, prestretched by 20 %. Upon strain removal, a variety of patterns could be observed, arising from the moduli contrast between the film and the substrate. Specifically we found that at early drying times ($t_{drying} \leq 10$ minutes) no pattern formation could be observed, with the liquid film surface remaining planar (Figure 7.4a). The same applied to films with $c_{0,glycerol} > 4\%$, which remained flat upon strain removal even after long drying times. Solutions with initial concentration of glycerol between 0 and 3 wt % exhibited two stages of sinusoidal pattern formation. At drying times between 9 and 11 min, double frequency sinusoidal profiles were observed, akin to a wrinkling cascade [94, 168] as shown in Figure 7.4b. These patterns resemble those discussed in Chapters 5-6, which were found to be caused by a structure consisting of a top and intermediate layers and a substrate, with decreasing elastic moduli. In case of film drying, the hierarchical patterns can be associated to the formation of a transient crust [186] during rapid evaporation, effectively creating an additional surface skin at intermediate times. The short wavelength wrinkles ($\lambda_2 \approx 3$ μm) arise due to the contrast between the top skin and intermediate layer, while the long wavelength profile ($\lambda_1 \approx 30$ μm) arises due to the dominant intermediate layer and the substrate, persisting over longer times. At increasing drying times, within $12 \leq t_{drying} \leq 120$ min (Figure 7.4c), single frequency, sinusoidal wrinkles form, readily enabling the mechanical characterisation of the drying film. Eventually, after 120 min, delamination and cracking prevail (Figure 7.4d), as the films become excessively brittle upon full water loss.

Within the sinusoidal range, we evaluated the effect of the prestrain $\epsilon_{prestrain}$ on the resulting pattern morphology. A representative system with $c_{0,glycerol} = 2$ wt % was selected for this evaluation and allowed to dry for 12 min at 25 °C and 25 %

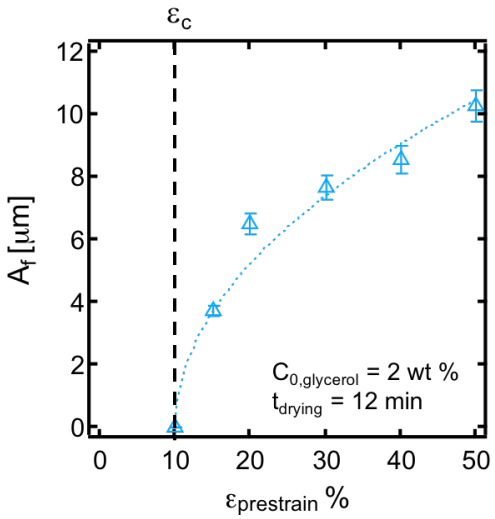

FIGURE 7.5: Wrinkling amplitude on the film surface as a function of PDMS substrate prestrain, for a film with $c_{0,glycerol} = 2$ wt % at 12 min drying time ($T = 25$ °C and 25 % RH). The line represents a fit according to the bilayer model [43, 46, 47].

RH. The wrinkling amplitude, which depends strongly on the prestrain (according to the bilayer model[43, 46, 47]), was plotted as a function of $\epsilon_{prestrain}$, as shown in Figure 7.5. The measurements showed that a critical value of $\epsilon_c \approx 10$ % had to be exceeded for wrinkling to be observed : thereafter, an increase in $\epsilon_{prestrain}$ results in an increase in A_f. Now, as the critical strain required to trigger the instability depends on the moduli contrast between the film and the substrate, we expect it to decrease as the film dries further. In other words, if we found $\epsilon_c \approx 10$ % at the early stages of drying, by choosing $\epsilon_{prestrain} = 20$ % we are sure to exceed the critical strain within the accessible experimental window.

Initial glycerol concentrations of ≈ 4 wt % led to more complex pattern morphologies, evolving from double scale wrinkling (Figure 7.4e) to ridge formation (Figures 7.4f-g) with increasing drying time. This can be explained by considering that sinusoidal wrinkling is only observed when the applied strain, yet exceeding ϵ_c, remains below a critical value, referred as ϵ_L. The latter again depends on the properties of the bilayer (e.g. the shear moduli contrast, as seen in Chapter 1 [52]): when $\epsilon_{prestrain}$ exceeds ϵ_L, nonlinearities in the strain energy functions cause stress localisation [54, 60, 187]. Considering the above, the presence of ridges at 4 wt % glycerol concentration can be interpreted by means of $\epsilon_L \leq 20\%$ and of the

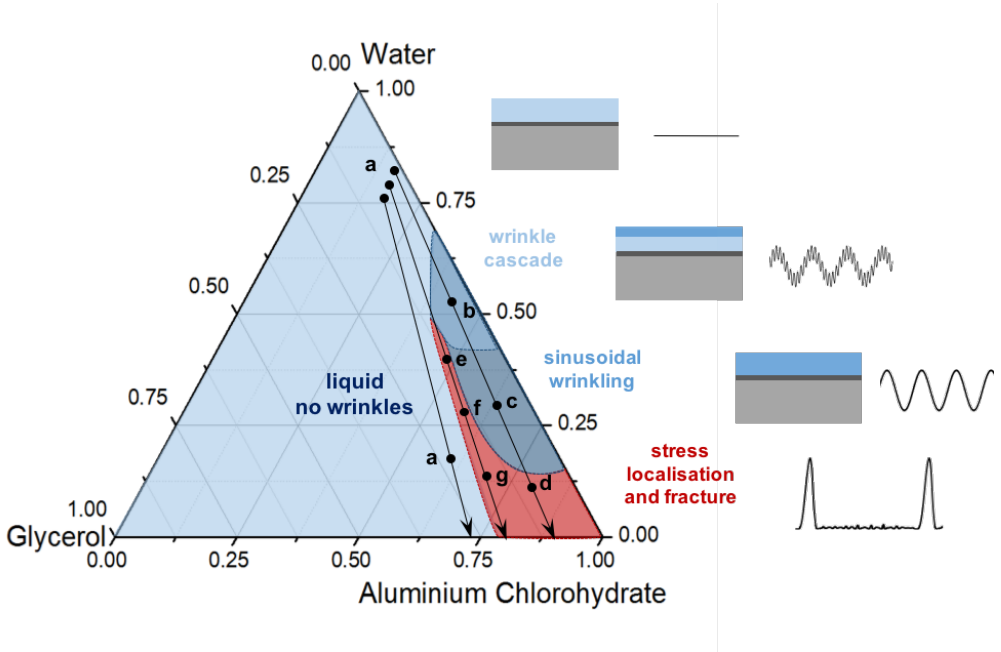

FIGURE 7.6: Different pattern formation regimes observed as a function of film composition mapped on the ternary diagram, along with the schematic of the corresponding surface profiles. The arrows represent drying pathways for $c_{0,glycerol} > 4$ wt %, $c_{0,glycerol} \approx 4$ wt %, and $c_{0,glycerol} < 4$ wt %, and the letters a-g correspond to the panels in Figure 7.4.

order of ϵ_c, since no pattern formation was observed below 20% strain.

Films with 5-15 wt % initial glycerol concentration did not exhibit wrinkling at any time during drying, even for prestrains up to 40 %. Evidently, either $\epsilon_c > 40$ %, corresponding to a relatively low modulus contrast with respect to the PDMS substrate, or the film remains a viscous liquid throughout, relaxing rapidly any surface pattern formed under compression. The addition of glycerol, a well-known plasticizer, above 4 wt % was thus found to promote film flexibility and decrease the film's elastic modulus sufficiently to suppress wrinkle formation.

The different wrinkling regimes observed as a function of film composition were also mapped onto a ternary diagram in Figure 7.6, including regions where wrinkling does not occur ($\epsilon_{prestrain} < \epsilon_c$), sinusoidal wrinkles ($\epsilon_c \leq \epsilon_{prestrain} < \epsilon_L$), and stress localisation and ridging ($\epsilon_{prestrain} \geq \epsilon_L$), crack formation, and delamination. Within the sinusoidal wrinkling region, we subdivided a range of concentrations (and corresponding drying times at $T = 25$ °C at 25 % RH) for which double frequency sinusoidal wrinkling is observed and referred to as a wrinkling cascade.

7.4 Sinusoidal wrinkles for mechanical properties evaluation

Control experiments allowed for mapping the wrinkling morphologies observed as a function of $c_{0,glycerol}$ and t_{drying}. We therefore identified the range of conditions leading to sinusoidal pattern formation. Now, within this experimental window, we can determine the elastic modulus of the film, by simply measuring λ_f and A_f, and use the appropriate model to infer E_f.

7.4.1 Determination of the appropriate model for the elastic modulus calculation

Intuitively one would use a simple bilayer model to interpret the morphology data: however, this requires a little more thinking. Indeed we have commented about the need of oxidising PDMS prior to solution deposition. As extensively reported in the previous Chapters, the oxidative treatment leads to the formation of a 'glassy' film, with thickness h_{ox}. Therefore, when the hydroxyaluminium solution is deposited and the film is formed, we effectively have a trilayer structure, represented schematically in Figure 7.7. The moduli sequence does not guarantee the formation of hierarchical patterns: however, λ_f and A_f could actually be influenced by the presence of the intermediate oxide layer and a trilayer model could be necessary to infer E_f. The trilayer model [171] , applied to this system yields

$$\lambda_f = 2\pi h_f \left(\frac{\bar{E}_{eff}}{3\bar{E}_s} \right)^{1/3} \tag{7.1}$$

$$A_f = h_f \left(\frac{4\epsilon}{\left(3\bar{E}_s/\bar{E}_{eff}\right)^{2/3}} - 1 \right)^{1/2} \tag{7.2}$$

where

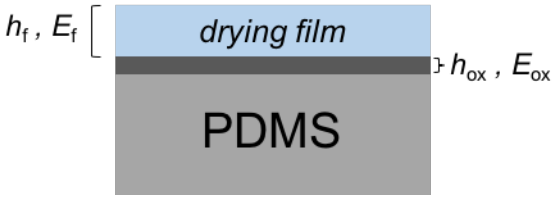

FIGURE 7.7: Schematic of the trilayer structure resulting from solution deposition (and planar film formation) on oxidised PDMS.

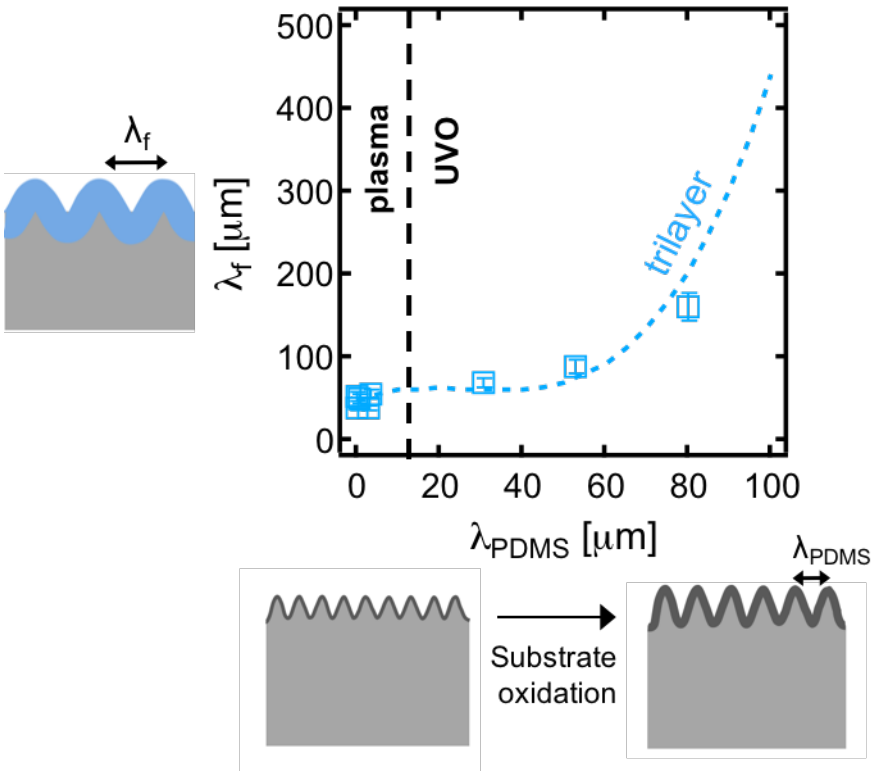

FIGURE 7.8: Wrinkling wavelength λ_f of films with $c_{0,glycerol} = 2$ wt % dried for $t_{drying} = 12$ min, as a function of substrate oxidation, expressed in terms of the wrinkling wavelength of neat oxidised PDMS under compression λ_{PDMS}. A plasma exposure time $t_{exp} = 2$ min yields $\lambda_{PDMS} = 0.14$ μm, while UVO exposures reach tens of micrometers. The dashed line represents the λ_f calculated by using the trilayer model of equations 7.1-7.3.

$$\bar{E}_{eff}/4 = \bar{E}_f \left[\left(1 - \frac{k}{2}\right)^3 - \left(\phi_{ox} - \frac{k}{2}\right)^3 \right] + \bar{E}_{ox} \left[\left(\frac{k}{2}\right)^3 + \left(\phi_{ox} - \frac{k}{2}\right)^3 \right] \quad (7.3)$$

and ϕ_{ox} is given by $\phi_{ox} = h_{ox}/(h_{ox} + h_f)$ whilst k can be expressed as $k = \frac{1+\phi_{ox}^2(\bar{E}_{ox}/\bar{E}_f - 1)}{1+\phi_{ox}(\bar{E}_{ox}/\bar{E}_f - 1)}$

In an attempt to assess the effect of the glassy oxide layer on the drying film

wrinkling, we performed a series of experiments, where h_{ox} was varied. Specifically, neat PDMS prestretched by 20 %, was oxidised using air plasma (MHz, $p = 7.16$ W, $P = 1$ mbar) and UV-ozonolysis for variable doses. As known from the results in the previous Chapters, simple air plasma exposure results in wrinkling with characteristic wavelengths from ≈ 100 nm to ≈ 4 μm and A within 10 nm and 1μm; UVO leads to larger patterns, with λ of the order of tens of microns. We measured λ_{PDMS} and A_{PDMS} for all the oxidised samples upon strain release, and utilised the characteristic dimensions to infer the thickness of the oxide layer using the simple bilayer model (comprising two equations with two unknowns, namely h_{ox} and $\bar{E}_{ox}$).

Thereafter, ternary films with $c_{0,glycerol} = 2$ wt % were cast onto identical, pre-strained, oxidised layers and the resulting wrinkling profile measured at drying time $t_{drying} = 12$ min. Figure 7.8 shows the wrinkling wavelength of the drying film, λ_f as a function of substrate oxidation expressed in terms of the oxidised PDMS wavelength, λ_{PDMS}. The data were fitted using the trilayer model, where h_{ox} was expressed in terms of λ_{PDMS}: the goodness of the fit corroborates the validity of the experimental observations. From the data it is clear that when $\lambda_{PDMS} \ll \lambda_f$, PDMS wrinkling has a negligible impact on film wrinkling. However, the effect of substrate wrinkling becomes more important as the extent of PDMS oxidation increases, in particular within the UVO range where $\lambda_{PDMS} \approx \lambda_f$. This observation suggests that a bilayer model might be appropriate when oxidation causes $\lambda_{PDMS} \ll \lambda_f$, as in short ($t_{exp} = 2$ min) plasma exposures, while otherwise a trilayer model should be needed.

This hypothesis was proven by calculating the film Young's modulus considering the existence of the intermediate layer in Figure 7.9a. The explicit trilayer results agree with each other over the entire range of substrate oxidation, confirming the validity of the model. The film elastic modulus was also inferred from λ_f using a bilayer model, at the optimal conditions of substrate oxidation chosen in the experiments ($t_{exp} = 2$ min). Evidently, both the trilayer and bilayer model results are in agreement when $\lambda_{PDMS} \ll \lambda_f$. By contrast, a bilayer assumption in the presence of a thick oxide (intermediate) layer h_{ox} yields inconsistent results

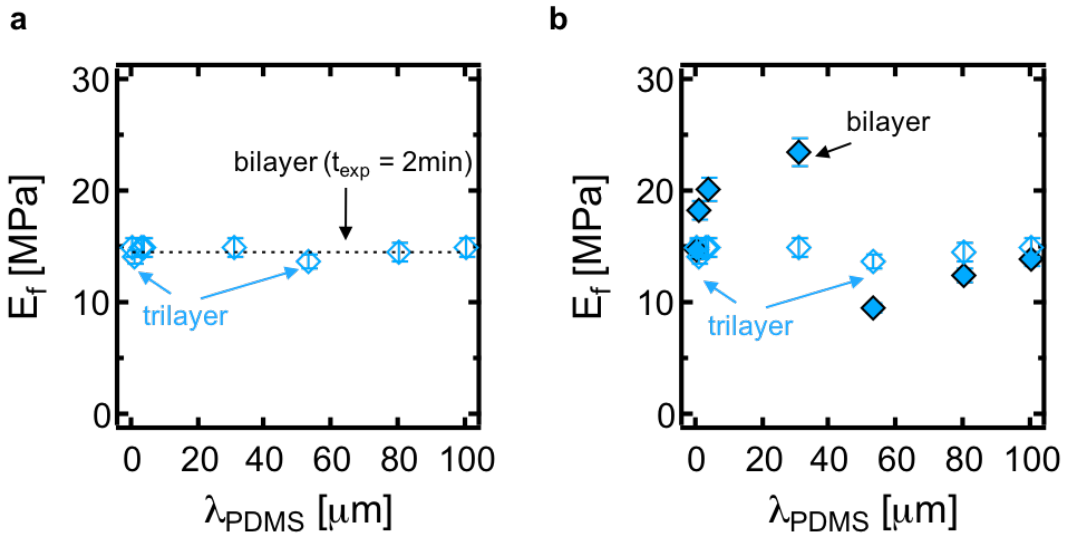

FIGURE 7.9: a) Elastic modulus of films with $c_{0,glycerol} = 2$ wt %, dried for $t_{drying} = 12$ min on PDMS substrates oxidised to various extents, evaluated using the trilayer model of equations 7.1-7.3. The dashed line is obtained from the bilayer model applied to films dried on PDMS substrates treated with plasma oxidation for $t_{exp} = 2$ min. b) Comparison between the values of E_f obtained by applying the bilayer model over the entire range of substrate oxidation, and those inferred with the trilayer model.

for the film's modulus under identical drying conditions (Figure 7.9b). For the remainder of the data analysis we thus employed a bilayer model, since it provides indistinguishable results for 2 min plasma exposed PDMS substrates.

7.4.2 Evolution of drying film mechanical properties: effect of drying time

Considering the above findings, we next compute the evolution of the Young's modulus of a $c_{0,glycerol} = 2$ wt % film as a function of drying time. The films were left drying on oxidised, prestretched ($\epsilon_{prestrain} \approx 20\%$) PDMS substrates: strain was released from the bilayers at different stages of drying (within the sinusoidal wrinkling regime). By means of surface profilometry we quantified λ_f and A_f of the wrinkling profile, which are plotted in Figure 7.10a and 7.10b as a function of the drying time. The measurements were repeated 30 minutes and 1 hour after the strain release and led to negligible variations in λ_f and A_f. From the wavelength and amplitude measurements, the aspect ratio A_f/λ_f was evaluated,

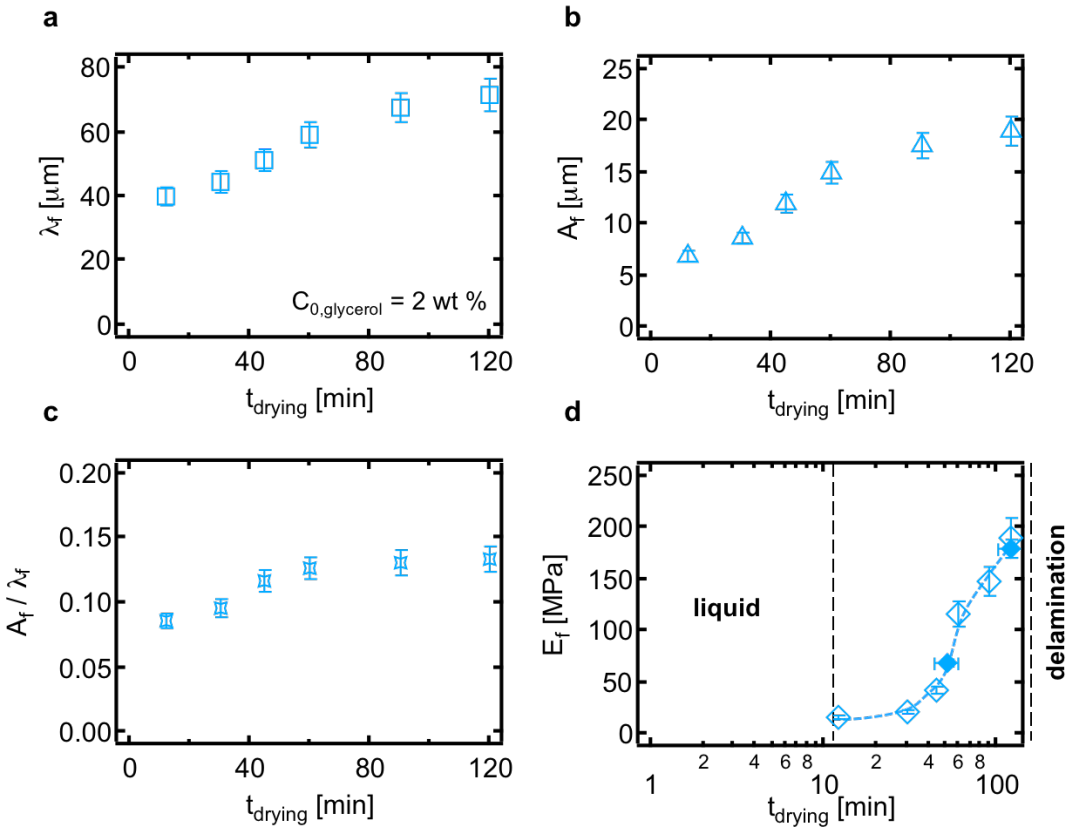

FIGURE 7.10: Evolution of drying film properties as a function of time ($c_{0,glycerol}$ = 2 wt %, T = 25 °C, and RH = 25%). Wrinkling wavelength (a), λ_f, and (b) amplitude, A_f, observed upon strain release at different drying times and (c) corresponding aspect ratio, A_f/λ_f. d) Dynamic evolution of film elastic modulus during drying, obtained from wrinkling experiments (⋄) using the bilayer model, corroborated by AFM nanoindentation (⧫).

whose temporal evolution is shown in Figure 7.10c. The reason why we computed the aspect ratio is that, recalling the bilayer model [43, 46, 47], we find that

$$A_f/\lambda_f = \left(\epsilon - \left(3\bar{E}_s/\bar{E}_f\right)^{2/3}/4\right)^{1/2}/\pi \tag{7.4}$$

The only unknown in the former expression is $\bar{E}_f$: therefore by having the dynamical evolution of the aspect ratio, we can trivially infer how the elastic modulus of the film changes as a function of drying time. This is plotted in Figure 7.10d, where a logarithmic scale is chosen for a direct comparison with the mass loss, shown in Figure 7.12a. As discussed previously, at short times no patterns are observed upon strain release thus impeding the calculation of the elastic modulus. After 12 min for this system, when the mass loss slows, an elastic modulus can

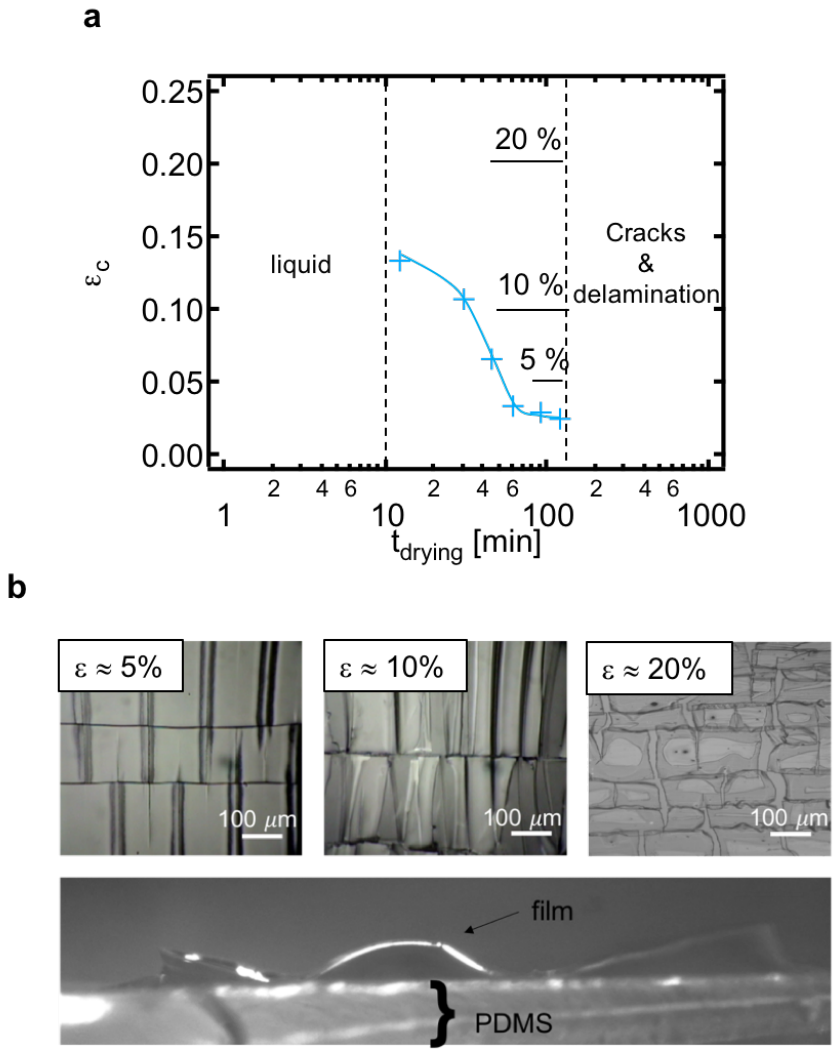

FIGURE 7.11: Critical strain for wrinkling as a function of drying time, for a film with $c_{0,glycerol}$ = 2 wt % at 25 °C and 25 % RH. The value of strain $\epsilon_{prestrain}$ = 20 % chosen in the experiments is above the critical strain at all relevant drying times. b) Optical microscopy images of films with $c_{0,glycerol}$ = 2 wt % allowed to dry for 3 hours, with a prestrain of 5, 10 and 20%. At such long drying times, even a lower value of strain (e.g. 5 %) could not prevent delamination and cracking, hindering mechanical measurement via wrinkling.

be measured and is found to increase rapidly upon further dehydration. This upturn corresponds to a significant increase in viscosity, in agreement with previous calorimetry experiments on these hydroxyaluminium solutions [184]. As the film stiffens, approaching the glass transition ($t_{drying} > 2$ h), wrinkling is no longer an effective approach to determine its mechanical properties. Instead, cracking and delamination modes were found to prevail, as seen in the map in Figure 7.4.

In an attempt to minimise these effects and thus extending the applicability of the method, we tried to reduce the strain applied for films dried at long times. In the previous paragraphs, we justified the choice of $\epsilon_{prestrain} \approx 20$ % as it exceeded the critical strain required to induce wrinkling during the first stages of drying. However, as anticipated, we expect ϵ_c to decrease as the film stiffens. Based on the values of the elastic modulus of the film at different drying times, we thus computed the evolution of the critical strain, shown in Figure 7.11a. The results corroborate the hypothesis, showing that at long drying times a $\epsilon_{prestrain}$ lower than 5 % is sufficient to trigger the wrinkling instability. Based on these findings, we decided to perform wrinkling experiments on dry films ($t_{drying} > 3$ hours), by employing lower values of $\epsilon_{prestrain}$ (≈ 5 and 10 %). Unfortunately, cracking and delamination were observed also at these conditions, as visible in Figure 7.11b, with an increasing spatial density, with increasing strain. Optical microscopy images of the top and cross-sectional views of the surfaces show the combination of cracks and (orthogonal) delamination. We therefore confirm that reducing $\epsilon_{prestrain}$ is not a viable approach to extending the range of application of this time-resolved wrinkling approach. For this system, under the environmental conditions studied, the window of applicability of the wrinkling approach is thus approximately [12-120 min]. To check the validity of the method within this range, we also employed AFM nanoindentation on the dried films to measure their elastic modulus. The values acquired through the different techniques were found to agree. However, one has to point out that nanoindentation measurements are limited by the characteristics of the AFM tips and suffer from substrate convolution for very thin films: moreover, they require long measurement times and model-sensitive data analysis. By contrast, the wrinkling method is simpler, sufficiently accurate, and versatile for these measurements.

From the elastic modulus obtained from our wrinkling approach, we then utilised the bilayer equations [43, 46, 47] to estimate the film thickness over time, reported in Figure 7.12b. The wrinkling values (data points) were found to be in good agreement with the calculated profile from mass loss measurements, further corroborating the reliability of the proposed experimental method.

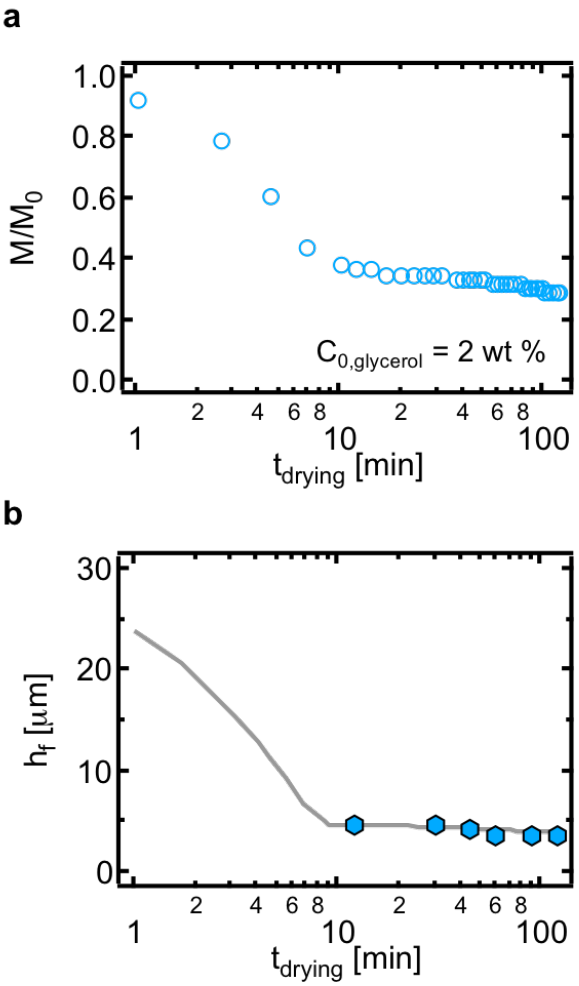

FIGURE 7.12: a) Normalised mass loss as a function of time for a film with $c_{0,glycerol} = 2$ wt %, dried at $T = 25$ °C and $RH = 25$ %. b) Corresponding height profile from gravimetric data (gray line) and values obtained from wrinkling experiments using the bilayer model.

Both the mechanical properties and thickness evolution were inferred from surface morphologies acquired on N different samples, where wrinkling was induced at different stages of drying. As discussed previously, since wrinkling is a reversible process, the N measurements can also be performed on the same sample, by periodically releasing the stress and then stretching back to the same initial value. The approach was implemented at ambient temperature and relative humidity (recorded at $T = 21$ °C and $RH = 45$ %) as the sample was kept under the optical microscope throughout the drying process. Figure 7.13 reports the pattern wavelength within the sinusoidal regime, measured upon strain release at different

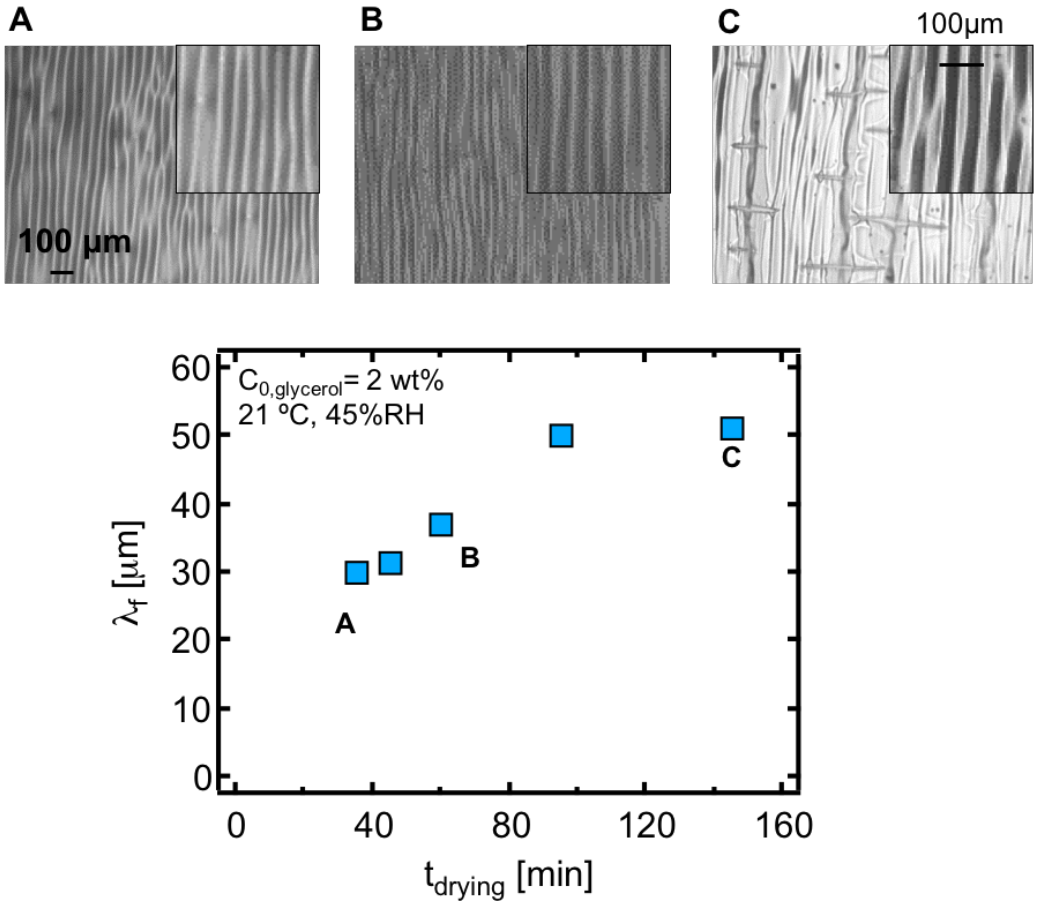

FIGURE 7.13: Wrinkling wavelength observed on a single film as a function of drying time, for a $c_{0,glycerol} = 2$ wt % film at 21 °C and 45 % RH. The data refer to the same sample, stretched back to the same initial amount of 20% after each wrinkling measurement. The figure also shows optical microscope images of the wrinkled film at different stages of drying

drying times. First of all, one can notice that the different conditions of temperature and relative humidity have an impact on the drying kinetics, with the sinusoidal regime extending now from 40 to 150 minutes. However, more importantly, the optical microscopy images of the surface at different stages of drying confirm that the formation of cracks is promoted by multiple stretching and releasing. As expected, more accurate measurements are obtained by employing multiple samples.

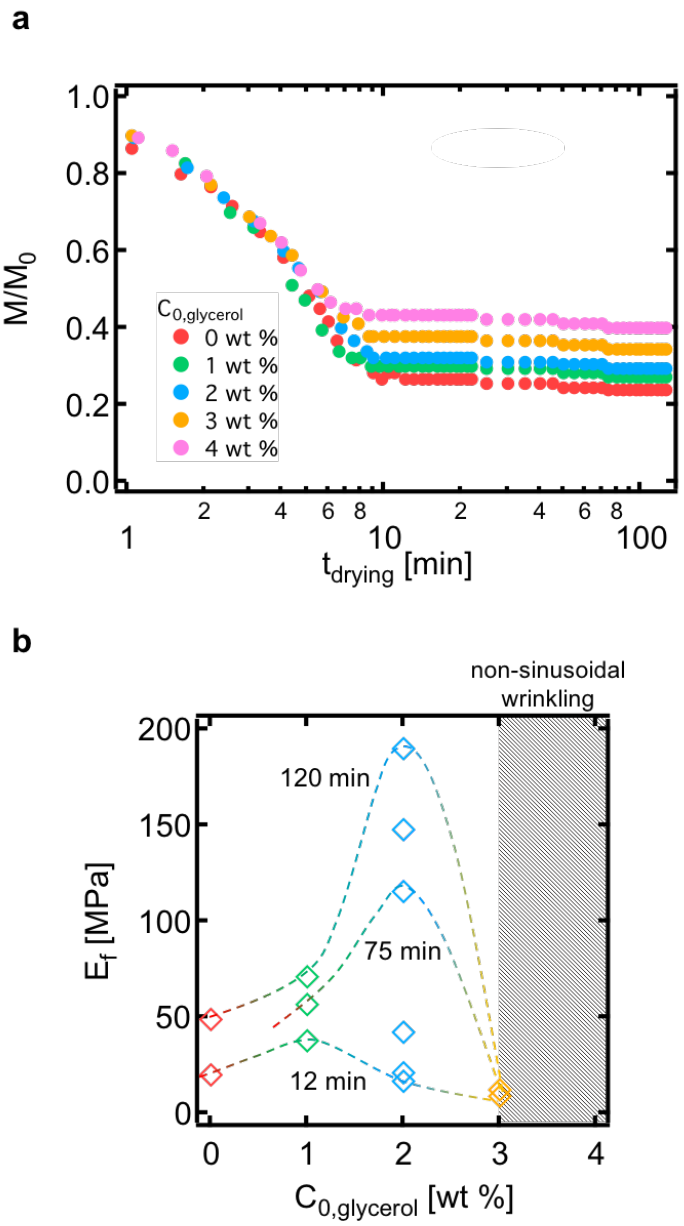

FIGURE 7.14: a) Normalised film mass loss for different initial solution compositions (0 wt % $< c_{0,glycerol} <$ 4 wt %), upon drying at 25 °C and 25% RH. b) Film elastic modulus calculated using a bilayer model as a function of initial solution composition in terms of glycerol content, at different drying times. The lines serve for guidance only.

7.4.3 Dependence of film modulus on solution concentration

We next computed the evolution of the elastic modulus for films of varying initial glycerol compositions ($c_{0,glycerol}$) during drying. The solutions were deposited on prestretched ($\epsilon_{prestrain} \approx 20$ %), oxidised PDMS substrates and wrinkling was induced by relasing the strain at selected drying times. The mass of the film was recorded as a function of time and is shown in Figure 7.14a for different $c_{0,glycerol}$. The normalised mass loss profiles show that increasing the glycerol content in the solution results in an increase in the final film mass, as more water is retained being glycerol an effective humectant [184].

Within the sinusoidal regime, wrinkling experiments allowed for the determination of the elastic modulus of the film, shown in Figure 7.14b as a function of $c_{0,glycerol}$ for films dried for 12, 75, and 120 min. As seen on the graph, the trend was found to be markedly nonmonotonic with glycerol concentration. One might have expected the elastic modulus to decrease with the addition of glycerol, suggested by the absence of pattern formation reported for $c_{0,glycerol}$ between 5 and 15 wt % for up to 40 % prestrain. However, small glycerol quantities ($c_{0,glycerol} \leq 4$ wt %) have been reported to act as an antiplasticizer [184, 188–191] and actually increase the film modulus, before the latter eventually decreases as the film becomes liquid at high humectant concentrations (for $c_{0,glycerol} > 4$ %). The competitive binding between glycerol, water, and ACH was shown to result in the replacement of water molecules bound to the salt's hydroxyl groups by glycerol, which enhances film drying. Generally, as the film loses more water, its elastic modulus increases, as can be observed in the curve at $t_{drying} = 120$ min which is above the 12 min curve. The reliability of the experiments is confirmed by previous calorimetric measurements, which agree with the observed trend of the elastic modulus as a function of composition [184].

Chapter 8

Conclusions and Future Work

8.1 Conclusions

We started this study seeking to develop soft matter patterning methods, accessing dimensions ranging from the macroscale down to the nanoscale. Moreover we wanted this method to be simple and cost-effective, thus applicable on large scales. Conventional techniques, including lithography, do not fully comply with the requirements, especially for nanoscale patterning, in terms of complexity and costs.

Guided by the 'simplicity' criterion, we examined wrinkling as a way to fabricate surfaces with distinct morphologies. Indeed having a bi- (multi-) layer, comprising a thin film on top of a thick and softer substrate, pattern formation can be readily induced through compression. Provided the compressive force is applied uniaxially and exceeds a critical value, one dimensional sinusoidal features arise, eventually replaced by more complex morphologies when increasing the compression, due to stress localisation effects. The characteristic wavelength and amplitude of the sinusoidal patterns are proportional to the thickness and elastic modulus of the film, and decrease with substrate stiffness. This suggested that, by appropriately selecting the bilayer, we could *theoretically* access a wide range of pattern morphologies, from the nano to the macroscale.

Practically, we had to devise different techniques for bilayer formation. The technique as well had to be chosen on the same basis of the patterning method: not only had it to be inexpensive and simple, but also effective at obtaining bilayers with films as thin as few nm. Amongst the various options, substrate vitrification appeared as the most suitable, ensuring perfect adhesion between the layers and overcoming the difficulties in handling very thin films. We therefore selected polydimethylsiloxane as the substrate of choice and studied wrinkling by mechanical compression of the bilayers forming upon substrate oxidation by means of air plasma or UV-ozonolysis.

We first investigated PDMS oxidation via plasma and the resulting wrinkling profiles attainable by uniaxial strain. An unprecedented range of experimental processing variables was considered: the exposure time, power, gas pressure and O_2 content, and plasma induction frequency (kHz and MHz). By independently assessing the effect of each parameter on wrinkling of the corresponding bilayers, we found that the pattern dimensions decrease with increasing pressure, decreasing exposure time, induction power and gas oxygen content, and that MHz plasma is more effective for patterning in the sub-μm range. Equipped with this knowledge, we were able to obtain sinusoidal patterns with $\lambda_{min} \approx 100$ nm at the modest strain of 20 %, corresponding to a 30% reduction with respect to the previously established limit of 140 nm (achieved however by employing an unpractical compression of 200 % [93]). Moreover, we found that under all the conditions studied the PDMS surface oxidation, densification and glass formation induced by plasma is well described by a planar frontal process, in which the glassy skin thickness h grows logarithmically with time (or dose D = power x time), and more generally with dose/pressure. The minimal model was found to capture the three stages observed via the wrinkling experiments at variable plasma doses , namely *induction*, *film formation* and *propagation*. Our hypothesis was that during the *film propagation* stage, the skin modulus remains unchanged and only the film thickness h evolves (logarithmically) during exposure. By contrast in the early stages of plasma exposure (*film formation*), the PDMS surface simultaneously increases in the modulus and thickness. This means that at low plasma exposure dose, the

bilayer modulus contrast is insufficient, and no wrinkling is observed. We refer to this as the *induction* stage.

Inspired by these results, we wanted to further lower the pattern dimensions achievable via mechanical wrinkling of plasma oxidised PDMS. Therefore we first sought to understand in more detail the mechanism of film formation and densification. X-ray and neutron reflectivity experiments revealed that a critical plasma exposure time t_c must be overcome in order to yield glassy films with finite thickness and sufficient conversion. The value of t_c was found to coincide with the time corresponding to the minimum wrinkling wavelength observed, marking the transition between the induction and formation regimes. These findings on one hand corroborated the validity of the minimal model chosen to describe the oxidation; on the other hand, however, they proved we could not tune the film's thickness or elastic modulus to access sub-100 nm patterns. If we could not soften the film, we therefore opted to stiffen the substrate. At first we tried simply varying the curing conditions for the PDMS, and obtained a reduction of $\approx$ 20 % in the minimum wavelength achievable. Inspired by this, we sought alternative ways to obtain a more markable increase in the substrate modulus. We thus considered UVO oxidation of PDMS. In agreement with previous literature studies, we found that for short exposure times, UVO results in the formation of a thick oxide layer, on PDMS, whose elastic modulus is two orders of magnitude lower compared to the glassy film formed upon plasma oxidation. Moreover, we found that the strain of 20 % conventionally employed is lower than the critical value required to trigger the wrinkling instability of the UVO-oxide layer. The latter could therefore act as the substrate and be further oxidised by means of air plasma to create the bilayer on which inducing wrinkling. By doing this, we succeeded in obtaining single frequency sinusoidal patterns with $\lambda_{min} \approx 45$ nm, thus accessing the deep UV-range.

Having established wrinkling as a scalable method for patterning in the nm range, we examined larger morphologies. We focused on UVO oxidation, as we had previously demonstrated it leads to thicker and softer skins compared to air plasma, thus larger features. We performed a combination of reflectivity and wrinkling

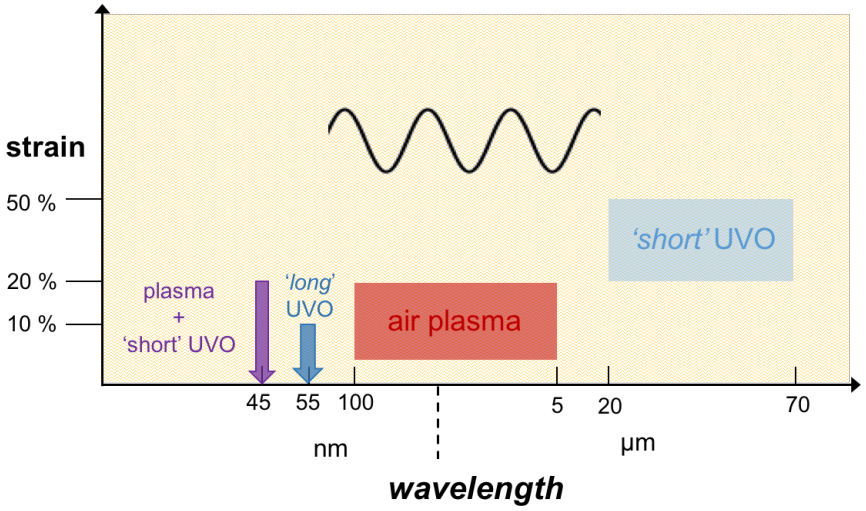

FIGURE 8.1: Strategies to obtain single frequency, sinusoidal wrinkles on oxidised PDMS bilayers. By employing different procedures and tuning the strain, we manage to pattern from the nm to the μm scale [152, 164, 168].

experiments on UVO oxidised PDMS bilayers, both confirming the existence of two regimes as a function of the exposure time. In the first stages of exposure, we assist to the formation of a bilayer, leading to wrinkles with $\lambda \sim$ tens of microns, when compressed to a high extent ($\approx$ 50 %). When prolonging the exposure an extra skin was found to form, resulting in trilayer laminates. By applying strain to these structures we could observe double frequency, sinusoidal patterns comprising one generation of wrinkles in the μm range surmounted by a second generation of patterns in the nm range. Interestingly we found that the properties of the three layers were such that, by lowering the strain, we could suppress the wrinkling mechanism between the intermediate layer and the substrate, thus obtaining surfaces with single frequency, sinusoidal features with $\lambda_{min} \approx 55$ nm. The conclusion was that, excitingly, a single UVO exposure is effective at creating multi-layers which, upon compression, can give both sinusoidal patterns ranging from 55 nm up to tens of microns, and hierarchical features where the two scales are nested in a single morphology. The experiments therefore established wrinkling as a cheap and simple method to impress patterns from the nano to the macro scale. Indeed by employing air plasma, UVO, or a combination of the two to oxidise PDMS substrates, we succeeded at creating bilayers which, appropriately excited, allow for single frequency, sinusoidal patterns to be observed, with

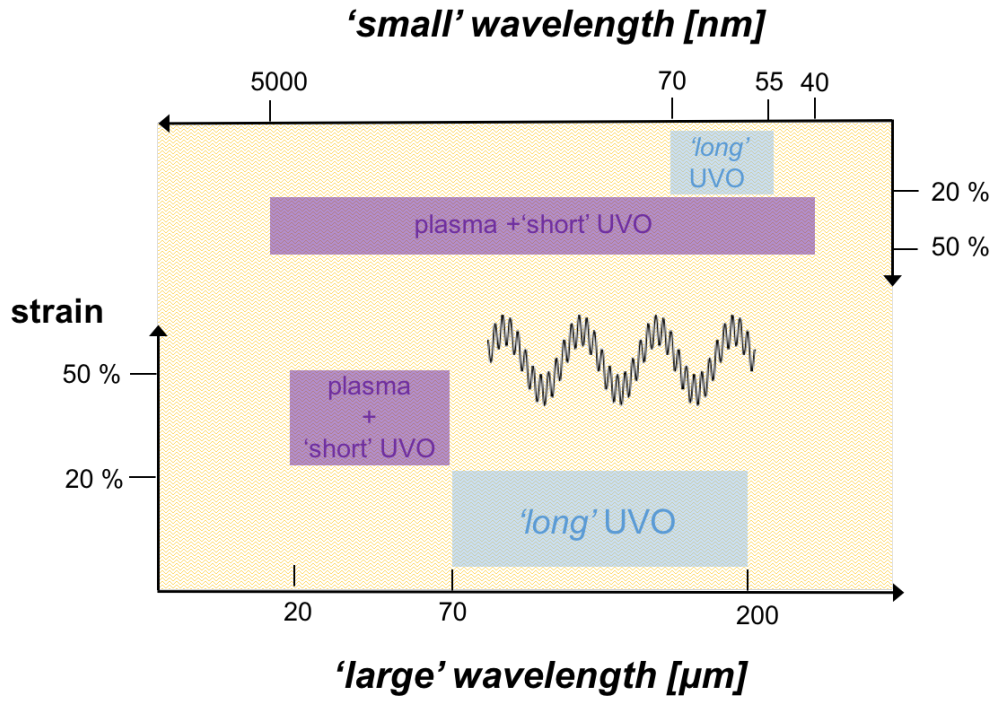

FIGURE 8.2: Strategies to obtain double frequency, sinusoidal wrinkles on oxidised PDMS bilayers. Moving from a 'single-step' to a 'double-step' approach we can access a wide range of pattern dimensions, tuning independently the two generations of wrinkles [168].

characteristic wavelengths ranging between $\approx$ 45 nm to $\approx$ 60 μm (Figure 8.1).

We then decided to further explore the capabilities of this patterning method and thus moved from single to double frequency sinusoidal features. We had previously observed these morphologies on multi-layers resulting from prolonged UVO exposure of PDMS. However we found that with a 'single step' method, the layers' thicknesses grow simultaneously thus we could not independently tune the dimensions of the two generations of patterns. Trilayer laminates were fabricated implying a 'two-step' procedure, comprising short UVO exposure, followed by either air plasma or film deposition. Upon compression hierarchical patterns arised, whose dimensions could be varied within a wide range just by selectively changing the extent of the two steps (Figure 8.2). Selected contact angle experiments carried on these patterned surfaces demonstrated that the presence of the second generation of wrinkles has an impact on the wetting properties, with increasing contact angle going from nm to few μm scale secondary features. These wrinkling

experiments allowed to establish the exact sequence of thicknesses and elastic moduli of the trilayers resulting in double frequency sinusoidal features. Moreover, we demonstrated that a simple model is sufficient to describe this unique wrinkling mechanism.

After having exploited wrinkling as a patterning method, we employed wrinkling as a tool to infer properties about selected films, building upon previous experimental reports. However, we were the first in applying the method in a dynamic way, in order to evaluate how thin, drying films, stiffen upon water loss and film formation. The method yielded accurate results, being simpler and more cost-effective than conventional techniques for elastic modulus determination.

All the results presented highlighted how a simple process like wrinkling can be effective both as a patterning and a measurement tool.

8.2 Perspective

Numerous possibilities remain open for future research on wrinkling. Great opportunities include fabricating more complex pattern morphologies, in a controlled and systematic way, for functional surfaces. Different strain fields, other than uniaxial, can be explored as well as processes comprising a defined sequence of multiple strain application and film formation. Chiche *et al.* [92], for example, reported on the possibility of fabricating surfaces with 'spikes' by replicating surfaces with sinusoidal features oriented in the y direction and then stretching and inducing wrinkling in the orthogonal direction. Following their procedure we succeeded in fabricating these morphologies, as shown by a representative profilometer image in Figure 8.3. However, controlled experiments as well as a mathematical description of this kind of pattern formation are still missing for both the sequential and simultaneous application of multi-axial strains. Surfaces with all these ranges of features could be of great interest for wetting and spreading of liquids, knowing the effect roughness has shown to have in these phenomena [192–196], and we expect

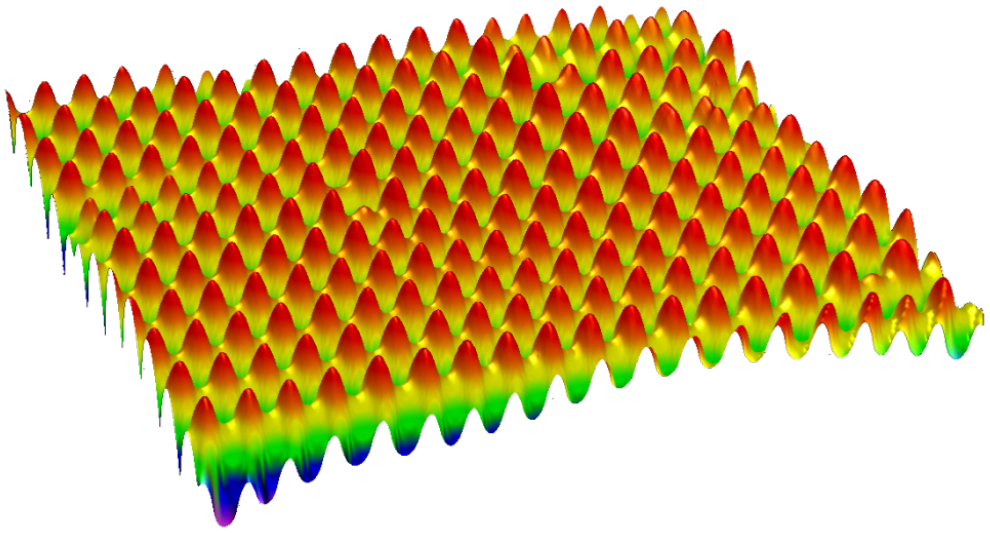

FIGURE 8.3: Surface morphology of a 'spiked' wrinkled sample fabricated with the procedure described by [92]. A PDMS slab was prestretched and oxidised via UVO to obtain single frequency sinusoidal patterns. The sample was then replicated and stretched in the direction parallel to the wrinkles, then oxidised again via UVO. The surface upon strain release was characterised by means of stylus profilometry.

a wide and unique range of responses. Moreover one could build on previous work [197–199] and assess how surface morphology impacts the adhesion properties.

Another significant path to explore would be related to the application of these structures. An interesting field includes biology and tissue engineering. Concerning this, at the moment we have an ongoing collaboration with the Institut Curie in France. The aim of the project is to use wrinkled surfaces to study the effects of the substrate curvature on the binding of proteins, septins, involved in many cellular processes, including cytokinesis and compartimentalization of cilium cells and spematozoids [200]. These proteins could be able to recognise the substrate curvature, as they are normally found in specific regions of cells (characterised by a radius of curvature in the μm range) [201]. To assess this, we utilised the PDMS patterned surfaces and transferred the wrinkling patterns onto photopolymerisable resins, thereby broadening immensely the choice of materials, surface energy and biocompatibility available. The surfaces were covered with lipid vesicles, leading to the formation of a bilayer subsequently coated with septins: the interaction

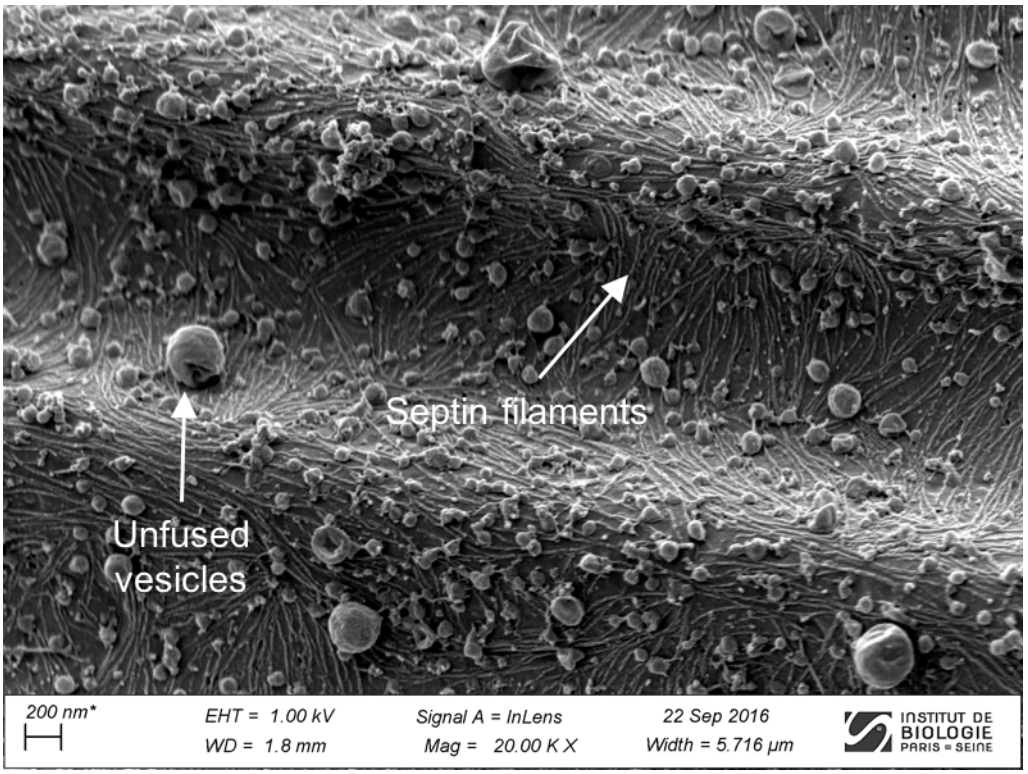

FIGURE 8.4: Preliminary results on binding of septins on lipid bilayers deposited onto wrinkled substrates. The project is a collaboration with the Institut Curie, Paris.

between the proteins and the wrinkled lipid bilayer was quantified by means of confocal and SEM microscopy. As we demonstrated the ability of fabricating patterns with a wide range of dimensions, by varying the morphology we are capable of assessing the impact of a significant number of positive and negative curvatures employing a simple, yet useful in vitro system. Some preliminary results are shown in Figure 8.4 which presents a SEM image of a selected sample, showing the septin filaments laying on the wrinkles. From the image one can clearly see how the filaments align differently in the regions of positive and negative curvature (hills and valleys).

Aside from studying protein binding, these wrinkled substrates could potentially be utilised for high throughput cell screening [114, 202, 203]. Moreover they could serve in building a tuneable and controlled microenvironment, allowing for stem cell differentiation studies [204, 205].

Another interesting application would exploit the interesting characteristic of patterned surfaces in affecting drag during flow. There is a well established method in our research group for fabricating microfluidic devices using photolithography [11]. These devices have been utilised to study complex fluids under flow, with the aid of scattering techniques [206, 207]. It would be worth incorporating wrinkles in these devices, thus creating microchannels with a defined internal roughness. This would allow for high throughput studies, aiming at evaluating how the roughness affects the pressure drop for non-Newtonian fluids under flow [208–211].

These are only some of the examples of what could be done with wrinkled surfaces. The possibility of transferring the patterns to a wide range of different materials incredibly extends the range of applications, which could go from the fabrication of optical components to solar cells with improved efficiency and many more, yet based on a process which is extremely simple, versatile and powerful.

List of Figures

List of Tables

List of Publications

1. **M. Nania**, F. Foglia, O.K. Matar and J.T. Cabral. Origin of multiple frequency wrinkling on elastomer sandwich bilayers. *Nano Letters*, To submit, 2017.

2. **M. Nania**, F. Foglia, O.K. Matar and J.T. Cabral. Sub-100 nm wrinkling of polydimethylsiloxane by double frontal oxidation. *Nanoscale*, 9 (5): 2030-2037, 2017.

3. **M. Nania***, G.L. Ferretti *[1], O.K. Matar and J.T. Cabral. Wrinkling Measurement of the Mechanical Properties of Drying Salt Thin Films. *Langmuir*, 32 (9): 2199-2207, 2016.

4. **M. Nania**, O.K. Matar and J.T. Cabral. Frontal vitrification of PDMS using air plasma and consequences for surface wrinkling. *Soft Matter*, 11 (15): 3067-3075, 2015.

***

5. F. Foglia, S. Karan, **M. Nania**, Z. Jiang, A. Porter, R. Barker, A.G. Livingston and J.T. Cabral. Neutron reflectivity and performance of polyamide nanofilms for water desalination. *Advanced Functional Materials*, Under review.

6. F. E. Bedoya-Lora, A. Hankin, I. Holmes-Gentle, A. Regoutz, D. J. Payne, **M. Nania**, J. T. Cabral and G. H. Kelsall. Effects of annealing Sn^{IV}-doped -Fe_2O_3 at 400-500 °C on photo-anode performance. *Electrochimica Acta*, Under review.

[1] *equal contribution

7. A. S. Poulos, **M. Nania**, P. Lapham, R. M. Miller, A.J. Smith, H. Tantawy, J. Caragay, J. Gummel, O. Ces, E. S. J. Robles, and J. T. Cabral. Microfluidic SAXS study of lamellar and multilamellar vesicle phases of linear sodium alkylbenzene- sulfonate surfactant with intrinsic isomeric distribution. *Langmuir*, 32 (23): 5852-5861, 2016.

Bibliography

[1] T. Shimoda, K. Morii, S. Seki, and H. Kiguchi. Inkjet printing of light-emitting polymer displays. *MRS Bulletin*, 28(11):821–827, 2011.

[2] C. T. Black, R. Ruiz, G. Breyta, J. Y. Cheng, M. E. Colburn, K. W. Guarini, H. C. Kim, and Y. Zhang. Polymer self assembly in semiconductor microelectronics. *IBM Journal of Research and Development*, 51(5):605–633, 2007.

[3] Tommie W. Kelley, Paul F. Baude, Chris Gerlach, David E. Ender, Dawn Muyres, Michael A. Haase, Dennis E. Vogel, and Steven D. Theiss. Recent progress in organic electronics::materials, devices, and processes. *Chemistry of Materials*, 16(23):4413–4422, 2004.

[4] Sami Valkama, Harri Kosonen, Janne Ruokolainen, Tomi Haatainen, Mika Torkkeli, Ritva Serimaa, Gerrit ten Brinke, and Olli Ikkala. Self-assembled polymeric solid films with temperature-induced large and reversible photonic-bandgap switching. *Nature Materials*, 3(12):872–876, 2004.

[5] M. Campbell, D. N. Sharp, M. T. Harrison, R. G. Denning, and A. J. Turberfield. Fabrication of photonic crystals for the visible spectrum by holographic lithography. *Nature*, 404(6773):53–56, 2000.

[6] Ralf Seemann, Martin Brinkmann, Edward J. Kramer, Frederick F. Lange, and Reinhard Lipowsky. Wetting morphologies at microstructured surfaces. *Proceedings of the National Academy of Sciences*, 102(6):1848–1852, 2005.

[7] Alongkorn Pimpin and Werayut Srituravanich. Review on micro- and nanolithography techniques and their applications. *Engineering Journal*, 16(1): 37–56, 2011.

[8] Dong Qin, Younan Xia, and George M Whitesides. Soft lithography for micro- and nanoscale patterning. *Nature Protocols*, 5:491–502, 2010.

[9] Zhihong Nie and Eugenia Kumacheva. Patterning surfaces with functional polymers. *Nature Materials*, 7(4):277–290, 2008.

[10] Alessandra Vitale, Marzia Quaglio, Matteo Cocuzza, Candido Fabrizio Pirri, and Roberta Bongiovanni. Photopolymerization of a perfluoropolyether oligomer and photolithographic processes for the fabrication of microfluidic devices. *European Polymer Journal*, 48(6):1118 – 1126, 2012.

[11] J. T. Cabral, Steven D. Hudson, Christopher Harrison, and Jack F. Douglas. Frontal photopolymerization for microfluidic applications. *Langmuir*, 20(23): 10020–10029, 2004.

[12] Byron D. Gates, Qiaobing Xu, Michael Stewart, Declan Ryan, C. Grant Willson, and George M. Whitesides. New approaches to nanofabrication: Molding, printing, and other techniques. *Chemical Reviews*, 105(4):1171–1196, 2005.

[13] F. H. Dill, W. P. Hornberger, P. S. Hauge, and J. M. Shaw. Characterization of positive photoresist. *IEEE Transactions on Electron Devices*, 22(7):445–452, 1975.

[14] J.-P. Fouassier. *Photoinitiation, photopolymerization and photocuring*. Hanser Publishers, 1995.

[15] Alessandra Vitale, Matthew G. Hennessy, Omar K. Matar, and João T. Cabral. A unified approach for patterning via frontal photopolymerization. *Advanced Materials*, 27(40):6118–6124, 2015.

[16] Alessandra Vitale, Matthew G. Hennessy, Omar K. Matar, and João T. Cabral. Interfacial profile and propagation of frontal photopolymerization waves. *Macromolecules*, 48(1):198–205, 2015.

[17] Younan Xia and George M. Whitesides. Soft lithography. *Angewandte Chemie International Edition*, 37(5):550–575, 1998.

[18] Daniel P. Sanders. Advances in patterning materials for 193 nm immersion lithography. *Chemical Reviews*, 110(1):321–360, 2010.

[19] Christian Wagner and Noreen Harned. Euv lithography: Lithography gets extreme. *Nature Photonics*, 4(1):24–26, 2010.

[20] L. W. Liebmann, S. M. Mansfield, A. K. Wong, M. A. Lavin, W. C. Leipold, and T. G. Dunham. Tcad development for lithography resolution enhancement. *IBM Journal of Research and Development*, 45(5):661–665, 2001.

[21] Matteo Altissimo. E-beam lithography for micro-/nanofabrication. *Biomicrofluidics*, 4(2):026503, 2010.

[22] J. A. M. Sondag-Huethorst, H. R. J. van Helleputte, and L. G. J. Fokkink. Generation of electrochemically deposited metal patterns by means of electron beam (nano)lithography of self-assembled monolayer resists. *Applied Physics Letters*, 64(3):285–287, 1994.

[23] S. D. Berger and J. M. Gibson. New approach to projection-electron lithography with demonstrated 0.1 micron linewidth. *Applied Physics Letters*, 57 (2):153, 1990.

[24] Joy Y. Cheng, Anne M. Mayes, and Caroline A. Ross. Nanostructure engineering by templated self-assembly of block copolymers. *Nature Materials*, 3(11):823–828, 11 2004.

[25] Sang Ouk Kim, Harun H. Solak, Mark P. Stoykovich, Nicola J. Ferrier, Juan J. de Pablo, and Paul F. Nealey. Epitaxial self-assembly of block copolymers on lithographically defined nanopatterned substrates. *Nature*, 424(6947):411–414, 2003.

[26] Mark P. Stoykovich, Marcus Müller, Sang Ouk Kim, Harun H. Solak, Erik W. Edwards, Juan J. de Pablo, and Paul F. Nealey. Directed assembly of block copolymer blends into nonregular device-oriented structures. *Science*, 308(5727):1442–1446, 2005.

[27] L. J. Guo. Nanoimprint lithography: Methods and material requirements. *Advanced Materials*, 19(4):495–513, 2007.

[28] Arjan P. Quist, Elisabeth Pavlovic, and Sven Oscarsson. Recent advances in microcontact printing. *Analytical and Bioanalytical Chemistry*, 381(3): 591–600, 2005.

[29] Richard D. Piner, Jin Zhu, Feng Xu, Seunghun Hong, and Chad A. Mirkin. "dip-pen" nanolithography. *Science*, 283(5402):661–663, 1999.

[30] E. Cerda and L. Mahadevan. Geometry and physics of wrinkling. *Phys. Rev. Lett.*, 90(7):074302(4), 2003.

[31] Roberto Toro. On the possible shapes of the brain. *Evolutionary Biology*, 39(4):600–612, 2012.

[32] Li Wen, James C Weaver, Patrick J M Thornycroft, and George V Lauder. Hydrodynamic function of biomimetic shark skin: effect of denticle pattern and spacing. *Bioinspiration and Biomimetics*, 10(6):066010, 2015.

[33] Hans J Ensikat, Petra Ditsche-Kuru, Christoph Neinhuis, and Wilhelm Barthlott. Superhydrophobicity in perfection: the outstanding properties of the lotus leaf. *Beilstein Journal of Nanotechnology*, 2:152–161, 2011.

[34] Marina Chicurel. Databasing the brain. *Nature*, 406:822–825, 2000.

[35] Xia Pu, Guangii Li, and Hanlu Huang. Preparation, anti-biofouling and drag-reduction properties of a biomimetic shark skin surface. *Biology Open*, 5(4):389–396, 2016.

[36] Philip Ball. Engineering shark skin and other solutions. *Nature*, 400(6744): 507–509, 1999.

[37] Gregory S. Watson, David W. Green, Lin Schwarzkopf, Xin Li, Bronwen W. Cribb, Sverre Myhra, and Jolanta A. Watson. A gecko skin micro/nano structure – a low adhesion, superhydrophobic, anti-wetting, self-cleaning, biocompatible, antibacterial surface. *Acta Biomaterialia*, 21:109 – 122, 2015.

[38] Mengnan Qu, Jinmei He, and Junyan Zhang. Superhydrophobicity, learn from the lotus leaf. In Amitava Mukherjee, editor, *Biomimetics Learning from Nature*, chapter 16. InTech, Rijeka, 2010.

[39] Edwin Nun, Markus Oles, and Bernhard Schleich. Lotus-effect® – surfaces. *Macromolecular Symposia*, 187(1):677–682, 2002.

[40] J. Groenewold. Wrinkling of plates coupled with soft elastic media. *Physica A: Statistical Mechanics and its applications*, 298(1):32–45, 2001.

[41] Jan Genzer and Jan Groenewold. Soft matter with hard skin: From skin wrinkles to templating and material characterization. *Soft Matter*, 2:310–323, 2006.

[42] Bo Li, Yan-Ping Cao, Xi-Qiao Feng, and Huajian Gao. Mechanics of morphological instabilities and surface wrinkling in soft materials: a review. *Soft Matter*, 8:5728–5745, 2012.

[43] H.G. Allen. *Analysis and design of structural sandwich panel.* Pergamon Press, New York, 1969.

[44] G. S. Gough, C. F. Elam, G. H. Tipper, and N. A. De Bruyne. The stabilisation of a thin sheet by a continuous supporting medium. *The Aeronautical Journal*, 44(349):12–43, 1940.

[45] Jun Young Chung, Adam J. Nolte, and Christopher M. Stafford. Surface wrinkling: A versatile platform for measuring thin-film properties. *Advanced Materials*, 23(3):349–368, 2011.

[46] A. L. Volynskii, S. Bazhenov, O. V. Lebedeva, and N. F. Bakeev. Mechanical buckling instability of thin coatings deposited on soft polymer substrates. *Journal of Materials Science*, 35(3):547–554, 2000.

[47] R. Huang. Kinetic wrinkling of an elastic film on a viscoelastic substrate. *Journal of the Mechanics and Physics of Solids*, 53(1):63 – 89, 2005.

[48] Z Suo R Huang. Wrinkling of a compressed elastic film on a viscous layer. *Journal of Applied Physics*, 91(3):1135–1142, 2002.

[49] M.A. Biot. Bending of an unfinite beam on an elastic foundation. *Journal of Applied Mechanics*, 4(1), 1937.

[50] Z.Y. Huang, W. Hong, and Z. Suo. Nonlinear analyses of wrinkles in a film bonded to a compliant substrate. *Journal of the Mechanics and Physics of Solids*, 53(9):2101 – 2118, 2005.

[51] B.A. Gilchrest. A review of skin ageing and its medical therapy. *British Journal of Dermatology*, 135(6):867–875, 1996.

[52] Qiming Wang and Xuanhe Zhao. A three-dimensional phase diagram of growth-induced surface instabilities. *Scientific Reports*, 5:8887 (1–10), 2015.

[53] Wei Hong, Xuanhe Zhao, and Zhigang Suo. Formation of creases on the surfaces of elastomers and gels. *Applied Physics Letters*, 95(11):11901, 2009.

[54] Yanping Cao and John W. Hutchinson. From wrinkles to creases in elastomers: the instability and imperfection-sensitivity of wrinkling. *Proceedings of the Royal Society of London A: Mathematical, Physical and Engineering Sciences*, 2011.

[55] M.B. Amar and P. Ciarletta. Swelling instability of surface-attached gels as a model of soft tissue growth under geometric constraints. *Journal of the Mechanics and Physics of Solids*, 58:935–954, 2010.

[56] S. Cai, D. Chen, Z. Suo, and R. Hayward. Creasing instability of elastomer films. *Soft Matter*, 8:1301–1304, 2012.

[57] Luka Pocivavsek, Robert Dellsy, Andrew Kern, Sebastián Johnson, Binhua Lin, Ka Yee C. Lee, and Enrique Cerda. Stress and fold localization in thin elastic membranes. *Science*, 320(5878):912–916, 2008.

[58] Jong Bok Kim, Pilnam Kim, Nicolas C. Pegard, Soong Ju Oh, Cherie R. Kagan, Jason W. Fleischer, Howard A. Stone, and Yueh-Lin Loo. Wrinkles and deep folds as photonic structures in photovoltaics. *Nature Photonics*, 6 (5):327–332, 2012.

[59] Fabian Brau, Pascal Damman, Haim Diamant, and Thomas A. Witten. Wrinkle to fold transition: influence of the substrate response. *Soft Matter*, 9:8177–8186, 2013.

[60] Y. Cao and John W. Hutchinson. Wrinkling phenomena in neo-hookean film/substrate bilayers. *Journal of Applied Mechanics*, 79:031019–1, 2012.

[61] Fabian Brau, Hugues Vandeparre, Abbas Sabbah, Christophe Poulard, Arezki Boudaoud, and Pascal Damman. Multiple-length-scale elastic instability mimics parametric resonance of nonlinear oscillators. *Nature Physics*, 7(1):56–60, 2011.

[62] Yuri Ebata, Andrew B Croll, and Alfred J Crosby. Wrinkling and strain localizations in polymer thin films. *Soft Matter*, 8(35):9086–9091, 2012.

[63] Changyong Cao, Hon Fai Chan, Jianfeng Zang, Kam W. Leong, and Xuanhe Zhao. Harnessing localized ridges for high-aspect-ratio hierarchical patterns with dynamic tunability and multifunctionality. *Advanced Materials*, 26: 1763–1770, 2014.

[64] Till JW Wagner and Dominic Vella. The 'sticky elastica': delamination blisters beyond small deformations. *Soft Matter*, 9(4):1025–1030, 2013.

[65] Haixia Mei, Chad M. Landis, and Rui Huang. Concomitant wrinkling and buckle-delamination of elastic thin films on compliant substrates. *Mechanics of Materials*, 43:627–642, 2011.

[66] Qiming Wang and Xuanhe Zhao. Phase diagrams of instabilities in compressed film-substrate systems. *Journal of Applied Mechanics*, 81:051004, 2013.

[67] J.W. Hutchinson and Z. Suo. Mixed mode cracking in layered materials. *Advances in Applied Mechanics*, 29, 1992.

[68] J.W Hutchinson and A.G Evans. Mechanics of materials: top-down approaches to fracture. *Acta Materialia*, 48(1):125–135, 2000.

[69] JY Chung, JH Lee, KL Beers, and CM. Stafford. Stiffness, strength, and ductility of nanoscale thin films and membranes: a combined wrinkling-cracking methodology. *Nano Letters*, 11(8):3361–3365, 2011.

[70] Christopher M. Stafford, Christopher Harrison, Kathryn L. Beers, Alamgir Karim, Eric J. Amis, Mark R. VanLandingham, Ho-Cheol Kim, Willi Volksen, Robert D. Miller, and Eva E. Simonyi. A buckling-based metrology for measuring the elastic moduli of polymeric thin films. *Nature Materials*, 3 (8):545–550, 2004.

[71] Santanu Karan, Zhiwei Jiang, and Andrew G. Livingston. Sub-10 nm polyamide nanofilms with ultrafast solvent transport for molecular separation. *Science*, 348(6241):1347–1351, 2015.

[72] Ned Bowden, Scott Brittain, Anthony G. Evans, John W. Hutchinson, and George M. Whitesides. Spontaneous formation of ordered structures in thin films of metals supported on an elastomeric polymer. *Nature*, 393(6681): 146–149, 1998.

[73] Zongping Chen, Wencai Ren, Libo Gao, Bilu Liu, Songfeng Pei, and Hui-Ming Cheng. Three-dimensional flexible and conductive interconnected graphene networks grown by chemical vapour deposition. *Nature Materials*, 10(6):424–428, 2011.

[74] Seung Jin Chae, Fethullah Günes, Ki Kang Kim, Eun Sung Kim, Gang Hee Han, Soo Min Kim, Hyeon-Jin Shin, Seon-Mi Yoon, Jae-Young Choi, Min Ho Park, Cheol Woong Yang, Didier Pribat, and Young Hee Lee. Synthesis of large-area graphene layers on nickel film by chemical vapor deposition: wrinkle formation. *Proc. SPIE*, 7399:73990 (1–11), 2009.

[75] Kevin R. Langley and James S. Sharp. Microtextured surfaces with gradient wetting properties. *Langmuir*, 26(23):18349–18356, 2010.

[76] Masashi Watanabe. Wrinkles formed on a thin gold film deposited onto stretched elastic substrates. *Polymers for Advanced Technologies*, 16(10): 744–748, 2005.

[77] Justin R. Serrano, Qinqin Xu, and David G. Cahill. Stress-induced wrinkling of sputtered sio2 films on polymethylmethacrylate. *Journal of Vacuum Science & Technology A: Vacuum, Surfaces, and Films*, 24(2):324–327, 2006.

[78] Michelle D. Casper, Arif O. Gozen, Michael D. Dickey, Jan Genzer, and Jon-Paul Maria. Surface wrinkling by chemical modification of poly(dimethylsiloxane)-based networks during sputtering. *Soft Matter*, 9: 7797–7803, 2013.

[79] Senjiang Yu, Yong Ni, Linghui He, and Quan-Lin Ye. Tunable formation of ordered wrinkles in metal films with controlled thickness gradients deposited on soft elastic substrates. *ACS Applied Materials & Interfaces*, 7(9):5160–5167, 2015.

[80] Senjiang Yu, Yadong Sun, Yong Ni, Xiaofei Zhang, and Hong Zhou. Controlled formation of surface patterns in metal films deposited on elasticity-gradient pdms substrates. *ACS Applied Materials & Interfaces*, 8(8):5706–5714, 2016.

[81] J. S. Sharp, D. Vader, J. A. Forrest, M. I. Smith, M. Khomenko, and K. Dalnoki-Veress. Spinodal wrinkling in thin-film poly(ethylene oxide)/polystyrene bilayers. *The European Physical Journal E*, 19(4):423–432, 2006.

[82] J. S. Sharp, K. R. Thomas, and M. P. Weir. Mechanically driven wrinkling instability in thin film polymer bilayers. *Phys. Rev. E*, 75:011601, 2007.

[83] J. S. Sharp and R. A. L. Jones. Swelling-induced morphology in ultrathin supported films of poly($d, l-$lactide). *Phys. Rev. E*, 66:011801, 2002.

[84] Mustafa M. Demir, Yusuf Z. Menceloglu, and Burak Erman. Effect of filler amount on thermoelastic properties of poly(dimethylsiloxane) networks. *Polymer*, 46(12):4127 – 4134, 2005.

[85] Kirill Efimenko, William E. Wallace, and Jan Genzer. Surface modification of sylgard-184 poly(dimethyl siloxane) networks by ultraviolet and ultraviolet/ozone treatment. *Journal of Colloid and Interface Science*, 254(2):306 – 315, 2002.

[86] Michael J. Owen and Patrick J. Smith. Plasma treatment of polydimethylsiloxane. *Journal of Adhesion Science and Technology*, 8(10):1063–1075, 1994.

[87] H. Hillborg and U.W. Gedde. Hydrophobicity recovery of polydimethylsiloxane after exposure to corona discharges. *Polymer*, 39(10):1991 – 1998, 1998.

[88] P.A. Sturrock. *Plasma Physics : Introduction to the Theory of Astrophysical, Geophysical and Laboratory Plasma*. Cambridge University Press, 1994.

[89] A. del Campo and E. Arzt. Fabrication approaches for generating complex micro- and nanopatterns on polymeric surfaces. *Chemical Reviews*, 108(3): 911–945, 2008.

[90] Ned Bowden, Wilhelm T. S. Huck, Kateri E. Paul, and George M. Whitesides. The controlled formation of ordered, sinusoidal structures by plasma oxidation of an elastomeric polymer. *Applied Physics Letters*, 75(17):2557–2559, 1999.

[91] Melanie Pretzl, Alexandra Schweikart, Christoph Hanske, Arnaud Chiche, Ute Zettl, Anne Horn, Alexander Böker, and Andreas Fery. A lithography-free pathway for chemical microstructuring of macromolecules from aqueous solution based on wrinkling. *Langmuir*, 24(22):12748–12753, 2008.

[92] Arnaud Chiche, Christopher M. Stafford, and Joao T. Cabral. Complex micropatterning of periodic structures on elastomeric surfaces. *Soft Matter*, 4:2360–2364, 2008.

[93] F. Angus Bayley, Joanne Lingling Liao, Paul N. Stavrinou, Arnaud Chiche, and Joao T. Cabral. Wavefront kinetics of plasma oxidation of polydimethylsiloxane: limits for sub-micron wrinkling. *Soft Matter*, 10:1155–1166, 2014.

[94] Kirill Efimenko, Mindaugas Rackaitis, Evangelos Manias, Ashkan Vaziri, L. Mahadevan, and Jan Genzer. Nested self-similar wrinkling patterns in skins. *Nature Materials*, 4(4):293–297, 04 2005.

[95] Edwin P. Chan and A. J. Crosby. Spontaneous formation of stable aligned wrinkling patterns. *Soft Matter*, 2:324–328, 2005.

[96] Charles J. Rand, Renee Sweeney, Mary Morrissey, Lauren Hazel, and Alfred J. Crosby. Fracture-induced alignment of surface wrinkles. *Soft Matter*, 4:1805–1807, 2008.

[97] Bernhard A. Glatz, Moritz Tebbe, Badr Kaoui, Roland Aichele, Christian Kuttner, Andreas E. Schedl, Hans-Werner Schmidt, Walter Zimmermann, and Andreas Fery. Hierarchical line-defect patterns in wrinkled surfaces. *Soft Matter*, 11(3332-3339), 2015.

[98] Juan Rodriguez-Hernandez and Adolfo del Campo. Fabrication of hierarchical wrinkled morphologies through sequentialuvo treatments. *Journal of Applied Polymer Science*, 132(17):41863(9), 2014.

[99] Hyun Suk Kim and Alfred J. Crosby. Solvent-responsive surface via wrinkling instability. *Advanced Materials*, 23(36):4188–4192, 2011.

[100] D. Breid and A.J. Crosby. Surface wrinkling behaviour of finite circular plates. *Soft Matter*, 5(2):425, 2009.

[101] D. Breid and A.J. Crosby. Effect of stress state on wrinkle morphology. *Soft Matter*, 7:4490–4496, 2011.

[102] E.P. Chan and A.J. Crosby. Fabricating microlens arrays by surface wrinkling. *Advanced Materials*, 18(24):3238–3242, 2006.

[103] Qiaoyuan Li, Xue Han, Jing Hou, Jian Yin, Shichun Jiang, and Conghua Lu. Patterning poly(dimethylsiloxane) microspheres via combination of oxygen plasma exposure and solvent treatment. *The Journal of Physical Chemistry B*, 119(42):13450–13461, 2015.

[104] Jun Young Chung, Adam J. Nolte, and Christopher M. Stafford. Diffusion-controlled, self-organized growth of symmetric wrinkling patterns. *Advanced Materials*, 21(13):1358–1362, 2009.

[105] Fuqian Yang and J. C. M. Li. Diffusion-induced beam bending in hydrogen sensors. *Journal of Applied Physics*, 93(11):9304–9309, 2003.

[106] L. Mahadevan and S. Rica. Self-organized origami. *Science*, 307(5716): 1740–1740, 2005.

[107] Ch. C. Dupont-Gillain, Y. Adriaensen, S. Derclaye, and P. G. Rouxhet. Plasma-oxidized polystyrene:wetting properties and surface reconstruction. *Langmuir*, 16(21):8194–8200, 2000.

[108] Robert J. Klein, Daniel A. Fischer, and Joseph L. Lenhart. Systematic oxidation of polystyrene by ultraviolet-ozone, characterized by near-edge x-ray absorption fine structure and contact angle. *Langmuir*, 24(15):8187–8197, 2008.

[109] I D Johnston, D K McCluskey, C K L Tan, and M C Tracey. Mechanical characterization of bulk sylgard 184 for microfluidics and microengineering. *Journal of Micromechanics and Microengineering*, 24(3):035017, 2014.

[110] Kyung M. Choi and John A. Rogers. A photocurable poly(dimethylsiloxane) chemistry designed for soft lithographic molding and printing in the nanometer regime. *Journal of the American Chemical Society*, 125(14):4060–4061, 2003.

[111] Cunjiang Yu, Kevin O'Brien, Yong-Hang Zhang, Hongbin Yu, and Hanqing Jiang. Tunable optical gratings based on buckled nanoscale thin films on

transparent elastomeric substrates. *Applied Physics Letters*, 96(4):041111, 2010.

[112] Patrick Görrn, Marcus Lehnhardt, Wolfgang Kowalsky, Thomas Riedl, and Sigurd Wagner. Elastically tunable self-organized organic lasers. *Advanced Materials*, 23(7):869–872, 2011.

[113] Won Hoe Koo, Soon Moon Jeong, Fumito Araoka, Ken Ishikawa, Suzushi Nishimura, Takehiro Toyooka, and Hideo Takezoe. Light extraction from organic light-emitting diodes enhanced by spontaneously formed buckles. *Nature Photonics*, 4(4):222–226, 04 2010.

[114] X. Jiang, S. Takayama, X. Qian, E. Ostuni, H.i Wu, N. Bowden, P. LeDuc, D. E. Ingber, and G.M. Whitesides. Controlling mammalian cell spreading and cytoskeletal arrangement with conveniently fabricated continuous wavy features on poly(dimethylsiloxane). *Langmuir*, 18(8):3273–3280, 2002.

[115] A. Venkateswara Rao, Sanjay S. Latthe, Digambar Y. Nadargi, H. Hirashima, and V. Ganesan. Preparation of mtms based transparent superhydrophobic silica films by sol–gel method. *Journal of Colloid and Interface Science*, 332(2):484 – 490, 2009.

[116] Sunetra L. Dhere, Sanjay S. Latthe, Charles Kappenstein, G.M. Pajonk, V. Ganesan, A. Venkateswara Rao, Pratap B. Wagh, and Satish C. Gupta. Transparent water repellent silica films by sol–gel process. *Applied Surface Science*, 256(11):3624 – 3629, 2010.

[117] Wei Jiang, Ming Mao, Wei Qiu, Yingming Zhu, and Bin Liang. Biomimetic superhydrophobic engineering metal surface with hierarchical structure and tunable adhesion: Design of microscale pattern. *Industrial & Engineering Chemistry Research*, 56(4):907–919, 2017.

[118] Yudi Rahmawan, Myoung-Woon Moon, Kyung-Suk Kim, Kwang-Ryeol Lee, and Kahp-Yang Suh. Wrinkled, dual-scale structures of diamond-like carbon (dlc) for superhydrophobicity. *Langmuir*, 26(1):484–491, 2010.

[119] Seung Goo Lee, Dong Yun Lee, Ho Sun Lim, Dae Ho Lee, Shichoon Lee, and Kilwon Cho. Switchable transparency and wetting of elastomeric smart windows. *Advanced Materials*, 22:5013–5017, 2010.

[120] Pei-Chun Lina and Shu Yang. Mechanically switchable wetting on wrinkled elastomers with dual-scale roughness. *Soft Matter*, 5:1011–1018, 2008.

[121] Y H Kim, Y M Lee, J Y Lee, M J Ko, and P J Yoo. Hierarchical nanoflake surface driven by spontaneous wrinkling of polyelectrolyte/metal complexed films. *ACS Nano*, 6(2):1082–1093, 2012.

[122] Yinyong Li, Shuxi Dai, Jacob John, and Kenneth R. Carter. Superhydrophobic surfaces from hierarchically structured wrinkled polymers. *Applied Materials and Interfaces*, 5:11066–11073, 2013.

[123] Seung Goo Lee, Dong Seok Ham, Dong Yun Lee, Hyojin Bong, and Kilwon Cho. Transparent superhydrophobic/translucent superamphiphobic coatings based on silica-fluoropolymer hybrid nanoparticles. *Langmuir*, 29:15051–15057, 2013.

[124] Robert N. Wenzel. Surface roughness and contact angle. *The Journal of Physical and Colloid Chemistry*, 53(9):1466–1467, 1949.

[125] A. B. D. Cassie and S. Baxter. Wettability of porous surfaces. *Trans. Faraday Soc.*, 40:546–551, 1944.

[126] Christopher M. Stafford, Shu Guo, Christopher Harrison, and Martin Y. M. Chiang. Combinatorial and high-throughput measurements of the modulus of thin polymer films. *Review of Scientific Instruments*, 76(6):062207, 2005.

[127] Emily D. Cranston, Mohamed Eita, Erik Johansson, Julia Netrval, Michaela Salajková, Hans Arwin, and Lars Wågberg. Determination of young's modulus for nanofibrillated cellulose multilayer thin films using buckling mechanics. *Biomacromolecules*, 12(4):961–969, 2011.

[128] Weixian Qian, Rubo Xing, Xinhong Yu, Xinjun Quan, and Yanchun Han. Highly oriented tunable wrinkling in polymer bilayer films confined with a

soft mold induced by water vapor. *The Journal of Chemical Physics*, 126 (6):064901, 2007.

[129] Fernando Carrillo, Shikha Gupta, Mehdi Balooch, Sally J. Marshall, Grayson W. Marshall, Lisa Pruitt, and Christian M. Puttlitz. Nanoindentation of polydimethylsiloxane elastomers: Effect of crosslinking, work of adhesion, and fluid environment on elastic modulus. *J. Mater. Res.*, 20(10): 2820–2830, 2011.

[130] Zhixin Wang, Alex A. Volinsky, and Nathan D. Gallant. Crosslinking effect on polydimethylsiloxane elastic modulus measured by custom-built compression instrument. *J. Appl. Polym. Sci.*, 131(22):41050 (1–4), 2014.

[131] John Sealy Edward Townsend. *The theory of ionization of gases by collision.* Constable, London, 1910.

[132] E.M. Bazelyan and Y.P. Raizer. *Spark Discharges.* CRS Press, New York, 1998.

[133] T.M. Hashem, M. Zirlewagen, and A. M. Braun. Simultaneous photochemical generation of ozone in the gas phase and photolysis of aqueous reaction systems using one vuv light source. *Water Science and Technology*, 35(4): 41–48, 1997.

[134] L. F. MacManus, M. J. Walzak, and N. S. McIntyre. Study of ultraviolet light and ozone surface modification of polypropylene. *Polymer Chemistry*, 37(14):2489–2501, 1999.

[135] J. F Rabek. *Mechanisms of Photophysical Processes and Photochemical Reactions in Polymers.* Wiley, New York, 1987.

[136] Alekh S. Bhurke, Per A. Askeland, and Lawrence T. Drzal. Surface modification of polycarbonate by ultraviolet radiation and ozone. *The Journal of Adhesion*, 83:43–66, 2007.

[137] Christopher M Stafford, Bryan D Vogt, Christopher Harrison, Duangrut Julthongpiput, and Rui Huang. Elastic moduli of ultrathin amorphous polymer films. *Macromolecules*, 39(15):5095–5099, 2006.

[138] Christopher Harrison, Christopher M. Stafford, Wenhua Zhang, and Alamgir Karim. Sinusoidal phase grating created by a tunably buckled surface. *Applied Physics Letters*, 85(18):4016–4018, 2004.

[139] E. Chason and T. M. Mayer. Thin film and surface characterization by specular x-ray reflectivity. *Critical Reviews in Solid State and Materials Sciences*, 22(1):1–67, 1997.

[140] Mario Birkholz. *Thin Film Analysis by X-Ray Scattering*. WILEY-VCH Verlag, 2006.

[141] M. Yasaka. X-ray thin film measurement techniques. v. x-ray reflectivity measurement. *The Rigaku Journal*, 26(2), 2010.

[142] H. Zabel. X-ray and neutron reflectivity analysis of thin films and superlattices. *Applied Physics A*, 58:159–168, 1994.

[143] H. Hillborg, J.F. Ankner, U.W. Gedde, G.D. Smith, H.K. Yasuda, and K. Wikström. Crosslinked polydimethylsiloxane exposed to oxygen plasma studied by neutron reflectometry and other surface specific techniques. *Polymer*, 41(18):6851 – 6863, 2000.

[144] Mark D. Foster. X-ray scattering methods for the study of polymer interfaces. *Critical Reviews in Analytical Chemistry*, 24(3):179–241, 1993.

[145] J Penfold and R K Thomas. The application of the specular reflection of neutrons to the study of surfaces and interfaces. *Journal of Physics: Condensed Matter*, 2(6):1369, 1990.

[146] H. Kiessig. Interferenz von röntgenstrahlen an dünnen schichten. *Annalen der physik*, 402(7):769–788, 1931.

[147] Nevot L. and Croce P. Characterization of surfaces by grazing x-ray reflection: application to study of polishing of some silicate-glasses. *Rev Phys Appl*, 15(3):761–779, 1980.

[148] Andrew Nelson. Co-refinement of multiple-contrast neutron/x-ray reflectivity data using motofit. *J. Appl. Crystallogr.*, 39(2):273–276, Apr 2006.

[149] URL `https://sourceforge.net/projects/rscl/`.

[150] R.C. Weast, editor. *Handbook of chemistry and physics*. CRC Press, Ohio, 57th edition, 1976.

[151] D. Richard, M. Ferrand, and G. J. Kearley. Analysis and visualisation of neutron-scattering data. *Journal of Neutron Research*, 4(1-4):33–39, 1996.

[152] M Nania, O K Matar, and J T. Cabral. Frontal vitrification of pdms using air plasma and consequences for surface wrinkling. *Soft Matter*, 11(15): 3067–3075, 2015.

[153] Brian S. Mitchell. *An Introduction to Materials Engineering and Science: For Chemical and Materials Engineers*. John Wiley and Sons, Ltd., 2004.

[154] S. Cai, D. Breid, A.J. Crosby, Z. Suo, and J.W. Hutchinson. Periodic patterns and energy states of buckled films on compliant substrates. *Journal of the Mechanics and Physics of Solids*, 59(5):1094 – 1114, 2011.

[155] Hanqing Jiang, Dahl-Young Khang, Jizhou Song, Yugang Sun, Yonggang Huang, and John A. Rogers. Finite deformation mechanics in buckled thin films on compliant support. *Proceedings of the National Academy of Sciences*, 104(40):15607–15612, 2007.

[156] J. Song, H. Jiang, Z.J. Liu, D.Y. Khang, Y. Huang, J.A. Rogers, C. Lu, and C.G. Koh. Buckling of a stiff thin film on a compliant substrate in large deformation. *International Journal of Solids and Structures*, 45(10):3107 – 3121, 2008.

[157] Hanqing Jiang, Dahl-Young Khang, Huiyang Fei, Hoonsik Kim, Yonggang Huang, Jianliang Xiao, and John A. Rogers. Finite width effect of thin-films buckling on compliant substrate: Experimental and theoretical studies. *Journal of the Mechanics and Physics of Solids*, 56(8):2585 – 2598, 2008.

[158] Hugues Vandeparre, Miguel Pineirua, Fabian Brau, Benoit Roman, José Bico, Cyprien Gay, Wenzhong Bao, Chun Ning Lau, Pedro M. Reis, and Pascal Damman. Wrinkling hierarchy in constrained thin sheets from suspended graphene to curtains. *Phys. Rev. Lett.*, 106(22):224301–224305, 2011.

[159] Diana B. H. Chua and H. T. Ng. Spontaneous formation of complex and ordered structures on oxygen-plasma-treated elastomeric polydimethylsiloxane. *Applied Physics Letters*, 76(6), 2000.

[160] J.T. Cabral and Jack F. Douglas. Propagating waves of network formation induced by light. *Polymer*, 46(12):4230 – 4241, 2005.

[161] James A. Warren, J. T. Cabral, and Jack F. Douglas. Solution of a field theory model of frontal photopolymerization. *Phys. Rev. E*, 72(2):021801–021813, 2005.

[162] D. F. Swinehart. The beer-lambert law. *Journal of Chemical Education*, 39 (7):333, 1962.

[163] Matthew G. Hennessy, Alessandra Vitale, Omar K. Matar, and João T. Cabral. Controlling frontal photopolymerization with optical attenuation and mass diffusion. *Phys. Rev. E*, 91(6):062402(12), 2015.

[164] Manuela Nania, Fabrizia Foglia, Omar K Matar, and João T Cabral. Sub-100 nm wrinkling of polydimethylsiloxane by double frontal oxidation. *Nanoscale*, 9(5):2030–2037, 2017.

[165] Hong-Gyu Park, Hae-Chang Jeong, Yoon Ho Jung, and Dae-Shik Seo. Control of the wrinkle structure on surface-reformed poly(dimethylsiloxane) via ion-beam bombardment. *Scientific Reports*, 5:12356 (8), 2015.

[166] Stéphane Béfahy, Pascale Lipnik, Thomas Pardoen, Cristiane Nascimento, Benjamin Patris, Patrick Bertrand, and Sami Yunus. Thickness and elastic modulus of plasma treated pdms silica-like surface layer. *Langmuir*, 26(5): 3372–3375, 2010.

[167] C. D. O'Connell, M. J. Higgins, S. E. Moulton, and G. G. Wallace. Nano-bioelectronics via dip-pen nanolithography. *J. Mater. Chem. C*, 3:6431–6444, 2015.

[168] Manuela Nania, Fabrizia Foglia, Omar K.Matar, and J. T. Cabral. Origin of multiple frequency wrinkling on elastomer sandwich bilayers. *Nano Letters*, To Submit, 2017.

[169] Binyang Du, Ophelia K. C. Tsui, Qingling Zhang, and Tianbai He. Study of elastic modulus and yield strength of polymer thin films using atomic force microscopy. *Langmuir*, 17(11):3286–3291, 2001.

[170] Jessica M. Torres, Christopher M. Stafford, and Bryan D. Vogt. Impact of molecular mass on the elastic modulus of thin polystyrene films. *Polymer*, 51(18):4211 – 4217, 2010.

[171] Adam J. Nolte, Robert E. Cohen, and Michael F. Rubner. A two-plate buckling technique for thin film modulus measurements:applications to polyelectrolyte multilayers. *Macromolecules*, 39(14):4841–4847, 2006.

[172] X.J. Feng and L. Jiang. Design and creation of superwetting/antiwetting surfaces. *Advanced Materials*, 18(23):3063–3078, 2006.

[173] P. A. O'Connell and G. B. McKenna. Novel nanobubble inflation method for determining the viscoelastic properties of ultrathin polymer films. *Review of Scientific Instruments*, 78(1):013901, 2007.

[174] Ranjana Saha and William D. Nix. Effects of the substrate on the determination of thin film mechanical properties by nanoindentation. *Acta Materialia*, 50(1):23 – 38, 2002.

[175] Pil J. Yoo and Hong H. Lee. Evolution of a stress-driven pattern in thin bilayer films: Spinodal wrinkling. *Phys. Rev. Lett.*, 91:154502, 2003.

[176] Edwin P. Chan, Kirt A. Page, Se Hyuk Im, Derek L. Patton, Rui Huang, and Christopher M. Stafford. Viscoelastic properties of confined polymer films measured via thermal wrinkling. *Soft Matter*, 5:4638–4641, 2009.

[177] R. Rizzieri, L. Mahadevan, A. Vaziri, and A. Donald. Superficial wrinkles in stretched, drying gelatin films. *Langmuir*, 22(8):3622–3626, 2006. PMID: 16584235.

[178] K. Laden. *Antiperspirants and deodorants*. Marcel Dekker Inc., New York-Basel, 1999.

[179] J. Rowsell and L. F. Nazar. Speciation and thermal transformation in alumina sols: Structures of the polyhydroxyoxoaluminum cluster [al30o8(oh)56(h2o)26]18+ and its delta-keggin moiete. *Journal of the American Chemical Society*, 122:3777–3778, 2000.

[180] Vojislava Pophristic, Michael L. Klein, and Marian N. Holerca. Modeling small aluminum chlorohydrate polymers. *The Journal of Physical Chemistry A*, 108(1):113–120, 2004.

[181] Dirk L. Teagarden, Joe L. White, and Stanley L. Hem. Aluminum chlorohydrate iii: Conversion to aluminum hydroxide. *Journal of Pharmaceutical Sciences*, 70(7):808 – 810, 1981.

[182] Yi Xu, Dongsheng Wang, Hong Liu, Lu Yiqiang, and Hongxiao Tang. Optimization of the separation and purification of al13. *Colloids and Surfaces A: Physicochemical and Engineering Aspects*, 231(1–3):1 – 9, 2003.

[183] Giulia L. Ferretti, Manuela Nania, Omar K. Matar, and João T. Cabral. Wrinkling measurement of the mechanical properties of drying salt thin films. *Langmuir*, 32(9):2199–2207, 2016.

[184] Giulia L. Ferretti and João T. Cabral. Phase behaviour and non-monotonic film drying kinetics of aluminium chlorohydrate–glycerol–water ternary solutions. *Journal of Colloid and Interface Science*, 481:263 – 270, 2016.

[185] Sergei V. Nemilov. Structural aspect of possible interrelation between fragility (length) of glass forming melts and poisson's ratio of glasses. *Journal of Non-Crystalline Solids*, 353(52–54):4613 – 4632, 2007.

[186] P.G. de Gennes. Solvent evaporation of spin cast films: "crust" effects. *The European Physical Journal E*, 7(1):31–34, 2002.

[187] Yu-Cheng Chen and Alfred J. Crosby. High aspect ratio wrinkles via substrate prestretch. *Advanced Materials*, 26(32):5626–5631, 2014.

[188] Farouk Ayadi and Patrice Dole. Stoichiometric interpretation of thermoplastic starch water sorption and relation to mechanical behavior. *Carbohydrate Polymers*, 84(3):872 – 880, 2011.

[189] Deeptangshu S. Chaudhary. Competitive plasticization in ternary plasticized starch biopolymer system. *Journal of Applied Polymer Science*, 118(1):486–495, 2010.

[190] Deeptangshu S. Chaudhary, Benu P. Adhikari, and Stefan Kasapis. Glass-transition behaviour of plasticized starch biopolymer system-a modified gordon-taylor approach. *Food hydrocolloids*, 25(1):114–121, 2011.

[191] L. Godbillot, P. Dole, C. Joly, B. Rogé, and M. Mathlouthi. Analysis of water binding in starch plasticized films. *Food Chemistry*, 96(3):380 – 386, 2006. 3rd International Workshop on Water in Foods.

[192] E.S. Kooij, H.P. Jansen, O. Bliznyuk, B. Poelsema, and H.J.W. Zandvliet. Directional wetting on chemically patterned substrates. *Colloids and Surfaces A: Physicochemical and Engineering Aspects*, 413:328 – 333, 2012.

[193] Levent Kubus, Hakan Erdogan, Erhan Piskin, and Gokhan Demirel. Controlling uni-directional wetting via surface chemistry and morphology. *Soft Matter*, 8:11704–11707, 2012.

[194] J.F Oliver and S.G Mason. Microspreading studies on rough surfaces by scanning electron microscopy. *Journal of Colloid and Interface Science*, 60 (3):480 – 487, 1977.

[195] J.P. Oliver, C. Huh, and S.G. Mason. An experimental study of some effects of solid surface roughness on wetting. *Colloids and Surfaces*, 1(1):79 – 104, 1980.

[196] L. Xu, L. Barcos, and S. R. Nagel. Splashing of liquids: Interplay of surface roughness with surrounding gas. *Phys. Rev. E*, 76:066311 (5), 2007.

[197] E. P. Chan, E. J. Smith, and A. J. Crosby R. C. Hayward. Surface wrinkles for smart adhesion. *Advanced Materials*, 20(4):711–716, 2008.

[198] Chelsea S. Davis and Alfred J. Crosby. Mechanics of wrinkled surface adhesion. *Soft Matter*, 7:5373–5381, 2011.

[199] Santanu Kundu, Chelsea S. Davis, Thomas Long, Ravi Sharma, and Alfred J. Crosby. Adhesion of nonplanar wrinkled surfaces. *Journal of Polymer Science Part B: Polymer Physics*, 49(3):179–185, 2011.

[200] Serge Mostowy and Pascale Cossart. Septins: the fourth component of the cytoskeleton. *Nat Rev Mol Cell Biol*, 13(3):183–194, 03 2012.

[201] Andrew A. Bridges, Maximilian S. Jentzsch, Patrick W. Oakes, Patricia Occhipinti, and Amy S. Gladfelter. Micron-scale plasma membrane curvature is recognized by the septin cytoskeleton. *The Journal of Cell Biology*, 213 (1):23–32, 2016.

[202] Qihui Zhou, Philipp T. Kühn, Thirsa Huisman, Elsje Nieboer, Charlotte van Zwol, Theo G. van Kooten, and Patrick van Rijn. Directional nanotopographic gradients: a high-throughput screening platform for cell contact guidance. *Scientific Reports*, 5:16240, 2015.

[203] Andrew F Adler, Alessondra T Speidel, Nicolas Christoforou, Kristian Kolind, Morten Foss, and Kam W Leong. High-throughput screening of microscale pitted substrate topographies for enhanced nonviral transfection

efficiency in primary human fibroblasts. *Biomaterials*, 32(14):3611–3619, 05 2011.

[204] Ying-Nan Wu, Jaslyn Bee Khuan Law, Ai Yu He, Hong Yee Low, James H.P. Hui, Chwee Teck Lim, Zheng Yang, and Eng Hin Lee. Substrate topography determines the fate of chondrogenesis from human mesenchymal stem cells resulting in specific cartilage phenotype formation. *Nanomedicine: Nanotechnology, Biology and Medicine*, 10(7):1507 – 1516, 2014.

[205] Lin Qi, Ning Li, Rong Huang, Qin Song, Long Wang, Qi Zhang, Ruigong Su, Tao Kong, Mingliang Tang, and Guosheng Cheng. The effects of topographical patterns and sizes on neural stem cell behavior. *PLoS ONE*, 8(3): e59022, 2013.

[206] Andreas S. Poulos, Manuela Nania, Paul Lapham, Ruhina M. Miller, Andrew J. Smith, Hossam Tantawy, Joel Caragay, Jérémie Gummel, Oscar Ces, Eric S. J. Robles, and João T. Cabral. Microfluidic saxs study of lamellar and multilamellar vesicle phases of linear sodium alkylbenzenesulfonate surfactant with intrinsic isomeric distribution. *Langmuir*, 32(23):5852–5861, 2016.

[207] Marco Adamo, Andreas S. Poulos, Ruhina M. Miller, Carlos G. Lopez, Anne Martel, Lionel Porcar, and Joao T. Cabral. Rapid contrast matching by microfluidic sans. *Lab on a Chip*, 17:1559–1569, 2017.

[208] Gh. Mohiuddin Mala and Dongqing Li. Flow characteristics of water in microtubes. *International Journal of Heat and Fluid Flow*, 20(2):142 – 148, 1999.

[209] David Pfund, David Rector, and Alireza Shekarriz. Pressure drop measurements in a microchannel. *AlChe Journal*, 46(8):1496–1507, 2000.

[210] Guobing Zhou and Shi-Chune Yao. Effect of surface roughness on laminar liquid flow in micro-channels. *Applied Thermal Engineering*, 31(2–3):228 – 234, 2011.

[211] Y.M. Kim, W.S. Kim, S.H. Lee, and J.Y. Baek. Effects of surface roughness on the flow characteristics in pdms micro-channels. *3rd IEEE/EMBS Special Topic Conference on Microtechnology in Medicine and Biology*, pages 292–295, 2005.